UNIVERSITÀ DEGLI STUDI DI PADOVA

Dipartimento di Fisica e Astronomia "Galileo Galilei"

Master Degree in Physics

Final Dissertation

Measurement of ultra-low optical absorption in mirror substrates for the next-generation gravitational wave detectors

Thesis supervisor

Prof. Jean-Pierre Zendri

Thesis co-supervisor

Prof. Marco Bazzan

Candidate

Stefano Gozzo

Academic Year 2020/2021

Ai miei genitori.

Before one enters the lab, things do work.
While one is in the lab, things no longer work.
After one exits the lab, things work once again.

Dōgen

Introduction

On 14 September 2015, one hundred years after the publication of the Theory of General Relativity, scientists of the VIRGO-LIGO collaboration were able to observe the first gravitational wave signal, confirming one of the most fascinating predictions of Einstein's theory and starting the era of multimessenger astronomy. Many more gravitational wave detections followed in recent years thanks to the developement of a network of second generation interferometers. Despite the initial success, the quantity and signal-to-noise ratio of this detections is still too low to perform accurate astronomical research and for consistently complementing electro-magnetical observations in the study of the most fundamental cosmic processes.
A new generation of gravitational wave interferometers with a considerably improved sensitivity is awaited to open the era of routine GW astronomy. The Einstein Telescope is an European Union project for a third generation gravitational wave interferometer that is at present undergoing design and prototyping phases.
In order to fulfill the sensitivity requirements of a third generation detector, it will be necessary to operate the Low Frequency interferometer of the Einstein Telescope in a cryogenic environment. This will establish an innovative technological challenge, as the substrate materials and coatings that are currently used in optical elements of second generation GW interferometers will be made unusable in a cryogenic enviroment due to increased mechanical losses. Therefore in recent years several research lines were started to investigate for new substrate materials with suitable characteristics for cryogenic operation. Crystalline silicon is among the most credited candidates to serve as substrate material in test masses of the Low Frequency detector of the Enstein Telescope.

This thesis work will contribute to the ongoing research on the charaterization of silicon optical properties in the same environment that is designed for the ET-LF detector. Throughout this document it will be illustrated the design and construction of a facility that allows to measure the optical absortion coefficient of crystalline silicon at cryogenic temperatures and for $\lambda = 1550\,\mathrm{nm}$ light. This kind of measurement is a non trivial task due to the very small magnitude of optical absorption in silicon, that ultimately makes it a favourable candidate as a test mass substrate material.
The absorption measurement will be performed with the use of an innovative method, compared to the ones that are commonly used in literature, the Modulation Calorimetry technique. The adaptation of this technique to optical absorption measurements was initially prompted by practical constraints related to the available instrumentation but eventually resulted in a solid method for accurate determination of $O(\,\mathrm{ppm})$ optical absorption coefficients in cryogenic environment. The α_{Si} estimate that is obtained in the experiment that is presented in this thesis will be compared to the only existing measurement of α_{Si} in analogous environmental conditions that is currently present in literature and the consequences of this findings on the Einstein Telescope design will be analyzed.

Contents

Part I

Chapter 1

Historical Overview of Gravitational Wave Searches

Gravitational wave and the attempts to detect them have a long and disputed history [1]. Born as an hypotetical analogy to the electromagnetical wave in an early work on Special Relativity by Henri Poincarè, they found their first rigorous mathematical description soon after the publication of the Theory of General Relativity, thanks to the effort of Albert Einstein that was able to find a wave-like solution to its field equations in a specific coordinate system. Yet Einsten himself was doubtful of the physicality of his solutions and his feelings were confirmed few years later when Sir. Arthur Eddington proved that two of the three of these wave solutions had a frame dependent propagation speed, so that they were a mere artifact of a wavy coordinate system. Hence Einstein reinforced his belief that gravitational waves were unphysical and went on to spread his opinion across the whole scientific community during the decades preceeding World War II.
During 1930s Einstein and Rosen published various theoretical papers demonstrating the unphysicality of wave-like solutions to the GR Equations that were eventually proven wrong by the work of H.P. Robertson. Despite Einstein admitting his mistake, Gravitational Waves remained an exotic subject among the physics community. During '50s the debate focused on whether or not Gravitational Waves would carry energy, but the dispute remained on theoretical ground as there were no experiment attempting at detecting them. This skewed state of affairs started to change after the Chapel Hill conference on General Relativity in January 1957. During the meeting devoted to Gravitational Waves, Richard Feynman persuaded the audience of their reality thanks to its famous 'Sticky Bead Argument'[1], finally settling the theoretical debate on the GW existence. One of the members of the audience happened to be Joseph Weber, an engineer from Maryland University that, fascinated by the topic, began to think about an experimental device that could achieve their detection.

Weber was the pioneer in the search for gravitational wave signals. In a 1960 paper [2] he summarized his ideas about the most promising strategies for their detection and during the following years he worked on the construction of the first Gravitational Wave Antenna, the 'Weber Bar', that begun the first data taking attempt in 1966 [3]. The Weber Bar consisted in a big aluminum cylinder with $66\,\mathrm{cm}$ diameter and $153\,\mathrm{cm}$ lenght, for a total wheight of around $3\,\mathrm{tons}$, suspended to a system aimed to insulate the mass from enviromental vibrations. The bar was enveloped by a strip of quartz transducers that converted mechanical strains to voltage signals and the whole system was sealed in a vacuum chamber.
This particular type of detector takes advantage of the resonance frequency of a mechanical system: if a gravitational wave with frequency that match exactly the resonant frequency of the bar passes

[1] In Feynman's thought experiment, a gravitational wave detector simply consist of two beads sliding freely on a rigid rod, oriented transversely to the propagation direction of the wave. As the gravitational wave passes, it excerts tidal forces on the objects respect to the center of the bar. Atomic forces hold the length of the rod fixed, instead nothing prevents the beads from sliding. If there's friction between the rod and the beads, heat will be dissipated in the process. Then, the energy source can only be the gravitational wave.

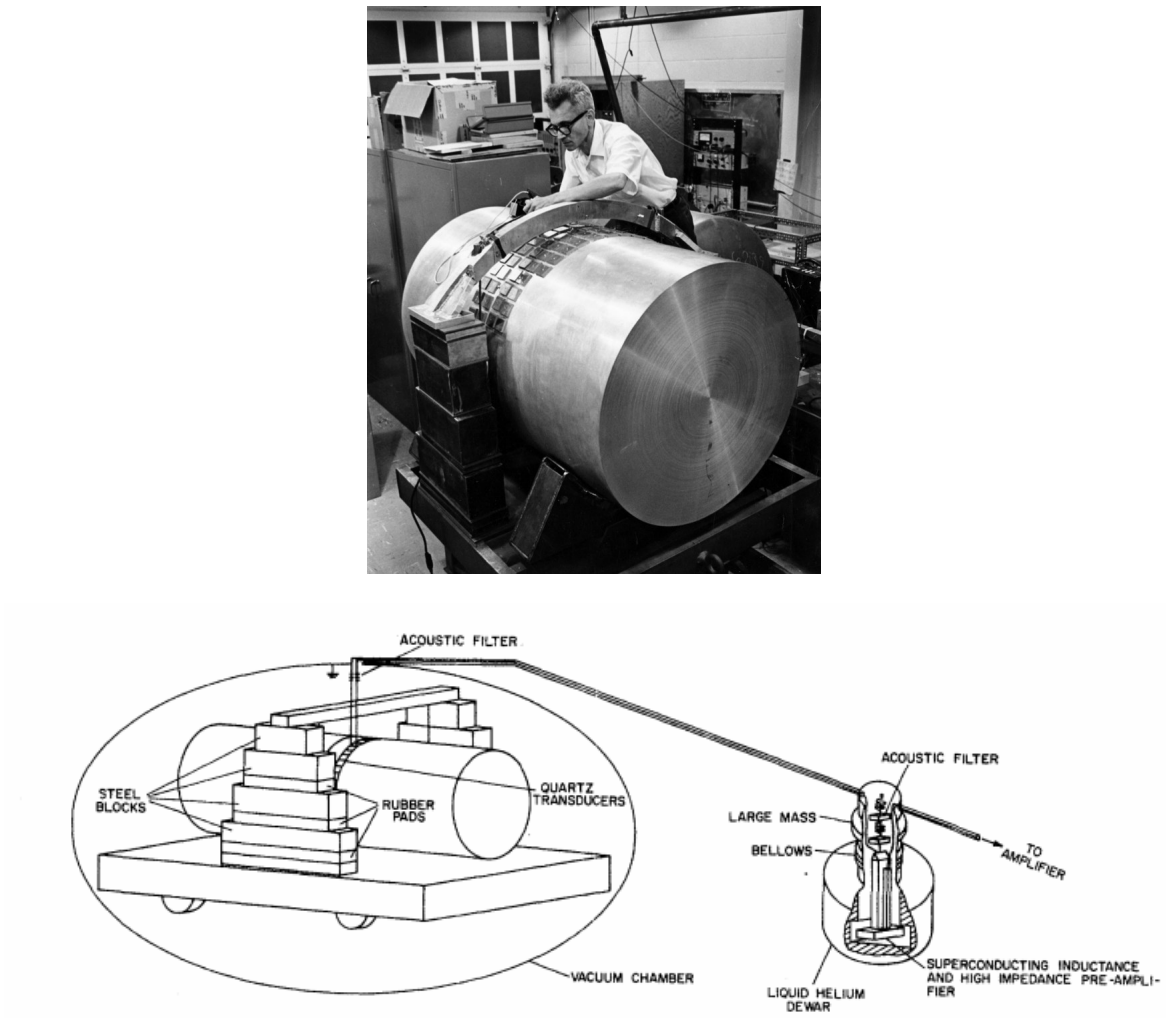

Figure 1.1: Up: Joseph Weber at work on one of his early resonant bar detector prototypes. Down: Scheme of the apparatus of the first Weber Bar [3]

through the detector with direction of propagation that is non-parallel to the bar axis, one could hope that the induced strain on the bar will be amplified enough to overcome the enviromental noises, hence becoming detectable. Unfortunately, this approach proved to be inefficient at detecting gravitational signals. The main problem with a resonant bar detector is the fact that its sensitivity is peaked only in a narrow frequency region around the mechanical resonant frequencies of the system, so that, in order for a gravitational signal to be detectable, not only it should exceed a treshold amplitude, but it should also peak its power at the exact frequency requested by the detector. Moreover, the technologies that were implemented in this early prototype detectors were inadequate to achieve a sufficient peak sensitivity to detect even the most optimistic gravitational wave event. Despite this fact, Weber was the first to understand the importance of having a global array of detectors that permits to reject local spurious signals based on coincidences, as he built two copies of his first prototype that were placed in two laboratories at a distance of $950\,\mathrm{km}$. Moreover his attempts prompted a fast development in the experimental field of gravitational wave searches in the following decades as many groups of scientists rushed to indepentely check Weber's measurement that claimed several Gravitational Wave signals that conflicted with the contemporary understanding of astronophysical processes, eventually ruling them out. The peak sensitivity for resonant bar detectors was reached in the late-'90s/early-2000s with the NAUTILUS and AURIGA ultracryogenic bar antennae at the INFN laboratories in Italy (Fig.1.2).

As the sensitivity of resonant bar detectors was improving, it became clear that Weber's method wasn't the optimal one for gravitational wave detection. There was a more promising strategy instead that

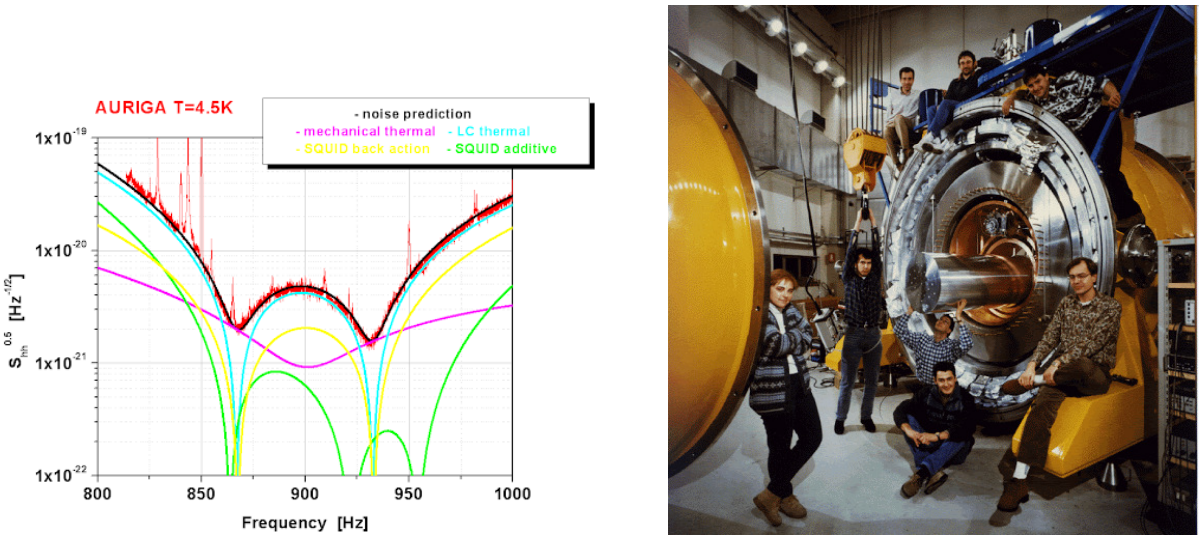

Figure 1.2: Left: Sensitivity of the AURIGA Detector, 2004. Right: Open Section of the AURIGA at the Laboratori Nazionali di Legnaro.

started developing in the 1970s: laser interferometry. The interferometric idea was nothing new between experimental physicist but it was applied for the first time to gravitational wave serches only in the early 70's, thanks to the independent efforts of Robert L. Forward [4] and Rainer Weiss [5]. In particular it was Weiss that, after having worked on an initial 1.5-m prototype at MIT and having contributed to the 30-m interferometer realized by the Garching group in Munich, Germany, laid the foundation for the LIGO (Laser Interferometer Gravitational-Wave Observatory) Project, a set of two 4-km long Michelson interferometers placed more than $3000\,\mathrm{km}$ apart at Hanford, WA and Livingstone, LA.

The LIGO large-scale interferometers were the first one to be built, as their construction started in 1994, but they were followed soon after by the VIRGO detector, a 3-km long Michelson interferometer built in Cascina, IT by a INFN-CNFR collaboration starting from the late '90s. These three detectors, togeter with the german GEO600 and the japanese TAMA, constituted the first generation of Gravitational Wave Interferometers. The initial version of the two LIGO interferometers started data acquisition in 2002, while VIRGO was fully operating for the first time in 2007. These early 2000s observation runs had the aim of testing a range of new technologies that were applied for the first time to large-scale interferometers and did not succeded in gravitational wave detection. Consequently the detectors were shut down between 2010 and 2011 to allow for the upgrade to their improved version, aLIGO (Advanced LIGO) [6] and AdV (Advanced VIRGO) [7] respectively. The upgraded detectors aimed for a factor 10 sensibility improvement respect to the initial versions, establishing the second generation of Gravitational Wave Interferometers. Sensitivities of these advanced gravitational wave detector reached values below $10^{-23}\,\sqrt{1/\mathrm{Hz}}$ accross a wide range of frequencies (Fig.1.3), a value that was expected to be comparable to the amplitudes of GW signals coming from nearest compact object inspiral events. More importantly, this was the frequency range inside wich gravitational wave signals from most of Bynary systems of Black Holes (BBH) and Neutron Stars (BNS) peaked their amplitude during mergers, so that the first gravitational wave event was eventually detected on September 14, 2015 by the aLIGO detector[2] [8], in the exact year of the 100th anniversary of the General Relativity Theory publication.

In the few years following the first gravitational wave detection a variety other signal were observed. A total of three observation runs has been conducted between 2015 and 2020, the last two of which the

[2]The first gravitational wave signal, GW150914, was observed by the aLIGO detector only, while it was still in 'engeneering' operational mode (its first official observation run would have started four days later, on September 18, 2015). The AdV detector started its first observation run on August 1, 2017.

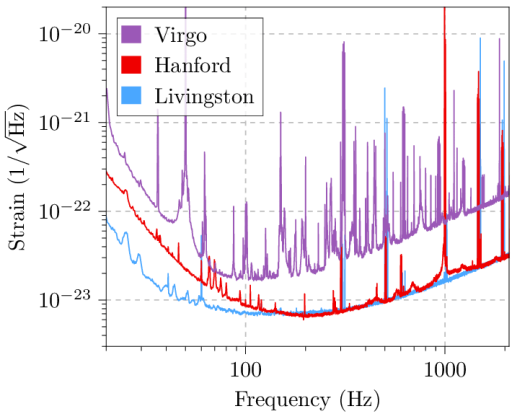

Figure 1.3: Left: Noise Spectral Density of the LIGO and VIRGO Detectors, September 2017. Right: Aerial View of the VIRGO interferometer in Santo Stefano a Macerata, IT.

three detectors were able to operate simultaneously. To have at least three working interferometers is crucial for triangulating the position in the sky of the signal source and it also allows to perform a better noise rejection based on multiple coincidences. During the first two runs a total of 11 gravitational wave events have been succesfully observed and the results of the first half of the third observation run has just been published, confirming the observation of 39 more GW signals, adding to a total of 50 detected merger events [9]. The majority of this events are Black Hole-Black Hole Mergers, but also two Neutron Star-Neutron Star Mergers were detected, for the first of which (GW170817) it was also detected the Electro-Magnetical counterpart of the gravitational wave signal, starting the era of multimessenger (EM-GW) astronomy [10].
Then, the Advanced LIGO and VIRGO detectors culminated the lenghty and winding hunt for gravitational waves, proving the physical existence of the fascinating space-time ripples. The number of GW events that are being digged out from the noisy interferometrical read-out signal of the three detectors is constantly increasing and this experimental findings are stimulating a multitude of theoretical and numerical reasearch to extensively test the General Relativity Theory along with expanding the current knowledge in the fields of Astrophysics, Cosmology and Fundamental Physics by directly observing the most powerful cosmic collisions.
In the coming years a new upgrade that will take the aLIGO and AdV detectors to their maximal design sensitivity is scheduled, but the three detector are already approaching their physical upper sensitivity bound. In order to understand where do the physical limitations to the aLIGO and AdV detector sensitivities come from and which strategies should be pursued to overcome them in a new generation of Gravitational Wave Interferometers, it is necessary to understand the theoretical framework of gravitational wave signals and their consequences on massive systems and the space-time fabric itself.

Chapter 2

Gravitational Waves in General Relativity

2.1 Linearized General Relativity

General Relativity is based upon the Equivalence Principle, the seemingly trivial assumption that inertial and gravitational mass are indistinguishable. Several experiments investigated an hypotetical discrepancy between the two masses even before XX sec., the most famous and precise of which was the Eötvös torsion balance experiment, conducted between 1885 and 1889, that verified the equivalence of the two quantities up to 1 part in 20 millions [11]. Nevertheless no one extensively considered the profound consequences of this principle before Einstein. The Einstein Equivalence Principle, that was illustrated by the german scientist in its famous elevator *Gedankenexperiment*, can be rigorously stated as follows: *"Fundamental non-gravitational test physics is not affected, locally and at any point of spacetime, by the presence of a gravitational field*[1]*."* [12]. Based on this general assumption, gravity can be described with a tensorial formalism as a space-time curvature induced by the energy-momentum distribution.
Spacetime is described as a Riemannian manifold, whose local geometry is summarized in the symmetric Metric Tensor $g_{\mu\nu}(x)$. The local relation between spacetime curvature and energy-momentum, which is quantified by the Energy-Momentum Tensor $T_{\mu\nu}$ in the neighbourhood of a spacetime point x is then illustrated by Einstein's Field Equations:

$$R_{\mu\nu} - \frac{1}{2} g_{\mu\nu} R = \frac{8\pi G}{c^4} T_{\mu\nu} \tag{2.1}$$

where $R_{\mu\nu}$ is the Ricci Tensor, R the Ricci Scalar[2], G the universal gravitational constant and c the speed of light.
The proportionality coefficient that relates Energy-Momentum to Spacetime Curvature is actually so

[1] In fact, the Equivalence Principle can be stated in various form with different logical extension. The first formulation given in this chapter, the equivalence of inertial and gravitational mass, is the weakest one (Weak Equivalence Principle, WEP), and its subordinated to the EEP formulation that was stated above. It is also possible to formulate the Equivalence Principle in a third, stronger, way (Strong Equivalence Principly, SEP), by requiring all the fundamental physics, including gravitation, to be unaffected by the presence of a gravitational field. It is the SEP formulation that is actually required for a proper derivation of Einstein's Field Equations.

[2] The Ricci Tensor and Scalar are defined in respect to the Riemann Tensor $R^{\mu}_{\nu\rho\sigma}$, which is in turn defined upon the Christoffel Symbol $\Gamma^{\rho}_{\mu\nu}$, a tensorial set of coefficients that refers directly to the Metric Tensor. The definition of these four quantities can be stated as follows:

$$\Gamma^{\rho}_{\mu\nu} = \frac{1}{2} g^{\rho\sigma} (\partial_\mu g_{\sigma\nu} + \partial_\nu g_{\sigma\mu} - \partial_\sigma g_{\mu\nu});$$

$$R^{\mu}_{\nu\rho\sigma} = \partial_\rho \Gamma^{\mu}_{\nu\sigma} - \partial_\sigma \Gamma^{\mu}_{\nu\rho} + \Gamma^{\mu}_{\alpha\rho} \Gamma^{\alpha}_{\nu\sigma} - \Gamma^{\mu}_{\alpha\sigma} \Gamma^{\alpha}_{\nu\rho};$$

$$R_{\mu\nu} = R^{\alpha}_{\mu\alpha\nu};$$

$$R = g^{\mu\nu} R_{\mu\nu}.$$

small ($\frac{8\pi G}{c^4} \approx 2 \times 10^{-43}\,\mathrm{s^2 m^{-1} kg^{-1}}$) that the attention can be focused on studying the linearization of Einstein's Field Equation around the flat-space metric $\eta_{\mu\nu} = diag(-1, 1, 1, 1)$. The expansion of the Metric Tensor in the linearized theory is defined as:

$$g_{\mu\nu} = \eta_{\mu\nu} + h_{\mu\nu}; \qquad |h_{\mu\nu}| << 1 \tag{2.2}$$

After choosing this almost Minkowskyian frame of reference one should proceed at linearizing all the quantites that are defined upon the Metric Tensor:

$$\Gamma^{\sigma}_{\mu\nu} = \frac{1}{2}(\partial_\mu h^\sigma_\nu + \partial_\nu h^\sigma_\mu - \partial^\sigma h_{\mu\nu}) \tag{2.3a}$$

$$R^{\sigma}_{\mu\nu\rho} = \frac{1}{2}(\partial_\nu\partial_\mu h^\sigma_\rho + \partial_\rho\partial^\sigma h_{\mu\nu} - \partial_\nu\partial_\sigma h^\sigma_\mu - \partial_\sigma\partial_\mu h^\sigma_\nu) \tag{2.3b}$$

$$R_{\mu\nu} = \frac{1}{2}(\partial_\nu\partial_\mu h + \Box h_{\mu\nu} - \partial_\nu\partial_\sigma h^\sigma_\mu - \partial_\sigma\partial_\mu h^\sigma_\nu) \tag{2.3c}$$

$$R = \Box h - \partial_\mu\partial_\sigma h^{\mu\sigma} \tag{2.3d}$$

where it was denoted $\Box = \partial_\sigma\partial^\sigma$ the D'Alembertian operator and $h = h^\sigma_\sigma$ the trace of the linear term of the Metric Tensor expansion. Then, defining the quantity:

$$\bar{h}_{\mu\nu} = h_{\mu\nu} - \frac{1}{2}\eta_{\mu\nu}h \tag{2.4}$$

a trivial algebraic substitution of Eqs.2.3 into Eq.2.1 leads to the linearized version of Einstein's Field Equations:

$$\Box\bar{h}_{\mu\nu} + \eta_{\mu\nu}\partial^\rho\partial^\sigma\bar{h}_{\rho\sigma} - \partial^\rho\partial_\nu\bar{h}_{\mu\rho} - \partial^\rho\partial_\mu\bar{h}_{\nu\rho} = \frac{16\pi G}{c^4}T_{\mu\nu}. \tag{2.5}$$

Having choosed a frame of reference where Eq.2.2 is valid, still leaves the freedom to perform a gauge transormation under which the equations will remain covariant. The wisest choice for the residual transformation is the Lorenz Gauge:

$$\partial^\nu h_{\mu\nu} = 0 \tag{2.6}$$

which immediately simplify the linearized field equations to a tensorial wave equation:

$$\Box\bar{h}_{\mu\nu} = \frac{16\pi G}{c^4}T_{\mu\nu}. \tag{2.7}$$

In order to study the propagation of the wave-like perturbations that arise from this equation and their interaction with test masses, Eq.2.7 should be analyzed in vacuum, that is the condition that surround the source, where $T_{\mu\nu} = 0$:

$$\Box\bar{h}_{\mu\nu} = 0. \tag{2.8}$$

A solution to this type of equation can be found with the Green Functions Method, that yelds:

$$\bar{h}_{\mu\nu} = A_{\mu\nu}e^{ik_\rho z^\rho}. \tag{2.9}$$

By inserting this wave-like solution into Eq.2.6 and Eq.2.8, two constraints on the $\bar{h}_{\mu\nu}$ tensor are obtained:

$$A^{\mu\nu}k_\mu = 0 \tag{2.10a}$$

$$k_\sigma k^\sigma = 0 \tag{2.10b}$$

wich lower its degrees of freedom from 10 to 6. In particular the first condition implies that the $\bar{h}_{\mu\nu}$ tensor will be transverse in this specific gauge[3], the second one that the wave-like perturbation will travel at the speed of light.

Starting from the current frame of reference it can be performed a further transformation that simplify the form of the $\bar{h}_{\mu\nu}$ tensor, without spoiling the Lorenz Gauge[4]. Then the 4 components of the new

[3]That is, the Gravitational Wave will be a transverse wave. A transverse wave is a wave whose oscillations take place in the plane that is perpendicular to the direction of propagation.

[4]It is trivial to show that a coordinate trasformation $x^\mu \to x^\mu + \zeta^\mu$ with $\Box\zeta_\mu = 0$, where ζ^μ is an infinitesimal quantity, is compatible with the Lorenz Gauge $\partial^\nu\bar{h}_{\mu\nu}$.This condition further implies $\Box\zeta_{\mu\nu} = 0$, where $\zeta_{\mu\nu} \equiv \partial_\mu\zeta_\nu + \partial_\nu\zeta_\mu - \eta_{\mu\nu}\partial_\sigma\zeta^\sigma$.

gauge transformation can be used to set 4 more constraints on $\bar{h}_{\mu\nu}$, reducing the number of its degrees of freedom from 6 to 2:

$$\bar{h}^{0i}_{TT} = 0; \qquad \bar{h}_{TT} = 0. \tag{2.11}$$

The frame of reference in which this conditions are valid is named Transverse Traceless Gauge (TT). The last two remaining degrees of freedom of the gravitational wave solution in the TT Gauge can be manifestly shown for a plane wave propagating along the z axis $\vec{k} = (1, 0, 0, 1)$:

$$\bar{h}^{TT}_{\mu\nu} = \begin{pmatrix} 0 & 0 & 0 & 0 \\ 0 & h_+ & h_\times & 0 \\ 0 & h_\times & h_+ & 0 \\ 0 & 0 & 0 & 0 \end{pmatrix} e^{i\omega(t-z/c)}. \tag{2.12}$$

The above equation is expressed in terms of the retarded time $t - z/c$ as the gravitational information is constrained to propagate at speed of light. The two Gravitational Wave Polarizations are named respectively Plus ($+$) and Cross ($\times$) Polarization. Then it can be immediately seen that, due to the passage of a Gravitational Wave, the invariant infinitesiaml space-time interval is periodically modulated:

$$\begin{aligned} ds^2 =& g_{\mu\nu}\, dx^\mu\, dx^\nu = \\ =& -c\, dt^2 + dz^2 + \{1 + h_+ \cos[\omega(t - z/c)]\}\, dx^2 \\ &+ \{1 - h_+ \cos[\omega(t - z/c)]\}\, dy^2 + 2h_\times \cos[\omega(t - z/c)]\, dx\, dy \end{aligned} \tag{2.13}$$

As the ds^2 is invariant, that is it's independent of the refence frame choice, the above equation manifestly shows that the Gravitational Wave solution has 'physical' effects and it's not an artifact of the specific Gauge choices that has been made to obtain Eq.2.12.

2.2 Geodesics and Newtonian Forces

Despite the general result obtained in Eq.2.1, if one is intrested at analyzing the effects of a Gravitational Wave on an array of test masses, the system should be studied in a (Local) Free Falling Reference Frame[5], as this reference frame is ideally inertial with the test masses of the interferometer, which are isolated from external non-gravitational forces. Moreover the oscillating coordinates of the TT Gauge does not reflect the experimental situation in which scientists hope to detect a displacement of the free falling test masses respect to a rigid ruler, that is a measurment apparatus so small that the modification induced on it by the passage of a Gravitational wave can be neglected[6]. The Free Falling Reference Frame of the experimental test masses is often referred as the Proper Detector Frame.
The equation of motion for a point mass in a background described by the metric $g_{\mu\nu}$ in absence of external forces is described by the Geodesic Equation[7]:

$$\frac{d^2x^\mu}{d^2\tau} + \Gamma^\mu_{\rho\sigma}(x)\frac{dx^\rho}{d\tau}\frac{dx^\sigma}{d\tau} = 0. \tag{2.14}$$

The above equation was parametrized in terms of the Proper Time τ, that is the time measured by a free falling clock following the given geodesic:

$$c^2\, d\tau^2 = -ds^2 = -g_{\mu\nu}\, dx^\mu\, dx^\nu. \tag{2.15}$$

[5] In theory, a Local Free Falling Reference Frame is defined by requiring that, in the neighborhood of the origin, the Christoffel Symbols vanish: $\Gamma^\mu_{\nu\rho}(x) = 0$.

[6] More precisely, when taking a resonant bar as a ruler, it can be considered rigid respect to the passage of a GW of frequency ω if its resonance frequency $\omega_0 >> \omega$.

[7] For a complete derivation of the Geodesic Equation, see [14].

As the aim of the analysis is to compare the geodesics of different free falling masses, the first thing to do is to fix a free falling reference frame that is inertial with a specific particle. In this reference frame, that is usually called Fermi Local Coordinate System, the metric is flat at first order even in the presence of Gravitational Waves:

$$ds^2 \approx c^2\, dt^2 - \delta_{ij}\, dx^i\, dx^j. \tag{2.16}$$

Then, expanding the metric at second order around the origin of the free falling frame and expressing the second derivatives of $g_{\mu\nu}$ in terms of the Riemann Tensor, the following result is obtained[8]:

$$\begin{aligned} ds^2 \approx & - c^2\, dt^2[1 + R_{0i0j}x^i x^j] \\ & - 2c\, dt\, dx^i \Big(\frac{2}{3} R_{0ijk} x^j x^k\Big) + dx^i\, dx^j \Big[\delta_{ij} - \frac{1}{3} R_{ikjl} x^k x^l\Big]. \end{aligned} \tag{2.17}$$

Then we can consider two nearby geodesics each parametrized by its own proper time, the coordinate distance that separates the two free falling particles on the geodesics is the space-time vector $\mathcal{E}^\mu(\tau)$ that connect points with the same value of τ on the two geodesics. The Geodesic Equation 2.14 will be valid along the first geodesic $x^\mu(\tau)$, while on the second goedesic $x^\mu(\tau) + \mathcal{E}^\mu(\tau)$ it will take the form:

$$\frac{d^2(x^\mu + \mathcal{E}^\mu)}{d^2\tau} + \Gamma^\mu_{\rho\sigma}(x + \mathcal{E}) \frac{d(x^\rho + \mathcal{E}^\rho)}{d\tau} \frac{d(x^\sigma + \mathcal{E}^\sigma)}{d\tau} = 0. \tag{2.18}$$

Assuming $|\mathcal{E}(\tau)|$ is much smaller than the typical scale of variation of the gravitational field, its evolution can be studied by taking the first order difference between Eq.2.14 and Eq.2.18, obtaining the Geodesic Deviation Equation:

$$\frac{d^2\mathcal{E}^\mu}{d^2\tau} + 2\Gamma^\mu_{\rho\sigma}(x) \frac{dx^\rho}{d\tau} \frac{d\mathcal{E}^\sigma}{d\tau} + \mathcal{E}^\nu \partial_\nu \Gamma^\mu_{\rho\sigma}(x) \frac{dx^\rho}{d\tau} \frac{dx^\sigma}{d\tau} = 0. \tag{2.19}$$

Near the Proper Detector Frame origin $\Gamma^\mu_{\rho\sigma}(x)$ vanishes and $dx^i/d\tau$ can be neglected respect to $dx^0/d\tau$ as the detector is moving non-relativistically:

$$\frac{d^2\mathcal{E}^i}{d^2\tau} + \mathcal{E}^\sigma \partial_\sigma \Gamma^i_{00}(x) \Big(\frac{dx^0}{d\tau}\Big)^2 = 0. \tag{2.20}$$

The Geodesic Deviation Equation in the Proper Detector Frame can be further rewritten by noting that near the origin only the both-spatial double derivatives of the metric are non vanishing, thus $\mathcal{E}^\sigma \partial_\sigma \Gamma^i_{00} = \mathcal{E}^j \partial_j \Gamma^i_{00}$. Moreover, in the PDF we have by definition $\partial_0 \Gamma^i_{0j} = 0$, then it is also valid $R^i_{0j0} = \partial_j \Gamma^i_{00} - \partial_0 \Gamma^i_{0j} = \partial_j \Gamma^i_{00}$. Therefore Eq.2.20 becomes[9]:

$$\frac{d^2\mathcal{E}^i}{d^2\tau} = -R^i_{0j0} \mathcal{E}^j \Big(\frac{dx^0}{d\tau}\Big)^2. \qquad \Rightarrow \qquad \ddot{\mathcal{E}}^i = -c^2 R^i_{0j0} \mathcal{E}^j. \tag{2.21}$$

In order to compute R^i_{0j0}, one can take advantage of the fact that in the linearized theory the Riemann Tensor is invariant rather than covariant, so that it can be equivalently computed in TT Gauge, where its derivation is easier due to the simpler form of Gravitational Waves in this reference frame. From the Riemann Tensor definition it follows immediately $R^i_{0j0} = R_{i0j0} = -\frac{1}{2c^2} \ddot{h}^{TT}_{ij}$, and the Geodesic Deviation Equation in the Proper Detector Frame eventually becomes:

$$\ddot{\mathcal{E}}^i = \frac{1}{2} \ddot{h}^{TT}_{ij} \mathcal{E}^j. \tag{2.22}$$

[8] For an Earthbound detector one should also account for the fact that the laboratory frame is accelerated and rotating. This would yeld various additional terms to the ds^2 expression (Centrifugal acceleration, Coriolis Effect, ecc.). This terms actually have much bigger amplitudes respect to the Riemann Tensor terms that are explicited in Eq.2.17 at low frequencies, but at sufficiently high frequencies this contributions are highly suppressed and we can neglect them.

[9] At first order in h we have $t = \tau$ and $dx^0/d\tau = c$. We also denote with $\dot{\mathcal{E}}$ the derivative with respect to the coordinate time t of the Proper Detector Frame.

The physical meaning of this simple equation is that, in the Proper Detector Frame, the effect of a Gravitational Wave on an array of point particles can be described in terms of a Newtonian Force. It's important to underline that in the Proper Detector Frame at first order coordinate distances $\mathcal{E}^i$ are equal to proper distances s^i. Then, upon verification that the first order approximation is satisfied in the experimental set-up, the result 2.22 has general validity and it describes the physical response of the system to a GW passage in every possible non-relativistic frame, included the TT Gauge.

2.3 GW's Effect on an Array of Test Masses

As an example it can be studied the effect of a Gravitational Wave propagating along the z-axis on a ring of test masses laying on the xy-plane[10]. The two GW polarizations can be studied separately. Starting from the Plus polarization ($h_\times = 0$) and remembering the $\bar{h}^{TT}_{ab}$ expression from Eq.2.12, the proper distance variation between the ring particles and the origin of the plane can be studied upon defining $\mathcal{E}_a(t) = (x_0 + \delta x(t), y_0 + \delta y(t))$. Then Eq.2.22 becomes:

$$\begin{aligned} \ddot{\mathcal{E}}^1_a = \delta\ddot{x} &= -\frac{h_+}{2}(x_0 + \delta x)\omega^2 \sin(\omega t) \\ \ddot{\mathcal{E}}^2_a = \delta\ddot{y} &= +\frac{h_+}{2}(y_0 + \delta y)\omega^2 \sin(\omega t). \end{aligned} \tag{2.23}$$

The δx and δy terms on the right side of the above equations can be neglected to linear order in h as they have dimension $O(h_+)$, so that the differential equation can be directly integrated:

$$\begin{aligned} \delta x(t) &= +\frac{h_+}{2} x_0 \sin(\omega t) \\ \delta y(t) &= -\frac{h_+}{2} y_0 \sin(\omega t). \end{aligned} \tag{2.24}$$

Proceeding analogously for the Cross polarization case ($h_+ = 0$), the resulting evolution of the test mass displacement is:

$$\begin{aligned} \delta x(t) &= +\frac{h_\times}{2} y_0 \sin(\omega t) \\ \delta y(t) &= +\frac{h_\times}{2} x_0 \sin(\omega t). \end{aligned} \tag{2.25}$$

The periodical modulation effect of each GW poarization on a ring of test masses is shown in Fig.2.1. In the general case where both polarizations are present the resulting effect is a superposition of the two single-polarization modulations. It's important to note few aspects of the results obtained in Eq.2.24 and Eq.2.25. The test mass displacements are proportional to the distance between the particle and the origin of the frame of reference. This means that the effect of GW passage is a constant relative deformation of the detector along the perpendicular direction to the the wave-vector:

$$\frac{\delta l}{l} = \pm\frac{h_{+/\times}}{2} \sin(\omega t). \tag{2.26}$$

It can be seen that the only free parameters that govern the relative detector deformation are the polarization amplitude h and the GW frequency ω. The parameters are dictated both by the source properties

[10] As GWs are transverse waves, there are no effects of their passage manifesting along the parallel direction to the wave vector. Then we can fix the test mass array on the perpendicular plane to the direction of propagation and their effect will be maximized.

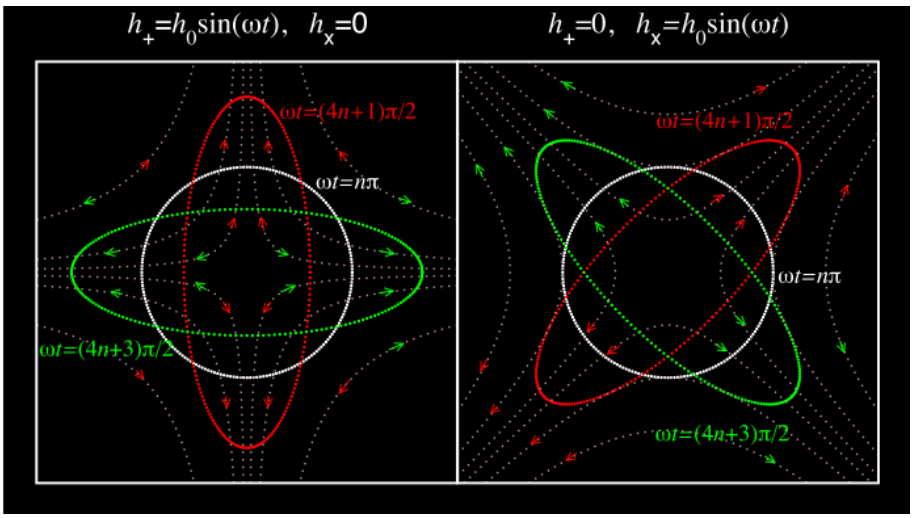

Figure 2.1: Effects of Plus (left) and Cross (right) polarization on a ring of test masses. The tidal field of the waves on the ring is indicated by light dotted lines. The direction of the force reverses sign each half-period of the wave as indicated by the red and green arrows.

and its distance and orientation respect to the detector. Then, if one is intrested in studying the feasibility of Gravitational Wave detection it is necessary to estimate the magnitude of this quantities at source and after propagation. Nowadays, in order to extract the source and sky location parameters from the interferometer mirror displacement, the acquired signal is compared with a detailed catalogue of waveform templates obtained via Numerical Relativity to find the set of parameters that best match the observation. Nevertheless it is still possible to gain an useful insight on Gravitational Wave generation and propagation by trying to solve analitically GR's linearized field equations under certain approximations and simmetry assumptions. In particular, for a system of two point-like masses in circular orbit around the center of mass of the system with non-relativistic velocities, expanding to the leading quadrupole radiation term at large distances from the source, the following result for the Gravitational Wave Amplitude can be obtained[11]:

$$h \approx \frac{1}{r}\frac{G\,\mu\,\omega_S^2\,R^2}{c^4} \tag{2.27}$$

where $\mu = m_1 m_2/(m_1 + m_2)$ is the reduced mass of the system, ω_S is the orbital frequency and R the orbital radius. The most important aspect of this equation is the $1/r$ GW Strain dependence upon propagation, that is analogous to multipole radiation instead of an usual spherical wave, which amplitude decreases as $1/r^2$. This desirable amplitude proportionality has a remarkable consequence for the detector upgrade design; in fact, an order 10 improvement in the detector sensibility translates in a 10^3 increase of the space-time volume that could be explored with the instrument. Then, as the LIGO and VIRGO detectors are close to achieving their maximal design sensitivity, it is advantageous to start researching and designing a new generation of Earthbound interferometrical detectors that will be capable of exceeding at least of an order of magnitude the sensitivity of the current detectors.

[11] See [13] for a detailed derivation.

Chapter 3

The Interferometric Method for GW Detection

3.1 Michelson Interferometers

The basic concept at the core of the modern antennae that succeded in the first gravitational wave detections in the last few years is the simple one of the Michelson Interferometer. A Michelson Interferometer is, in its simplest configuration, an array of two mirrors and one beam splitter together with a monocromatic light source that allows to sense a variation in the differential length between the two interferometer arms exploiting the phenomenon of interference of Electro-Magnetical Waves. The operating principle of a Michelson interferometer and its interactions with a Gravitational Wave are summarized in the following section.

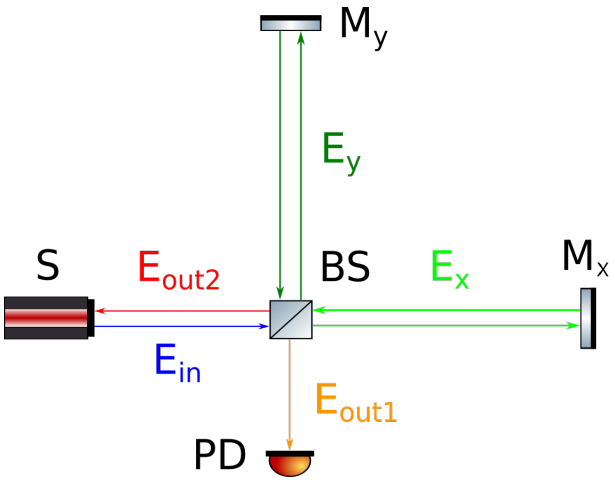

Figure 3.1: Basic Michelson interferometer scheme. Monocromatic Source (S), Beam Splitter (BS), Mirrors (M_x,M_y), Photodiode (PD).

The scheme of a basic Michelson Interferometer configuration can be seen in Fig.3.1. The monochromatic light source is nowadays always provided by a laser device. The beam is splitted in two orthogonal arms and after having travelled twice along each arm it recombines at the beam splitter, partly heading toward the output port and partly directed back to the input source.
The input beam can be represented with the complex notation for electromagnetical fields:

$$E_{in} = E_0 e^{-i(\omega_l t - \vec{k_l}\cdot\vec{x})} \tag{3.1}$$

where ω_l is the laser frequency and $\vec{k_l}$ the laser beam wave vector ($|\vec{k_l}| = 2\pi/\lambda_l = \omega_l/c$). After being divided and recombined, the output beam amplitude can be obtained by the superposition of the two

x/y-arm beams, properly accounting for the $\phi_{x/y}$ phase picked up upon reflection:

$$E_x = \frac{E_0}{\sqrt{2}} e^{i(k_l L_x - \omega_l t + \phi_x)}, \qquad E_y = \frac{E_0}{\sqrt{2}} e^{i(k_l L_y - \omega_l t + \phi_y)} \tag{3.2}$$

where the factor 2 at denominator is due to the double transmission through the beam splitter. Then the output intensity is immediately obtained from the output amplitude expression:

$$I_{Out} = |E_{Out}|^2 = |E_x + E_y|^2 = \frac{E_0^2}{2}\Big(1 + \cos\big(k(L_x - L_y) + (\phi_x - \phi_y)\big)\Big). \tag{3.3}$$

The electromagnetical wave acquires a $\phi = \pi$ extra-phase at each reflection. Then the acquired phases for the two input and output directed recombined beams can be explicitely computed: the output directed beam ($Out1$) acquires a total phase $\phi_1 = \phi_x - \phi_y = (\pi + \pi) - (\pi + \pi) = 0$; the input directed beam ($Out2$) acquires a total phase $\phi_2 = \phi_x - \phi_y = \pi - (\pi + \pi + \pi) = -2\pi$. Then the intensities of the two recombining beams become:

$$\begin{aligned} I_{Out1} =& \frac{E_0^2}{2}\Big(1 - \cos\big(k(L_x - L_y)\big)\Big) = E_0^2 \sin^2\big(k(L_x - L_y)\big); \\ I_{Out2} =& \frac{E_0^2}{2}\Big(1 + \cos\big(k(L_x - L_y)\big)\Big) = E_0^2 \sin^2\big(k(L_x - L_y) + \pi\big). \end{aligned} \tag{3.4}$$

Therefore a variation in the differential length of the two interferometer arms results in a power variation at the output port that could be properly detected with a photodiode, while the remaining power is sent back to the input port, consistently with energy conservation principle.

If one then desires to analyze the response of a Michelson Interferometer to a Gravitational Wave passage, the TT Gauge is the most convenient frame in which conducting the analysis, as the coordinate of the free falling interferometrical test masses are fixed by definition in this reference frame. Instead it is the light beam propagation time across the interferometer arms that is affected from the Gravitational Wave passage in TT Gauge.
Assuming for simplicity that the Gravitational Wave is composed only of Plus polarization ($h_\times = 0$) and that it is traveling along the z direction, for an interferometer laying in the $z = 0$ plane the metric linear expansion term becomes:

$$h_+(t) = h_0 \cos(\omega_{gw} t) \tag{3.5}$$

where ω_{gw} is the frequency of the incoming Gravitational Wave. Then, for a photon travelling along a null geodesic, the invariant space-time interval results:

$$ds^2 = -c^2\, dt^2 + \big(1 + h_+(t)\big)dx^2 + \big(1 - h_+(t)\big)dy^2 + dz^2 = 0. \tag{3.6}$$

The above equation can be projected to a single coordinate to calculate the total photon travel time along each arm. Starting from the x arm, at linear order in h_0:

$$dx = \sqrt{\frac{c^2\, dt^2}{1 + h_+(t)}} \approx \pm c\, dt\big(1 - \frac{1}{2}h_+(t)\big) \tag{3.7}$$

where the $+$ sign distinguish the back and forth trips. Starting from the beam splitter at instant t_0, the time t_1 at wich the photon reaches the x arm mirror is obtained by integrating Eq.3.7 with the plus sign the two endpoints $x = 0$ and $x = L_x$:

$$\int_0^{L_x} dx = +c \int_0^{t_1} dt\big(1 - \frac{1}{2}h_+(t)\big) \qquad \Rightarrow \qquad L_x = c(t_1 - t_0) - \frac{c}{2}\int_{t_0}^{t_1} dt h_+(t). \tag{3.8}$$

An analogous integration with the minus sign for the return trip from the mirror $x = L_x$ to the beam splitter $x = 0$, gives:

$$\int_{L_x}^{0} dx = -c \int_{t_1}^{t_2} dt\big(1 - \frac{1}{2}h_+(t)\big) \qquad \Rightarrow \qquad L_x = c(t_2 - t_1) - \frac{c}{2}\int_{t_1}^{t_2} dt h_+(t). \tag{3.9}$$

The sum of Eq.3.8 and Eq.3.9 gives the total travel time for the photon that is moving along the x arm:

$$t_2 - t_0 = \frac{2L_x}{c} + \frac{1}{2}\int_{t_0}^{t_2} dt h_+(t). \tag{3.10}$$

As the integrand in Eq.3.10 is already of order $O(h_0)$, the upper limit of the integral can be approximated with the flat metric roundtrip time $t_2 = t_0 + 2L_x/c$. Exploiting the trigonometric expression $\sin(\alpha + 2\beta) - \sin(\alpha) = 2sin(\beta)\cos(\alpha + \beta)$, the following expression is obtained:

$$\begin{aligned} t_2 - t_0 =& \frac{2L_x}{c} + \frac{1}{2}\int_{t_0}^{t_0+2L_x/c} dt h_0 \cos(\omega_{gw} t) = \\ =& \frac{2L_x}{c} + \frac{h_0 L_x}{c}\frac{\sin(\omega_{gw}L_x/c)}{\omega_{gw}L_x/c}\cos\big(\omega_{gw}(t_0 + L_x/c)\big) = \\ =& \frac{2L_x}{c} + \frac{L_x}{c}\, h_+\big(t_0 + \frac{L_x}{c}\big)\,\frac{\sin(\omega_{gw}L_x/c)}{\omega_{gw}L_x/c} \end{aligned} \tag{3.11}$$

where, in the last identity, Eq.3.5 was used to simplify the expression. The above equation shows that the flat-metric photon roundtrip travel time along an arm ($2L_x/c$) is modified by the passage of a Gravitational Wave with a term that is proportional to the value of the GW amplitude at the instant when the photon reaches the arm mirror ($t_0 + L_x/c$) and to the arm length L_x. Moreover, the roundtrip travel time modification is proportional to the function:

$$\mathrm{sinc}\,\big(\frac{\omega_{gw}L_x}{c}\big) \equiv \frac{\sin(\omega_{gw}L_x/c)}{\omega_{gw}L_x/c} \tag{3.12}$$

the behaviour of which is shown in Fig.3.2. The sinc function approaches 1 for $\omega_{gw}L_x/c << 1$ and the travel time modification simplifies to $h_+(t_1)L_x/c$, while it get suppressed for $\omega_{gw}L_x/c >> 1$. This behaviour has a simple physical interpretation: if the detector arm is made too long, then $\omega_{gw}L_x/c >> 1$ and the GW metric perturbation changes sign many times along the roundtrip, so that its overall effect gets averaged out; on the contrary, if the interferometer arm is made too short, then it is the L_x factor that inhibits the dector sensibility to detect variations in the metric, as there is not enough time for the photon that is travelling along the arm to integrate the Gravitational Wave effect. Then the interferometer lenght must be ideally optimized to maximize the signal in the possible frequency range of the target source.

An analogous computation can be performed for the y-arm case. Comparing the roundtrip travel time in the two orthogonal arms the total phase difference introduced by a Gravitational Wave in the Michelson interferometer output beam is obtained:

$$\Delta\phi_{Mich} \approx \omega_l\Big(2\frac{L_x - L_y}{c} + \frac{2L}{c}h_0\cos(\omega_{gw}t + \alpha)\,\mathrm{sinc}\,\big(\frac{\omega_{gw}L}{c}\big)\Big) = \Delta\phi_0 + \Delta\phi_{gw} \tag{3.13}$$

where the first order in h_0 approximation $L_x \approx L_y \approx L$ was performed, as the usual experimental configuration for a Michelson Interferometer is nearly symmetrical[1]. Substituting back this result

[1]More specifically, the $\Delta\phi_0$ term contains two contributions that are properly tuned by experimentalist to build the optimal conditions for GW detection in the interferometer. In particular, the first one is a microscopical asymmetry term to control the interferometer working point, that is the intensity of the recombined beam directed to the output port that, for various reasons, it is not null; the second one is a macroscopic term, named Schnupp Asymmetry, that is needed for allowing the GW frequency sidebands (see Eq.3.16) to leak out at the output port.

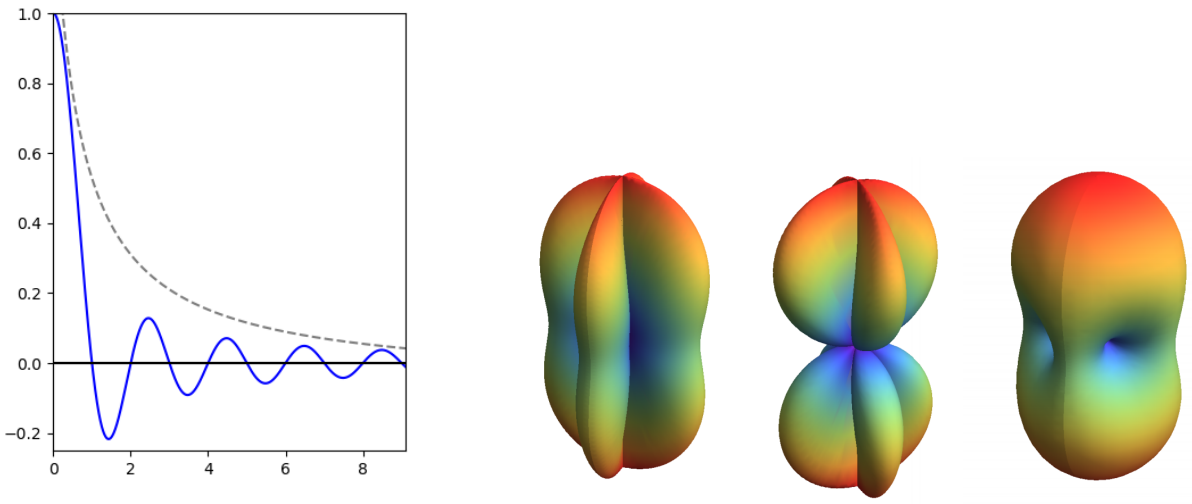

Figure 3.2: Left: Sinc function (blue) compared to $1/x$ (dashed) in the positive domain. Right: (From left to right) Antenna Pattern of a Michelson Interferometer in the $+$, $\times$, and generic polarization cases [15].

in Eq.3.4, it is shown how the intensity of the recombined beam in a Michelson Interferometer is modulated by the passage of a Gravitational Wave:

$$I_{Out} = E_0^2 \sin^2(\Delta\phi_0 + \Delta\phi_{gw}). \tag{3.14}$$

Specifically, the ideal interferometer arm length for detecting a Gravitational Wave of given frequency can be explicitely computed by maximising the GW induced phase in the recombined beam $\Delta\phi_{gw}$, giving the following result result ($f_{gw} = \omega_{gw}/2\pi$):

$$L \approx 750\,\mathrm{km}\left(\frac{100\,\mathrm{Hz}}{f_{gw}}\right) \tag{3.15}$$

It can also be noted that, extending the computation to a generic arm and analyzing the result with the complex field notation, the following expression at first order in h_0 for the amplitude of the recombined beam that is directed toward the output port is obtained:

$$\begin{aligned} E_{Out1} =& \frac{E_0}{2} e^{-i\omega_l\left(t-\frac{2L}{c}\right)} e^{+i\omega_l \frac{L}{c} h_+\left(t-\frac{L}{c}\right)} \operatorname{sinc}\left(\tfrac{\omega_{gw}L}{c}\right) \approx \\ \approx& \frac{E_0}{2} e^{-i\omega_l\left(t-\frac{2L}{c}\right)} \left(1 + i\omega_l \frac{L}{c} \operatorname{sinc}\left(\frac{\omega_{gw}L}{c}\right) \frac{e^{i(\omega_{gw}t+\alpha)} + e^{-i(\omega_{gw}t+\alpha)}}{2}\right) = \\ =& \frac{E_0}{2} e^{2i\alpha}\left(e^{-i\omega_l t} + \beta e^{-i\alpha} e^{-i(\omega_l-\omega_{gw})t} + \beta e^{-i\alpha} e^{-i(\omega_l+\omega_{gw})t}\right) \end{aligned} \tag{3.16}$$

where $\alpha = -\omega_{gw}L/c$ is the generic flat-metric halftrip phase and β an irrelevant phase. Then, Eq.3.16 shows that the passage of a Gravitational Wave has the effect of generating two symmetrical frequency sidebands in the output beam that are spaced by a frequency ω_{gw} from the carrier laser frequency ω_l. By instead considering the general case of a Gravitational Wave that is generated by a source located at a θ zenith angle and ϕ azimuthal angle respect to the detector plane:

$$h(t) = \frac{1}{2}\left(1 + \cos^2(\theta)\right)\cos(2\phi)h_+(t) + \cos(\theta)\sin(2\phi)h_\times(t), \tag{3.17}$$

the complete antenna pattern of a Michelson Interferometer is obtained. An illustration of the antenna pattern of a Michelson Interferometer in the case of a $+$-polarized and $\times$-polarized Gravitational Wave, along with a generically polarized GW, is shown in Fig.3.2, where color indicates increasing sensitivity from indigo to red.

3.2 Real Gravitational Wave Interferometers

In Sec.3.1 it was carried out a discussion on the effect of a Gravitational Wave on a basic Michelson Interferometer and in Eq.3.15 the optimal arm length for detecting a Gravitational Wave of given frequency has been computed. A plot representing the frequency ranges in wich various GW source types are expected to be emitting and the correspondent ranges in wich various detecting methods peak their sensitivity[2] is shown in Fig.3.3. The current generation of ground-based interferometers are sensible to Gravitational Waves in the acoustic band, generated by Black Holes Binaries, Neutron Star Binaries Mergers and by Stellar Supernovae.

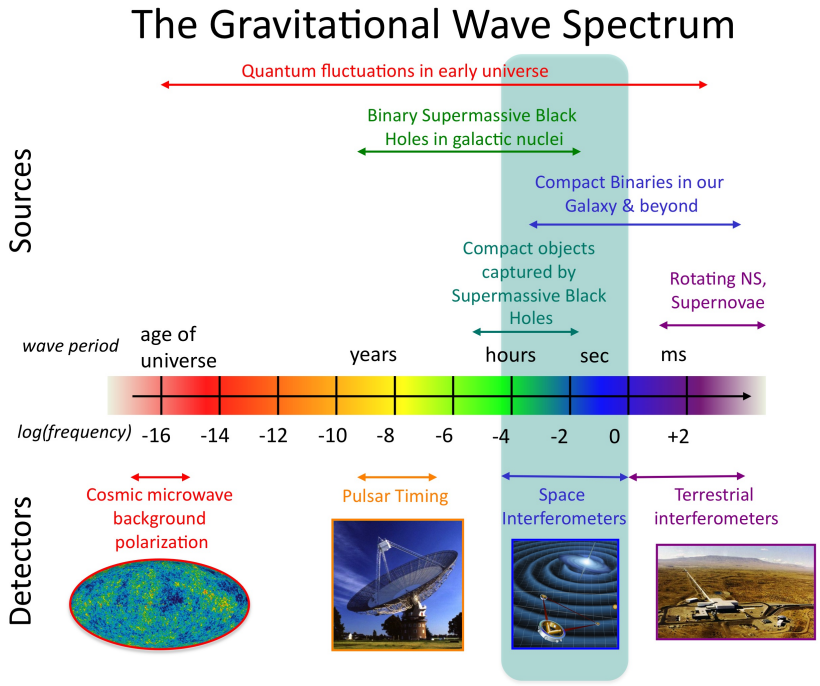

Figure 3.3: Expected Gravitational Wave Spectrum of main sources and detection methods [16].

The required arm length to optimize the detection of $[10 - 100]\,\mathrm{Hz}$ Gravitational Waves obtained from Eq.3.15 is $L \approx 10^3\,\mathrm{km}$. This is in apparent contradiction with the fact presented in Sec.1 that the LIGO and VIRGO interferometers have an arm length of $4\,\mathrm{km}$ and $3\,\mathrm{km}$ respectively. In fact the current generation of interferometers has already approached the limit length for a ground-based interferometer and even with the technological advancements that will be implemented in the next generation of Earth-bound detectors, the arm lengths of the instrument will not exceed the $10\,\mathrm{km}$ order of magnitude.
The conflict is resolved if one analyzes a realistic model for a ground-based GW interferometer, that makes use of several optical cavities to effectively increase the storage time of a photon inside the arms, while the initial estimate presented in Sec.3.1 refers to the simple Michelson Interferometer case.

[2]The only method that, at the time of writing, has been succesful in detecting Gravitational Waves is the one of ground-based Interferometers. The LISA mission is a (proposed) 2.5 million km arm triangular space interferometer that aims at detecting GW emitted in the processes related to Supermassive Black Holes in the sub-Hz band and its launch is planned for 2034 [17]. In order to detect sub-μHz GWs associated with Supermassive Black Holes it is instead proposed the Pulsar timing method, that attemps to detect anomalies in the extremely stable pulsar spinning periods as a consequence of the passage of a GW between Earth and the neutron star [18]. GWs are expected to be produced also by Quantum Fluctuations during the Cosmic Inflation period and their effect should be detectable analyzing the polarization of the Cosmic Microwave Background radiation [19].

An optical cavity is an arrangment of mirrors that allows for a closed path for a light beam. The photon is trapped between two or more mirrors for a certain amount of time of reflections (on average) before being eventually transmitted through one of the mirrors, thus increasing the beam optical path inside the interferometer arm.
As said, several types of cavities are implemented in a single ground-based interferometer, each one of which has its own peculiarities and specific aims. The most important cavities that are present in the current generation of GW interferometers are Fabry-Perot Cavities, that fold the beam path multiple times inside the interferometer arms, the Power Recycling Cavity, that reconveys the light that is leaking toward the input port back into the interferometer arms, the Input and Output Mode Cleaner Cavities, that exploit the narrow bandpass filtering property of resonant cavities to reject the unwanted normal modes that are present in the beam, and the Signal Extraction Cavity, that is tuned to enhance GW sidebands to improve the instrument sensitivity in a desired frequency range. A scheme showing the arrangement of the various cavities inside a GW interferometer can be seen in Fig.3.4.

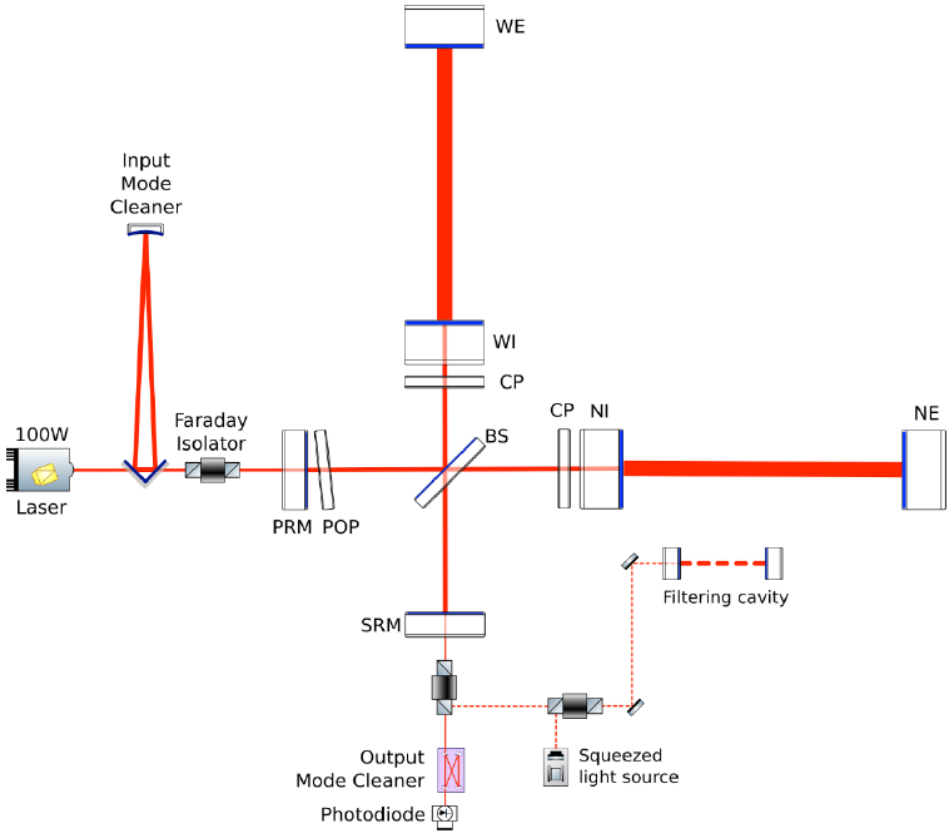

Figure 3.4: Advanced VIRGO optical configuration. BS: beam splitter; NI,WI: input test masses; NE,WE: end test masses; SRM: signal reciclying mirror. PRM: power reciclying mirror; POP: pick-off plate; CP: compensation plate.

A complete discussion of optical cavities requires the modelization of a laser beam with the paraxial approximation, that allows to decompose it in a superposition of ortho-normal modes, and performing computations of the cavity electrical field using the Circulating Field Approach [22], and it is not the scope of this work to present it in detail. As a general result it could be noted here that the effective increase of the optical path length thanks to the implementation of an optical cavity is quantified by the average number of reflections to which the photon is subject before being transmitted out of the cavity N. The average number of reflections is in turn proportional to the cavity Finesse $\mathcal{F}$, defined

by the following equation:

$$\mathcal{F} \equiv \frac{\pi\sqrt{r_1 r_2}}{1 - r_1 r_2} \tag{3.18}$$

where r_1 and r_2 are the reflection coefficients of the two mirrors of a Fabry-Perot cavity. The two quantities are related by the proportionality $N \sim 2\mathcal{F}/\pi$, so that for a Michelson interferometer with Fabry-Perot cavities there is an increase in the phase shift induced by the passage of a Gravitational Wave:

$$\Delta\phi_{FP} \approx \frac{2\mathcal{F}}{\pi}\Delta\phi_{Mich} \approx \frac{4\mathcal{F}}{\pi} h_0 k_l L. \tag{3.19}$$

Anyway the choice of the Fabry-Perot cavities Finesse in a GW interferometer is not solely dictated by detection frequency optimization based on source predicted properties but several other technical aspects must be considered in the design.
When developing in full detail the computations of the interaction between the cavities and the Gravitational Wave, the transfer function of a Fabry-Perot Interferometer is obtained [13]:

$$T_{FP}(f_{gw}) = \frac{8\mathcal{F}L}{\lambda_l} \frac{1}{\sqrt{1 + (f_{gw}/f_p)^2}} \tag{3.20}$$

where $f_p \equiv \frac{1}{4\pi\tau_s}$ is the Cavity Pole Frequency and $\tau_s = \frac{2L}{c}\frac{1}{1-r_1^2}$ is the Cavity Storage Time.

3.3 Noise Contributions in GW Interferometers

The sensitivity of the current generation of Gravitational Wave Interferometers is limited by a variety of noise contributions. Each noise source is peaked in a specific frequency range. The noises that are injected inside the detector and that propagate to the acquired output signal must be adequately refered to the input so that they can be compared to the Gravitational Wave Strain h. The sum of all the input-refered noise contribution provide the complete Noise Power Spectrum of the detector (Fig.3.5).

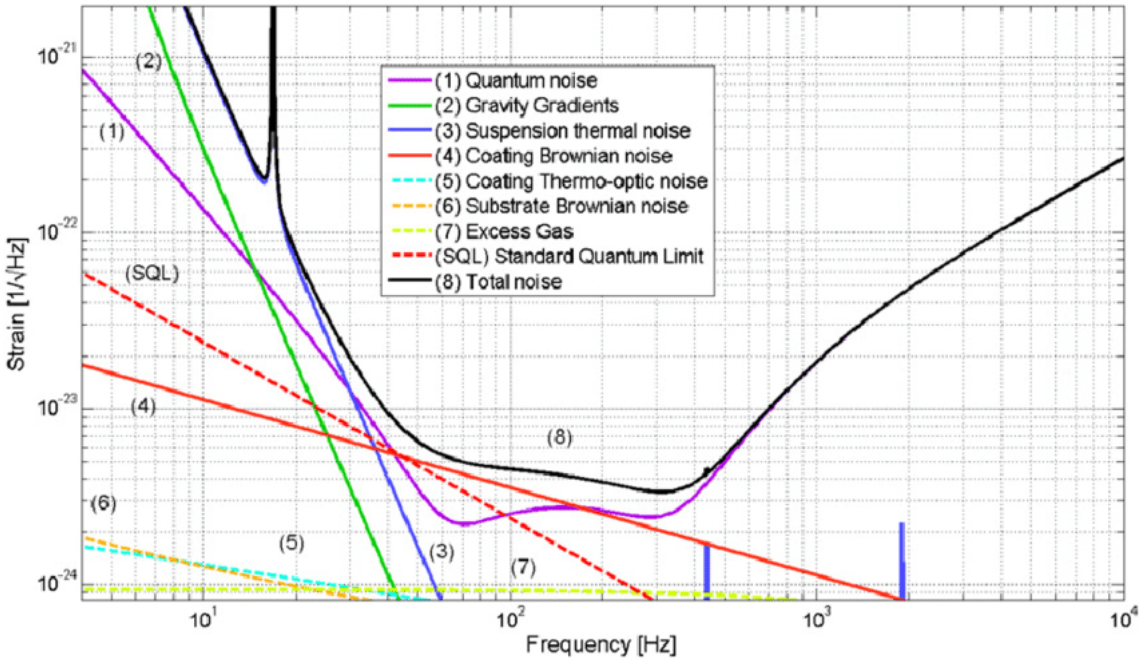

Figure 3.5: Design Sensitivity of the AdV detector [21].

There are three predominant noise contributions that limit the sensitivity of second generation Gravitational Wave interferometer sensitivities across their whole operating frequency range: Suspension

Thermal Noise for frequencies below $30 - 50$ Hz; Coating Brownian Noise[3] in the $50 - 150$ Hz frequency range; Quantum Noise for frequencies above $150 - 200$ Hz. The first two contributions are associated with classical thermal noise in test masses and their suspension systems, the random motion of particles in the mirror materials due to the fact that they are operated at non-zero temperatures, while the third contribution arises from quantum physics, in particular from photon radiation pressure and arrival statistics.

3.3.1 Quantum Noise

Quantum noise is a fundamental noise that arises due to the quantistic nature of the light beam particles which interact with mirrors and the readout system. It currently limits the sensitivity of second generation ground-based interferometer at frequencies above $150\,\mathrm{Hz}$.
Quantum noise in interferometers originates in two different phenomena. The first type of Quantum Noise is Shot Noise, that is caused by statistical fluctuations in the detected photon arrival rate by the readout apparatus. The second effect that contributes to Quantum Noise is Radiation Pressure, the pressure fluctuations on the test mass surfaces due to fluctuations in the number of photons that impinges on it.

Shot Noise Laser light is composed of discrete quanta, photons, that indipentently interact with the readout photodetector after having travelled in the interferometer. The photodetector acts as an integrator of the energy $E = \hbar\omega_l/c$ that each photon deposit on it in a certain time period T, so that the average output power measured at the photodetector is:

$$P_0 = \frac{N_\gamma \hbar \omega_l}{T} \tag{3.21}$$

where N_γ is the number of photons that interacted with the photodetector in the time interval T. The probability distribution of the process of counting discrete indepentent events, such as photon arrivals at the output port, is known to be the Poisson Distribution:

$$p(N_\gamma, \bar{N_\gamma}) = \frac{1}{N_\gamma!} \bar{N_\gamma}^{N_\gamma} e^{-\bar{N_\gamma}} \tag{3.22}$$

where $\bar{N_\gamma}$ is the average number of photons that are expected to reach the photodiode during T. For large $\bar{N_\gamma}$ the Poisson Distribution becomes a Gaussian Distribution with $\sigma = \sqrt{\bar{N_\gamma}}$. Therfore the photon arrival process in a given time interval has a fluctuation $\Delta N_\gamma = \sqrt{N_\gamma}$ that eventually translates in a power fluctuation at the photodiode:

$$(\Delta P)_{shot} = \frac{N_\gamma^{1/2} \hbar \omega_l}{T} = \left(\frac{\hbar \omega_l}{T} P_0\right)^{1/2}. \tag{3.23}$$

What was found in the above equation is just the standard deviation of output power fluctuations $(\Delta P)_{shot} = \sigma_{P,\,shot}$, wich can be expressed by definition with the integral of the Spectral Density of power fluctuations over all the frequency domain delimited by the time interval T:

$$(\Delta P)_{shot} = \sigma_{P,\,shot} = \int_0^{\frac{1}{T}} d\omega \; S_{P,\,shot}(\omega). \tag{3.24}$$

[3]Optical Coatings are stacks of alternated dielectric materials with high and low refractive index that are deposited on the surface of an optical component. If the substrate thickness is correctly dimensioned, the dielectric stack can induce a constructive/destructive interference condition for the light beam that its impinging on its outer surface, thus enhancing Reflectance/Trasmittance of the mirror respectively.

Putting together Eq.3.23 and Eq.3.24 the Spectral Density of Output Power Fluctuation caused by Shot Noise $S_{P,\,shot}(\omega) = P_0\hbar\omega_l$ is obtained, so that, as the detector output is proportional to P_0, the Relative Output Noise due to Shot Noise becomes:

$$S^{1/2}_{\Delta\phi,\,shot}(\omega) = \frac{S_{P,\,shot}(\omega)}{P_0} = \sqrt{\frac{\hbar\omega_l}{P_0}}. \tag{3.25}$$

In order to compare this output noise with the Strain h of a Gravitational Wave of frequency f_{gw} that is interacting with the interferometer, it is necessary to refer it to the detector input. That is, the Spectral Density of the Output Noise $S^{1/2}_{\Delta\phi,\,shot}(\omega)$ must be multiplied by the inverse of the transfer function of a Fabry-Perot Interferometer T_{FP} that was obtained in Eq.3.20. By accounting also for the fact that in a real GW interferometer Power Recycling Cavities are implemented to increase the circulating power inside Fabry-Perot Cavities and the not ideal efficiency of the photodiode, the interferometrical Strain Sensitivity due to Shot Noise can be expressed as:

$$S^{1/2}_{h,\,shot}(f) = \frac{S^{1/2}_{\Delta\phi,\,shot}(f)}{T_{FP}(f)} = \frac{1}{8\mathcal{F}L}\sqrt{\frac{4\pi\hbar\lambda_l c}{\eta P_{bs}}}\sqrt{1+\left(\frac{f}{f_p}\right)^2} \tag{3.26}$$

where $P_{bs} \equiv CP_0$ accounts for the power enahancement at the beam splitter due to the Power Recycling Cavity ($C = O(50-100)$) and η is the photodiode efficiency ($\eta \approx 0.9 - 0.95$).

Radiation Pressure Photons posses a momentum that is proportional to their frequency: $p = \hbar\omega_l/c$. This implies that for each laser beam photon that collides with a test mass surface the exchange of momentum can be modeled as an inelastic scattering, so that for a laser beam of power P_0 the average force that is acting on the test mass surface is:

$$F_0 = \frac{2P_0}{c} = \frac{2N_\gamma\hbar\omega_l}{Tc^2}. \tag{3.27}$$

Following an analogous reasoning to the Shot Noise paragraph, this force on the mirror surface exhibits Poissonian fluctuations around its average value due to the quantized nature of the light beam, the Spectral Density of which can be estimated as:

$$S^{1/2}_{F,\,rad} = 2\sqrt{\frac{2\hbar\omega_l P_0}{c^2}}. \tag{3.28}$$

The mirror that acts as a target for the beam is actually free to move in the horizontal plane, so that the the fluctuating force result in a mirror displacement $F = M\ddot{x}$, where M is the mirror mass. Taking the Fourier Transform of the force $\tilde{F}(f) = -M(2\pi f)^2\tilde{x}$, the Spectral Density of the mirror displacement immediately follows:

$$S^{1/2}_{x,\,rad}(f) = \frac{2}{M(2\pi f)^2}\sqrt{\frac{2\hbar\omega_l P_0}{c^2}}. \tag{3.29}$$

This fluctuating mirror displacement results in a fluctuation of the output signal that must adequately referred to the input in order to be compared with the Gravitational Wave Strain. To transform the mirror displacement into a phase shift fluctuation at the output port one must use the Fabry Perot Interferometer Transfer Function T_{FP} of Eq.3.20, but the following input referincing operation that must be performed on the output phase shift eliminates the T_{FP} dependency from the final Radiation Pressure Strain Sensitivity. However, as each photon performs $O(N \approx \frac{2\mathcal{F}}{\pi})$ bounces between the cavity mirror, it results that the power inside the cavity is larger by a factor $O(N)$ than the power P_{bs} at the beam-splitter. In fact it can be more rigorously shown that [13]:

$$P_{cav} \approx \frac{2\mathcal{F}}{\pi}P_{bs}. \tag{3.30}$$

Therefore a power fluctuation ΔP_{bs} at the input mirror gets amplified by the same factor inside the cavity $\Delta P_{cav} = \Delta P_{bs}(2\mathcal{F}/\pi)$.
Nevertheless there are a few more caveats that must be considered in order to correctly refer the mirror displacement to the input. The photons that arrive at the beam-splitter are randomly scattered into one of the two arms. As a consequence, the photon distributions in the two arms are two anti-correlated Poissonian distributions. As the interferometer is sensitive to changes in the differential length of the two arms, the contributions due to Radiation Pressure in the two arms adds up, so that the final Strain Sensitivity due to Radiation Pressure must be multiplied by a factor of 2. It can also be shown [13] that, if the mirror vibrates at a frequency f, the cavity is displaced off resonance, and the power inside the cavity is reduced by a factor $[1 + (f/f_p)^2]$. Then, the Strain Sensitivity due to Radiation Pressure results:

$$S_{h,\,rad}^{1/2}(f) = \frac{16\sqrt{2}\mathcal{F}}{ML(2\pi f)^2}\sqrt{\frac{\hbar P_{bs}}{2\pi\lambda_l c}}\frac{1}{\sqrt{1+(f/f_p)^2}}. \tag{3.31}$$

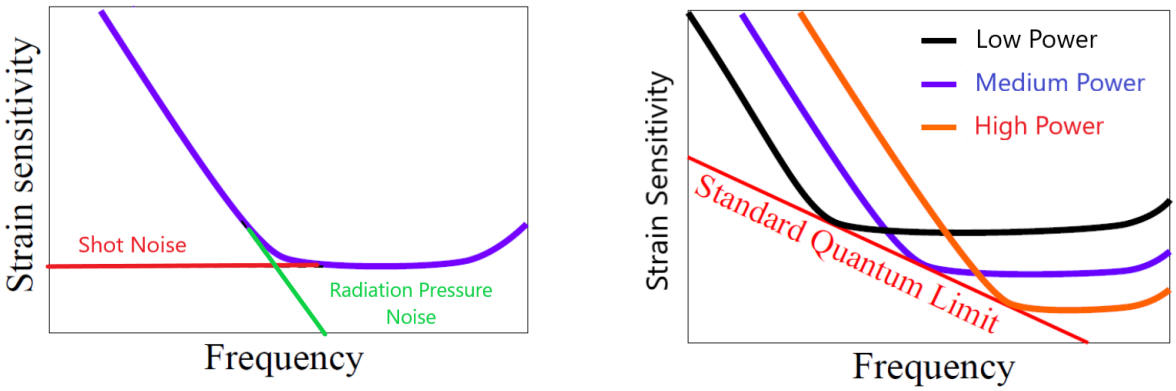

Figure 3.6: Left: Shot Noise (Red) and Radiation Pressure Noise (Green) contributions to Optical Readout Noise (Blue); Right: Standard Quantum Limit and power optimization.

The two Shot Noise and Radiation Pressure contribution quadratically add up to give the total Quantum Noise, also called Optical Readout Noise (Fig.3.6). Shot Noise is the main limiting factor for the interferometer sensitivity at high frequencies while Radiation Pressure Noise becomes relevant at lower frequencies. Moreover, it can be noted that the two noise contibutions have different dependencies on the circulating power inside the interferometer arms:

$$S_{h,\,shot}^{1/2} \propto \frac{1}{\sqrt{P_{bs}}}; \qquad S_{h,\,rad}^{1/2} \propto \sqrt{P_{bs}}. \tag{3.32}$$

What this relations are saying is that, when choosing the circulating power in the design phase of the interferometer, one cannot reduce an Optical Readout Noise contribution without increasing the other, so that a circulating power optimization process is needed to find the value that minimizes the sum of the two contributions in the frequency region of intrest. This in fact shows the remarkable fact that a (macroscopic) Gravitational Wave Interferometer aims at such an extreme accuracy in the determination of its mirror positions that its sensitivity is limited by Heisemberg Uncertainty Principle. The GW interferometer is a quantum system in which the test mass position is measured with the use of quantum particles, photons, which cause a recoil on the test mass that disturbs the measure itself.
Then, upon defining:

$$f_0 = \frac{8\mathcal{F}}{2\pi}\sqrt{\frac{P_{bs}}{\pi\lambda_l c M}} \tag{3.33}$$

the Spectral Density of the Optical Readout Noise can be written as:

$$S_{h,\,opt}^{1/2}(f) = \big(S_{h,\,shot}(f) + S_{h,\,rad}(f)\big)^{1/2} = \frac{1}{L\pi f_0}\sqrt{\frac{\hbar}{M}}\Big[\Big(1+\frac{f^2}{f_p^2}\Big) + \frac{f_0^4}{f^4}\frac{1}{1+f^2/f_p^2}\Big]^{1/2}. \quad (3.34)$$

For a given value of f, the Optical Readout Noise Spectral Density $S_{h,\,opt}^{1/2}$ can be minimized with respect to f_0[4]. The optimal value of f_0 is the one that makes equal the Shot Noise and Radiation Pressure Noise contributions, and is given by:

$$\bar{f}_0 = f\Big(1+\frac{f^2}{f_p^2}\Big)^{1/2}. \quad (3.35)$$

The corresponding set of optimal $S_{h,\,opt}^{1/2}(f)$ values defines the Standard Quantum Limit (SQL):

$$S_{h,\,SQL}^{1/2}(f) = \frac{1}{2\pi f L}\sqrt{\frac{8\hbar}{M}}. \quad (3.36)$$

The Standard Quantum Limit $S_{h,\,SQL}^{1/2}(f)$ (Fig.3.6) represents the minimum noise spectral density which can be obtained, as long as only Optical Readout Noise is concerned, at a given value of f in a Gravitational Wave Interferometer. Hence, as it is the value of f_0 that gets experimentally optimized by a change of the circulating power keeping fixed the value of f, in a GW Interferometer the Standard Quantum Limit Sensitivity can be reached at best only at a specific frequency.

3.3.2 Thermal Noise

Thermal noise in test masses and suspension systems is the current limiting factor for the sensitivity of second generation ground-based interferometer at frequencies below $200\,\mathrm{Hz}$[5]. Thermal noise in the suspension systems primarily arises from losses in the fused silica fibers that hang the test mass to the attenuator structure. This contribution needs to be numerically computed with finite-elements models that include bulk, surface and thermoelastic components of the fibre material and that account for the specific noise-reducing fibre shape. Thermal noise in test masses on the other hand can be adequately studied using analytical models.

There are two fundamental origins of thermal noise in optical components. The first is the standard Brownian Noise, due to the thermal energy of the jittering atoms of the test mass that causes a thermally driven fluctuation of the reflective surface of the element. Thermal energy k_bT is present as soon as the component is operated at non-zero temperatures.
The second component is a less intuitive form of thermal noise that arises from temperature fluctuations. The local microscopic temperature of a component is not a constant value but fluctuates around an average temperature T. Due to the fact that many material properties, like the coefficient of thermal expansion α or the refractive index n, are temperature dependent, temperature fluctuations induces phase and position fluctuations. The process that is associated with α is called Thermo-Elastic Noise whereas other processes are referred to as Thermo-Refractive Noise or Thermo-Optic Noise.

[4]That is, it can be minimized with respect to the circulating power inside the interferometer arms, as $f_0 \propto \mathcal{F}\sqrt{P_{bs}}$.

[5]There are also other technical noises sources, such as seismic noise, that significantly contribute to the overall noise in the sub-$200\,\mathrm{Hz}$ region, but they will not be examined in detail in this work.

Brownian Thermal Noise Brownian Noise of the Bulk Material of the interferometer mirrors can be calculated by direct application of the Fluctuation-Dissipation (FD) Theorem. In a Gravitational Wave Interferometer a laser beam is shining on the surface of the cylindrical test masses. The light reflected by the mirrors acquires a phase shift that contains information about the displacement of the test mass surface. Brownian Thermal Noise induces vibrations in the test mass rest position $x(t)$ in the horizontal plane that gets eventually converted in a phase shift at the output port. Then the first thing to be done in order to analyze Brownian Thermal Noise in bulk material is to find the Spectral Density $S^{1/2}_{x,\,Bulk}(f)$ of its induced fluctuations in $x(t)$. Throughout the derivation is assumed that the mirror surface is infinite in size, so that the boundary effects of the beam-test mass interaction are negligible, and that the test mass is in thermal equilibrium at temperature T.
In its most general form the Fluctuation-Dissipation Theorem states that the Thermal Noise Spectral Density of a generic readout variable is given by [23]:

$$S_x^{1/2}(f) = \frac{k_b T}{\pi^2 f^2} \big| \operatorname{Re}[Z(f)] \big| \tag{3.37}$$

where k_b is Boltzman's constant. The complex impedance $Z(t)$ can be computed by applying a generalized force $F(t)$ to the test mass that will generate a consequent time evolution of the observable variable $x(t)$. By denoting with $F(f)$ and $x(f)$ the Fourier Transforms of the driving force and the readout variable respectively, the Fourier Transform of the complex impedance $Z(f)$ is expressed as:

$$Z(f) = 2\pi i f \frac{x(f)}{F(f)}. \tag{3.38}$$

In the case of thermal noise in the Gaussian Beam-Test Mass system, the arbitrary driving force can be modelled with an oscillating force which intensity is gaussianly distributed across the mirror surface. This will result in an oscillating pressure acting on the mirror surface:

$$P(\bar{r}, t) = F_0 \cos(2\pi f\, t) f(\bar{r}) \tag{3.39}$$

where $f(\bar{r}) = \frac{1}{\pi r_0^2} e^{-r^2/r_0^2}$ is the gaussian intensity profile. This oscillating driving force will consequently feed a dissipated power W_{diss} in the test mass due to internal frictions. Then it can be shown [24] that for the above configuration the real part of the Fourier Transform of the system complex impedance is given by:

$$\big| \operatorname{Re}[Z(f)] \big| = \frac{2W_{diss}}{F_0^2}. \tag{3.40}$$

Inserting Eq.3.40 in the FD Theorem 3.37, the following relation is obtained:

$$S_x^{1/2}(f) = \frac{2k_b T}{\pi^2 f^2} \frac{W_{diss}}{F_0^2}. \tag{3.41}$$

Then, assuming homogeneous dissipation, the W_{diss} power that is absorbed by the mirror can be expressed as:

$$W_{diss} = 2\pi f U_{max} \phi^{Bulk}(f). \tag{3.42}$$

In the above equation $\phi^{Bulk}(f)$ is the Mechanical Loss Angle of the mirror material, while U_{max} is the elastic deformation energy in the instant when the test mass is maximally contracted or extended under the action of the oscillatory pressure 3.39. Then, under the above assumptions, an explicit expression for U_{max} can be derived for the Gaussian Beam-Test Mass system ([24], [25]):

$$U_{max} \approx \frac{F_0^2(1-\nu)}{2\pi^{1/2} Y_s r_0} \tag{3.43}$$

where ν and Y_s are the Poisson's Ratio and the Young's Modulus of the material respectively. Eq.3.43 is valid up to first order corrections $O(r_0/R)$, where r_0 is the Gaussian Beam Radius and R the Characteristic Size of the cylindrical Test Mass. Substituting Eq.3.42 and Eq.3.43 back into Eq.3.41, it is finally obtained an expression for the Mirror Displacement Spectrum of Brownian Thermal Noise in the Test Mass Bulk Material:

$$S^{1/2}_{x,\,Bulk}(f,T) = 2k_bT\frac{1-\nu}{\pi^{3/2}fY_sr_0}\phi^{Bulk}. \tag{3.44}$$

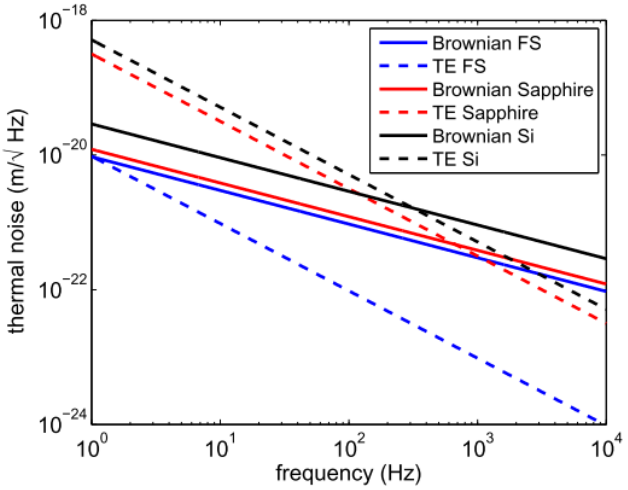

Figure 3.7: Comparison of the Brownian and Thermo-Elastic noise at room temperature (300K) for various Advanced Detectors Test Masses candidate materials (Fused Silica, Sapphire, Silicon).

Similar to Brownian Thermal Noise in the bulk materials of the test mass, the coatings also show Brownian thermal noise. An analogous computation can be perform to extract the Mirror Displacement Spectrum of Brownian Thermal Noise in Coatings [25]:

$$S^{1/2}_{x,\,Coat}(f,T) = 2k_bT\frac{1-\nu}{\pi^{3/2}fY_sr_0}\phi^{Coat}_{eff}. \tag{3.45}$$

In the above equation ν and Y_s still refer to Poisson's Ratio and Young's Modulus of the bulk material, while ϕ^{Coat}_{eff} is an effective Loss Angle for the Coating Stack of Dielectric Materials, the final form of which has a detailed expression that needs further assumptions and computations to be obtained[6] [26].

In order to properly compare the Brownian Thermal Noise displacement spectra obtained in Eq.3.44 and Eq.3.45 with Gravitational Wave Strain h, they must be refered to the input. This can be easily made by remembering that the effect of a Gravitational Wave on the length L of a Fabry-Perot Cavity is to change it by the amount $\Delta L = hL$. This implies that, in order to input refer the mirror displacement induced by Thermal Noise, it must be divided by the cavity length L so that the effect is equivalent to a Gravitational Wave of strain h. As opposed to Quantum Noise, the Finesse of the cavity does not

[6]For completeness, it can be shown the result obtained in [26] for the effective Coating Loss Angle, which is valid for small Poisson's Ratio of the coating materials:

$$\phi^{Coat}_{eff} = \frac{t}{\sqrt{\pi}r_0}\left(\frac{Y_s}{Y_\perp}\phi_\perp + \frac{Y_\parallel}{Y_s}\phi_\parallel\right)$$

where t is the total thickness of the coating layer. The effective Young's Moduli $Y_\perp$, $Y_\parallel$ and Loss Angles $\phi_\perp$, $\phi_\parallel$ in the above expression are defined in terms of the coating materials Young Moduli Y_i, Loss Angles ϕ_i and thicknesses t_i ($i = 1, 2$

enter here in the input referring operation, as both GW and Thermal Noise effects get amplified by the same factor $O(N)$ inside the cavity.
Then, the Strain Spectral Density of Brownian Noise in Bulk Materials and Coatings, is simply given by:

$$S^{1/2}_{h,\,Bulk}(f,T) = \frac{2k_bT}{L}\frac{1-\nu}{\pi^{3/2}fY_sr_0}\phi^{Bulk}; \tag{3.46}$$

$$S^{1/2}_{h,\,Coat}(f,T) = \frac{2k_bT}{L}\frac{1-\nu}{\pi^{3/2}fY_sr_0}\phi^{Coat}_{eff}. \tag{3.47}$$

Thermo-Elastic Noise Thermo-Elastic Noise of the Bulk Material arises from stochastic temperature fluctuations that are translated into displacement noise by means of the coefficient of thermal expansion α. Its contribution to the total Thermal Noise can becomputed by applying the Fluctuation-Dissipation Theorem, in analogy to the Brownian Thermal Noise estimate in the previous paragraph. The estimate of the complex impeadance requires lengthier computations in this case, as it must be derived by solving the system of the thermal conductivity and strain-displacement equations for the mirror [27], assuming that the only dissipation mechanism in the mirror is thermo-elastic damping and approximating the mirror as an half space. Refering to [28] for detailed computations, the displacement spectrum of Thermo-Elastic Noise in Bulk Materials is given by:

$$S^{1/2}_{TE,\,bulk}(f,T) = \frac{8}{\sqrt{2\pi}}\alpha^2(1+\nu)^2\frac{k_bT^2\kappa}{\rho^2c_p^2f^2r_0^2} \tag{3.48}$$

where ρ,κ and c_p are the density, thermal conductivity and specific heat capacity of the material respectively. The above equation is valid in the 'adiabatic' regime, that is if the thermal diffusion lenght of the material l_{th} is smaller than the beam diameter r_0. The thermal diffusion length of is defined as:

$$l_{th} = \sqrt{\frac{a^2}{f}} = \sqrt{\frac{\kappa}{\rho c_p f}} < r_0. \tag{3.49}$$

Outside of the adiabatic regime the thermo-elastic effect gets weaker. This is because the adiabatic condition 3.49 corresponds to the requirement that, during one period of oscillation, all temperature fluctuations that are present at the observation volume stay inside this volume. Then, if thermal conductivity is increased or lower frequencies are considered, l_{th} gets larger and the temperature fluctuations are averaged out faster.
The non-adiabatic regime correction becomes important for low temperature applications, as most optical materials exhibit a peak in the thermal conductivity at cryogenic temperatures. A detailed calculation can be performed to estimate the displacement noise for Thermo-Elastic Noise incorporating the non-adiabatic case [29], that can be expressed as:

$$S^{1/2}_{TE,\,bulk}(f,T) = \frac{8}{\sqrt{2\pi}}\alpha^2(1+\nu)^2\frac{k_bT^2r_0}{\kappa}J\left[\Omega\right] \tag{3.50}$$

indicates the different coating layer materials) as:

$$Y_\perp = \frac{t_1+t_2}{\frac{t_1}{Y_1}+\frac{t_2}{Y_2}},$$
$$Y_\parallel = \frac{Y_1t_1+Y_2t_2}{t_1+t_2},$$
$$\phi_\perp = \frac{Y_\perp}{t_1+t_2}\Big(\frac{t_1}{Y_1}\phi_1+\frac{t_2}{Y_2}\phi_2\Big),$$
$$\phi_\parallel = \frac{Y_1t_1\phi_1+Y_2t_2\phi_2}{Y_\parallel(t_1+t_2)}.$$

where $J[\Omega]$ is a function of the dimensionless variable $\Omega = \omega/\omega_c$ that quantifies the relative frequency compared to the adiabatic limit frequency $\omega_c = a^2/r_0^2$:

$$J[\Omega] = \sqrt{\frac{2}{\pi^3}} \int_0^\infty du \int_{-\infty}^\infty dv \, \frac{u^3 e^{-u^2/2}}{(u^2+v^2)\big((u^2+v^2)^2+\Omega^2\big)} \tag{3.51}$$

3.3.3 Other Noises

Despite the fact that the noise sources that were analyzed in the previous sections are the dominant contribution across all the operating frequency range of currently operating interferometers, there are other noise sources that contribute to the general noise budget of the detector. In fact these alternative noise contribution are not secondary as they have a significant indirect effect on the overall noise budget, as the effort to minimize them eventually reflects in a Thermal Noise increase or in a financial cost increase that subtracts precious resources to major noise contributions suppression. Detailed evaluation of all noise sources is crucial during the design phase of an interferometer and in the case of new generation detectors it will be even more important to extensively account for all possible contributions.

Seismic Noise Earth's ground is in perpetual motion, with an average vibration amplitude of $O(10^{-6}\,\mathrm{m})$. There are different causes of different nature that contribute to this continual vibration. In the $1-10\,\mathrm{Hz}$ region Cultural Noise, that is ground vibration caused by human activities and infrastructures such as road and train traffic, and wind noise are the main contibutions. This adds up to the micro-seismic background that affect GW Interferometers in the form of surface waves that ultimately shake test masses.
The amplitude of the Seismic Noise vibration are more than ten orders of magnitude larger than the mirror displacemnt values that a GW interferometer aims to detect, so that there is need for a dedicate suspension system that is able to decouple the test masses from surrounding oscillations. A typical suspension chain is obtained cascading a set of passive mechanical filters providing a suited attenuation from seismic and acoustic noise above a certain cut-off frequency. Below this frequency value an active feed-back control strategy is developed by using sensors and actuators disseminated along the suspension chain and keeping the interferometer at its working point via feedback systems.

In the VIRGO interferometer, the upper part of the suspension chain is called SuperAttenuator (Fig.3.8) and it is essentially a N-stage pendulum supported by a three-leg elastic structure, called Inverted Pendulum. In an N-stage pendulum, at much higher frequencies than its normal modes, the horizontal displacement of the suspension point is transmitted to the last stage with an attenuation proportional to f^{-2N}. This exponential attenuation factor allows to reach the desired seismic noise suppression level in second generation interferometers with a 5-stage pendulum.
The Optical Payload is intead the last suspension stage and it is designed to couple the test mass to the SA chain, as well as steering the mirror through internal forces exerted from the last Superattenuator element to compensate the residual Seismic Noise at lower frequencies. This end structure is formed by two active components, the Marionette that is used to control the mirror position by means of coil-magnet actuators acting between the last stage upper part suspension and the marionette arms itself, and the Recoil Mass that is used to protect and steer the mirror. Particular attention has to be focused on the mechanical elements which connect the mirror to the last suspension stage as they can easily degrade the intrinsic mechanical losses of the system. In order to suppress mechanical losses that happen at interfaces of different materials, the test mass-suspension wire system in the advanced second generation detector is made from a monolithic element of fused silica.

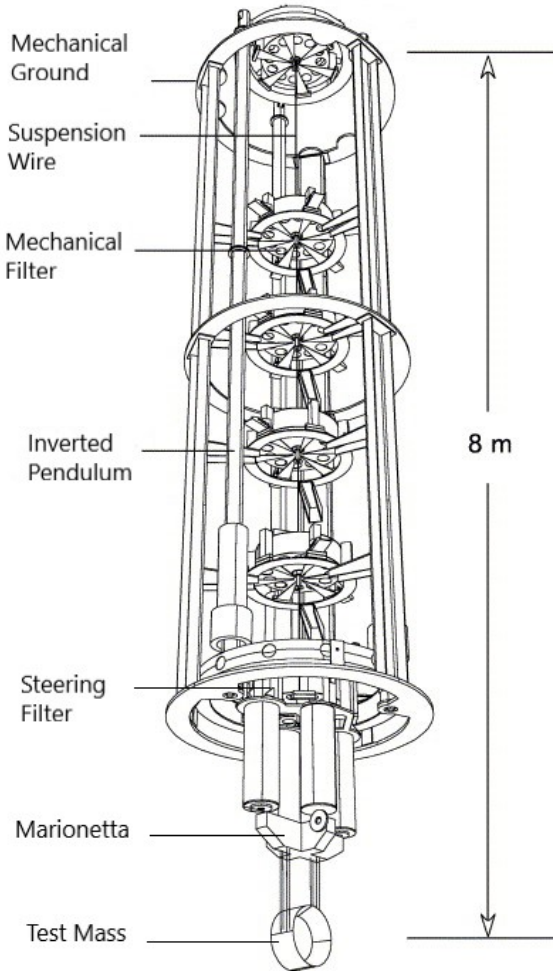

Figure 3.8: Scheme of VIRGO's SuperAttenuator.

Newtonian Noise Stochastic fluctuations of the local gravitational field are usually referred to as Newtonian Noise or Gravity Gradient Noise. Local variations in the gravitational field result in a newtonian force acting on the test masses, in analogy to the ones exerted by Gravitational Wave perturbations. The most important Newtonian Noise contribution comes from micro-seismic noise, which produces mass density fluctuations, and consequently gravitational field fluctuations, in the Earth's ground that surround the detector. Modern GW interferometers are so sensitive that even the changing gravitational attraction of water clouds due to atmospheric turbulences gives a non negligible contribution to Newtonian Noise.
Gravity Gradient Noise is the most fundamental type of noise, in the sense that there is no way to shield it, otherwise Gravitational Wave induced perturbations would be shielded too. There are different available strategies that can be employed to mitigate the impact of Gravity Gradient Noise. An active strategy consists in deploying a network of sensors to measure ground displacement and atmospheric pressure variations so that their effect on the mirrors can be modelled and subtracted from Gravitational Wave signals. A passive strategy for minimizing Newtonian Noise consists instead in building the interferometer in an underground site to reduce the impact of atmospheric perturbations, as it was done for the Large Scale Cryogenic Gravitational Wave Telescope (LCGT) located in the Kamioka mine, Japan.

Scattering and n Noise Ambient pressure air exhibits refraction index n fluctuations. The noise associated with the change of optical path that would be injected in the interferometrical system if

the laser beam was travelling in ambient pressure air would be larger than the design sensitivity of the detector. To minimize the n fluctuations induced noise the light beam in Advanced Gravitational Wave interferometers travels inside an ultra-high vacuum pipe, with pressure of $O(10^{-9}\,\mathrm{mbar})$[7]. Moreover, the residual gas must be free of condensable organic molecules, in order to keep the optical surfaces clean.

Also scattered light inside the arms constitutes a relevant noise source in GW interferometers, as it can interact with the pipe walls, thereby getting modulated by its seismic noise, and then get rediffused back in the beam by reflection on a mirror. As a consequence, diffusion of circulating light inside the Fabry-Perot cavities must be kept below few parts per million. For this purpose, cavity mirrors are polished to a 0.5Å rms micro-roughness over a diameter of $O(20\,\mathrm{cm})$.

[7]The vacuum pipes enclose all the interferometer arm, so that they are $3-4\,\mathrm{km}$ in lenght and around $1.2\,\mathrm{m}$ in diameter in order to contain the diffraction-limited laser beam. This results in a total volume of about $9000\,\mathrm{m}^3$, that is larger than the LEP particle accelerator at CERN. Pumping such a huge volume to ultra-high vacuum pressure constitutes not only a technological challenge but also a source of issues and delays in case of incidents inside the arms.

Chapter 4

The Einstein Telescope

The second generation of Gravitational Wave Interferometers has succeded in the first detection of a Gravitational Wave Signal in 2015 and in the last few years, thanks to periodical improvements in the detector set-ups and readout systems, the frequency of the claims of new GW signals constantly increased, bringing the total number of confirmed event detections up to fifty. Despite the huge importance of this achievement, that ultimately led to the assignment of the 2017 Nobel Prize in Physics to three scientist that played a key role in the foundation of the LIGO/VIRGO Collaboration (K.Thorne, R.Weiss, B.C. Barish), the quantity and signal-to-noise ratio of the detections made in second generation detectors is still too low for precise astronomical studies of the GW sources and for consistently complementing optical and X–ray observations in the study of fundamental systems and processes in the Universe. An increase of the Signal-to-Noise Ratio in the detected signal could also be crucial to investigate over beyond General Relativity theories, as the relativistic description of compact object mergers breaks down in the last collision and ringdown instants of the event.
Due to these considerations, starting from the late '00s, the Gravitational Wave community started investigating a third generation of detectors with a considerably improved sensitivity that will open the era of routine GW astronomy. The Einstein gravitational wave Telescope (ET) is an European Collaboration project for a third generation GW Interferometer that will aim at a sensitivity about a factor 10 better than the current advanced detectors. Research and development on the innovative technologies that are needed to reach ET ambitious design sensitivity have slowly but steadily evolved in the last decade and the project is now mature to receive official approval from the institutions for the start of its construction phase. Moreover another third generation detector, the Cosmic Explorer funded by the United States of America, is planned to support Einstein Telescope observations.
Einstein Telescope Design encompasses most of the technological features that allowed second generation interferometers to achieve the first Gravitational Wave detections but will also implement new solutions to reduce the fundamental and technical noises that currently limit the sensitivity of advanced LIGO and VIRGO detectors. In these last years that precede construction, research on new candidate materials and technologies for the ET Interferometers are flourishing and this thesis work wishes to contribute to the developement by performing an innovative optical absorption measurment in silicon crystals at cryogenic temperatures. In order to understand why it is crucial for the next generation interferometers to characterize the properties of optical substrate materials at cryogenic temperatures, it is necessary to present a brief analysis of the main strategies and technological features that are included in the Einstein Telescope design to attempt at improving second generation sensitivity over a wide range of frequencies.

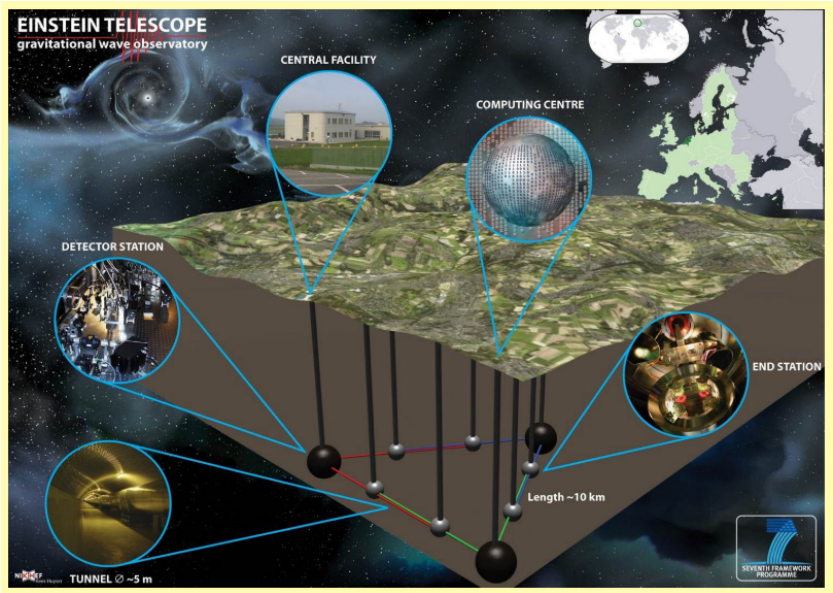

Figure 4.1: Artist's view of Einstein Telescope.

4.1 Detector Layout

In Sec.3.3 the main noise contribution that limits the sensitivities of the currently operating ground-based detectors were discussed and their spectral densities were derived. The main feature of a second generation dector noise budget were highlighted: thermal noise is the limiting factor for frequencies below $100 - 200\,\mathrm{Hz}$ while quantum noise becomes the dominant contribution at higher frequencies. Einstein Telescope aims at improving second generation performances over the entire detection frequency band from few Hz to $10\,\mathrm{kHz}$, so that it is needed to adress both the main limiting noise contributions in a single detector.
In order to find a strategy to achieve this wideband sensitivity improvement, it is useful to recall the Brownian Thermal Noise and Shot Noise spectral density that were derived in Eq.3.26 and Eq.3.46:

$$\begin{aligned} S^{1/2}_{h,\,brown}(f) =& \frac{2k_bT}{L}\frac{1-\nu}{\pi^{3/2}fY_sr_0}\phi; \\ S^{1/2}_{h,\,shot}(f) =& \frac{1}{8\mathcal{F}L}\sqrt{\frac{4\pi\hbar\lambda_l c}{\eta P_{bs}}}\sqrt{1+\left(\frac{f}{f_p}\right)^2}. \end{aligned} \tag{4.1}$$

In the above expressions it is manifest that the most intuitive approach to reduce both noise contributions is to elongate the interferometer arms ($S^{1/2}_{h,\,brown}$, $S^{1/2}_{h,\,shot} \propto L^{-1}$). This strategy will be followed in Einstein Teslescope interferometers, as their arms are planned to be $10\,\mathrm{km}$ in length. This design arm length is in fact close to the maximum achievable arm length for a ground-based interferometer, considering in particular that the third generation of Gravitational Wave interferometers will be built in underground sites to reduce Newtonian Noise[1].
If one then desires to further reduce shot noise, the only viable strategy is to increase the circulating power inside the interferometer arms, either by increasing the input power at the beam splitter or the cavity Finesse ($S^{1/2}_{h,\,shot} \propto \mathcal{F}^{-1}$, $P_{bs}^{-1/2}$). This is however detrimental for the Brownian Thermal Noise contribution because raising the circulating power inside the Fabry-Perot Cavities would increase the temperature of the mirrors ($S^{1/2}_{h,\,brown} \propto T$). One could think of preventing this problem by enlarging the section of the mirror suspensions so to have a better evacuation of the excess absorbed power, but

[1]The arm length limiting factor is not so much the technological aspect of managing a very long armed interferometer, but rather the economical cost that comes from building and operating an underground facility of such dimensions.

this would in turn increase the Suspension Thermal Noise, that is the actual limiting factor for the detector sensitivity below $10\,\mathrm{Hz}$, besides spoiling Seismic Isolation.
Hence there are no other efficient strategies that allows to tackle both Thermal Noise and Shot Noise in a single interferometer than increasing the arm length. For this reason Einstein Telescope follows a different approach respect to second generation GW interferometers, that is to build a pair of parallel interferometers, one of which can be optimized for low frequency detection ($2 - 40\,\mathrm{Hz}$) while the second can be independently tuned for higher frequencies observation.

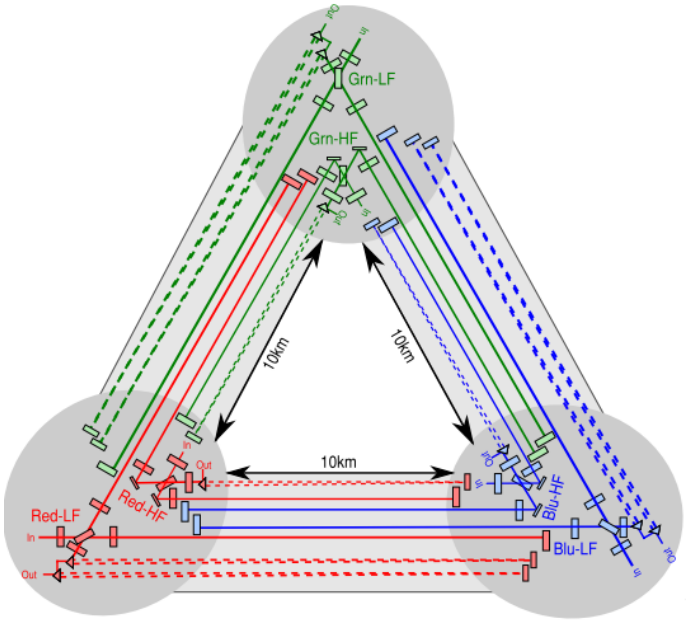

Figure 4.2: The final Xylophone Configuration for Einstein Telescope.

The final construction stage of the Einstein Telescope will consist of three nested detectors, each one formed by an aligned pair of dual-recycled Michelson Interferometers with Fabry-Perot Cavities, arranged in a triangular configuration (Xylophone Configuration), as shown in Fig.4.2. It can be shown that the sensitivity of a triangular configuration is comparable to the one of a right-angled interferometer with same construction parmeters, while offering a more isotropic antenna pattern [30].
The interferometers will be built in an underground location ($100 - 200\,\mathrm{m}$ below surface) to minimize Seismic and Newtonian Noise contributions that would spoil detector sensitivity at frequencies below $10\,\mathrm{Hz}$. Research is ongoing to find a site in Europe that offers an high level of geologic and seismologic stability, while possibly presenting an already existing infrastructure to cut costs and time on tunnel and shaft construction. In order to isolate test masses from ground seismic vibrations and local disturbances, each one of them will be hanged to a suspension system with similar structure to the ones employed in second generation interferometers.

4.2 Detector Noise Budget

The design sensitivity for a single pair of High Frequency and Low Frequency interferometers of the Einstein Telescope detector is shown in Fig.4.3, together with the detailed noise budget for both HF and LF detectors. Different strategies are employed in the two HF and LF interferometers to adress the dominant noise contributions in each frequency range of intrest.
Quantum Shot Noise will be the main limiting factor for the High Frequency detector at frequencies above 200Hz. As shown in the expression for the Shot Noise Spectral Density that was obtained in the previous chapter (Eq.3.26), for minimizing it the circulating power in the interferometer arms needs to

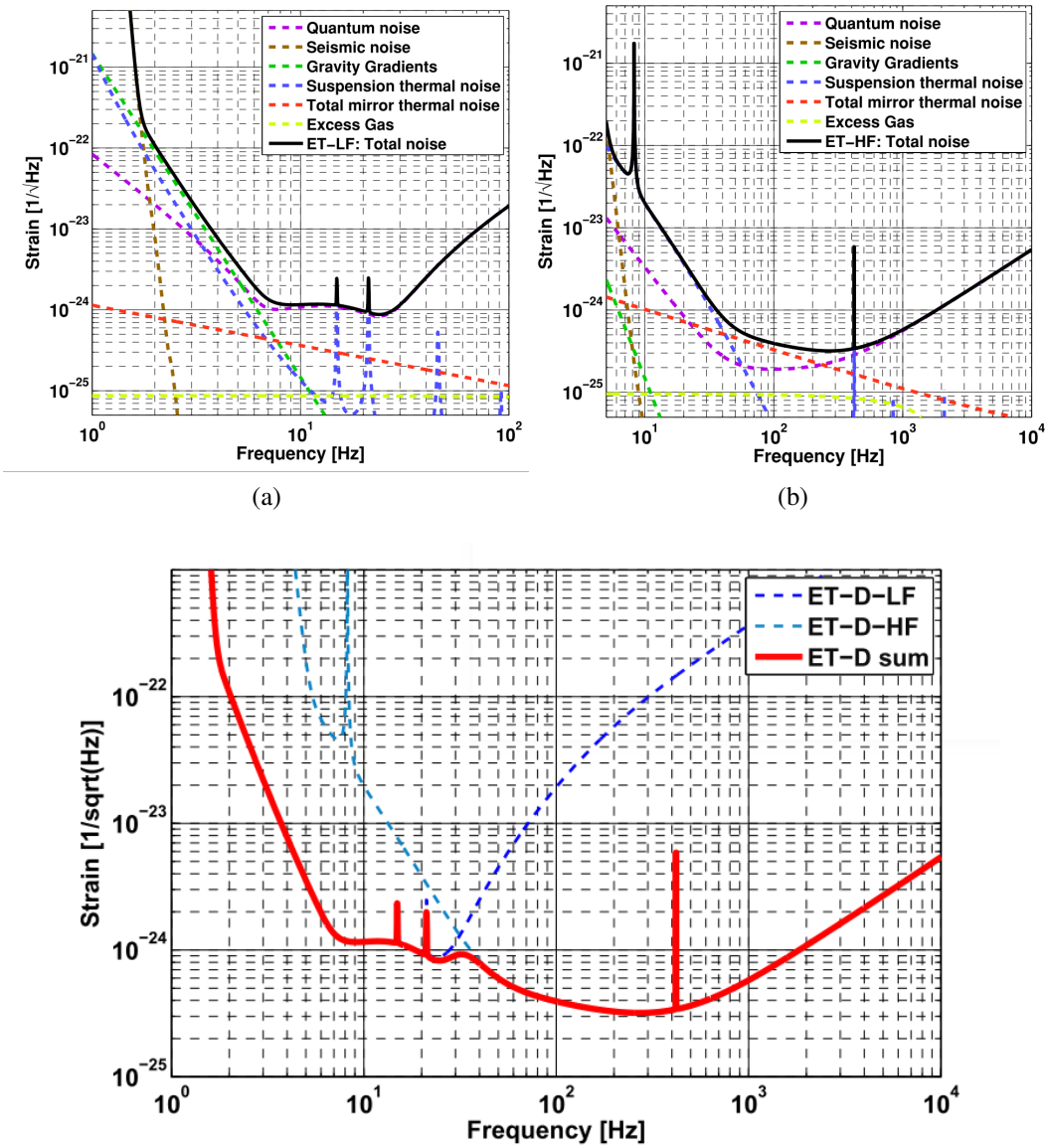

Figure 4.3: Design Sensitivity for the Low Frequency (a), High Frequency (b) and LF-HF sum (c) detectors of Einstein Telescope [31].

be increased as much as possible. Design specifications aim at operating the HF interferometer with a light power of $O(10^6\,\mathrm{W})$ inside the Fabry-Perot Cavities[2]. As a consequence the HF interferometer must be operated at room temperature, since material and coating technologies are not mature enough to handle a several MegaWatt power in input to the test masses. The massive circulating power that acts on the test masses and the high operating temperature cause the High Frequency Detector sensitivity between $40\,\mathrm{Hz}$ and $200\,\mathrm{Hz}$ to be limited by mirror thermal noise. Another important implication of the fact that the HF interferometer will be operated at room temperature is that all the succesful technological solutions developed for test mass coatings and suspension systems in second generation detectors can be directly implemented, as the input laser will be operated at usual $1064\,\mathrm{nm}$ wavelength and the mirrors will be built from fused silica.
The crossover frequency of the sensitivities of the LF and HF interferometers is at about $35\,\mathrm{Hz}$. For frequencies below $1.7\,\mathrm{Hz}$, the Low Frequency Detector sensitivity will be limited by seismic noise.

[2]For comparison, the maximum circulating power that is designed to be hold inside aLIGO arm cavities is $750\,\mathrm{kW}$, five times lower than the $3\,\mathrm{MW}$ design circulating power for the High Frequency ET detector.

In order to minimize the Seismic Noise contribution and to push its relevance at the lowest possible frequencies, a modified version of the VIRGO SuperAttenuatur will be developed to decouple the test masses from gruond vibration. The Modified SuperAttenuator will consist of 6 mechanical filters for a total chain height of $17\,\mathrm{m}$, compared to the $9\,\mathrm{m}$ with 5 filters configuration of the VIRGO suspension system. Newtonian Noise limits the LF detector sensitivity in the $[1.7 - 6]$ Hz frquency range. As already discussed in Sec.3.3, the only possible approach to Newtonian Noise mitigation is post-processing subtraction. To this purpose a set of displacement sensors will be placed all around the interferometers arms to monitor for ground mass displacement of seismic origin, in the hope that it will be possible to correlate the independently recorder ground displacement with mirror displacement detected by the interferometer. The Gravity Gradient Noise subtraction strategy for ET is still undeveloped at the time of writing, so that the curves shown in Fig.4.3 show a conservative estimate for the NN contribution. After the sensor array for Newtonian Noise subtractiobn will be completed, Suspension Thermal Noise will become the limiting factor in the $[1.7 - 6]$ Hz frequency band. Ultimately, Quantum Noise will be the limiting factor also in the Low Frequency Detector, at frequencies above $6\,\mathrm{Hz}$.
Quantum Noise will limit the sensitivities of both LF and HF detectors of Einstein Telescope, either in the form of Shot Noise or Radiation Pressure Noise. Apart from the conventional Quantum Noise minimization strategies such as the sharp circulating power increase inside the HF Fabry-Perot cavities, that are capable of decreasing a single QN contribution at the expense of an increase in the second contribution, a broadband Quantum Noise reduction can be obtained with the injection of squeezed states of light with a frequency-dependent squeezing angle into the output port of the interferometer [34]. An electro-magnetic field is in a squeezed state if the quantum uncertainty of one of its quadrature is smaller than the one of a coherent state, at the expense of a larger quantum uncertainty associated to its conjugated quadrature, to fulfill Heisenberg's uncertainty principle. Then the squeezing angle can be oriented in a frequency dependent way so that phase fluctuation noise is reduced in the frequency band where Shot Noise is more relevant, increasing the contribution of the irrelevant Radiation Pressure noise due to increased amplitude fluctuations, and viceversa, thus overcoming the Standard Quantum Limit in a wide frequency range. A frequency dependent squeezing source that is capable of reaching at least $4\,\mathrm{dB}$ of broadband quantum noise reduction has been realized both in KAGRA and LIGO sites ([35],[36]). An implementation of the FDS technology in all advanced interferometers is planned for the start of the O4 acquisition run (2022/23).

4.3 Scientific Reach of the Einstein Telescope

A third generation Gravitational Wave Interferometer such as the Einstein Telescope will make it possible to observe a variety of the most extreme phenomena in the universe, providing a new tool for expanding our knowledge of fundamental physics, cosmology and relativistic astrophysics. First of all, Einstein Telescope pledge to detect the same type of events that were observed during the first data-taking runs of the aLIGO and AdV detectors, but at larger distances, hence dramatically increasing the detection frequency, allowing to build up a solid statistic in compact binary mergers analysis. The new generation detector is expected to observe BNS up to a redshift of $z \sim 2$, stellar-mass BBH population at the edge of the Universe ($z \sim 15$) and intermediate-mass BBH out to a typical redshift of $z \sim 5$[3]. Moreover ET is expected to be sensitive to Gravitational Wave signals of different nature respect to the ones already observed, such as supernovae collapse out to a distance of $1.5 \times 10^7\,\mathrm{ly}$, within which the expected event rate is $1/\,\mathrm{year}$. Other important classes of gravitational wave events that could be detected by an instrument with a sensitivity as the one that was presented in Fig.4.3 are, for instance, gravitational collapses associated with Gamma Ray Bursts, isolated Neutron Star GW

[3]For comparison, the most distant events that were identified with the aLIGO and AdV detectors are located at distances of $O(z = 0.1)$.

signals or even the Primordial Gravitational Wave Background.
The following section aims at presenting the main scientific objectives of the Einstein Telescope project and the open issues in physics that could be addressed by enhancing the range of Gravitational Wave observations.

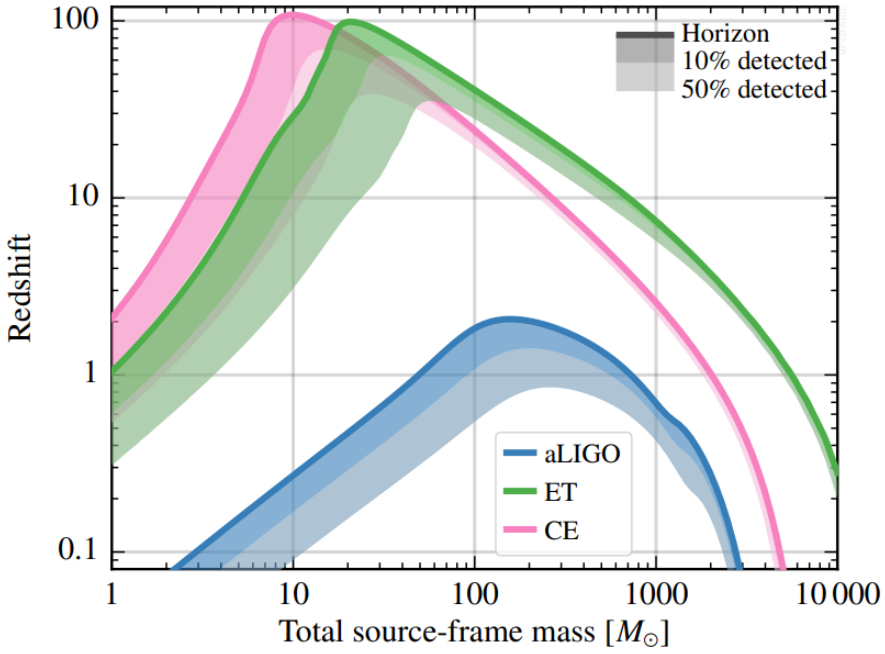

Figure 4.4: Astrophysical reach of the Einstein Telescope for equal-mass, nonspinning binaries isotropically distributed in sky location and inclination, compared to one of the aLIGO and Cosmic Explorer detectors [33].

4.3.1 Fundamental physics and strong field tests of General Relativity

Einstein Telescope will be capable of observing sources in dense enviroments of ultra-strong gravity and will therefore provide a cosmic laboratory for understanding phenomena and matter in extreme conditions of density, temperature, and magnetic fields. The detection of such events can potentially answer astonishing questions in fundamental physics. Moreover, an instrument with improved sensitivity respect to the currently operating advanced detectors will give a clearer picture of BBH interaction close to the merger phase, providing an insights into the nature of Black Holes spacetimes and of gravity in ultra-strong fields.

Polarization of gravitational waves According to the theory of General Relativity, Gravitational Waves have only two polarizations $(+,\times)$, as shown in Sec.2.1. However, in scalar-tensor theories of gravity, such as the Brans-Dicke theory, Gravitational Waves have six physical polarizations. These additional polarizations could cause motion of test masses longitudinal to the direction of propagation, conversely to the transverse nature of the Plus and Cross polarization effect, as well as different oscillation patterns in the transverse plane respect to the relativistic ones. High Signal-to-Noise Ratio events that are going to be provided by Einstein Telescope will be able to shed light on the presence of additional polarizations in Gravitational Wave signals, eventually confirming or ruling out a whole class of alternative theories to General Relativity.

Bounding graviton mass In Einstein's theory gravitons, the quanta of the gravitational field, are massless particles. As a consequence, gravitational information and radiation travel at the speed of light. Massive graviton theories are natural extensions to General Relativity. In such theories Gravitational Waves would not travel at the speed of light and this could be tested throgh multimessenger observation of distant gravitational wave sources, by measuring the difference in the arrival times of gravitational and electro-magnetic radiation. The major source of uncertainty in such an estimate of the graviton mass relies in the complex nature of gravitational collapse in supernovae and coalescing binaries which makes it difficult to accurately compute the initial retard of EM emission respect to the GW signal.
There is indeed another method for the determination of the graviton mass that is capable of yelding more robust results. This alternative method exploits the fact that in massive graviton theories Gravitational Waves would suffer disperson. More specifically, the graviton speed of propagation v_g will depend on its wavelength λ as $v_g \approx \left(1 - (\lambda/\lambda_g)^2\right)$, where λ_g is the Compton wavelength of the graviton[4], so that the higher frequency band of the Gravitational Wave will arrive earlier than the lower frequency part of the signal. The resulting distortion of the signal respect to the relativistic prediction is proportional to the distance of the GW source respect to the observer. Then, the ability to detect BBH mergers at the edges of the universe may prove critical for estimates of the graviton mass and consequently for confirming or ruling out massive graviton extensions to General Relativity.
The first Gravitational Waves observations were already sufficient to put a constraint on the graviton mass of $m_g \leq 1.2 \times 10^{-22}\,\mathrm{eV}$ [37]. This upper bound on the graviton mass will be considerably improved when multimessenger observations and detection of BBH mergers at cosmological distances will become a routine operation.

Measuring the dark energy equation of state and its variation with z Starting from the late '90s, evidence has emerged suggesting that the expansion of the Universe is accelerating. This evidence can be explained by considering modifications of General Relativity at large length scales or by introducing a new contributor to the mass/energy content of the Universe, the Dark Energy[5]. The time evolution of an homogeneous and isotropic universe is described by the combination of the Friedmann Equations and an additional Equation of State for the Dark Energy fluid that drives the accelerated expansion of the cosmic spacetime. The Equation of State links the pressure and density of the Dark Energy fluid and takes the general form:

$$p_{DE} = \omega(z)\rho_{DE}. \tag{4.2}$$

The traditional model for Dark Energy is the one of an exotic negative pressure fluid ($\omega = -1$). At present, the most accurate constraints on the Dark Energy Equation of State parameter ω are determined combining the Planck Mission data on Cosmic Microwave Background with galactic redshift catalogues built upon Type Ia Supernovae observations and Baryon Acoustic Oscillations measurements [38]: the obtained 1σ bound $\omega = -1.03 \pm 0.03$ is compatible with the standard model for the Dark Energy fluid.
The main source of uncertainty in the above constraint comes from the fact that galactic redshift determination currently rely on the Cosmic Distance Ladder (see Sec.4.3.3). This problem can be bypassed with the employment of routine multimessenger observation data, obtaining more reliable measurements of compact binary inspirals redshifts as a function of their luminosity distance and thus more accurate constraints on ΛCDM parameters such as ω.

[4]The result is valid at first order approximation in $x = (\lambda/\lambda_g)^2$.

[5]The most general form of Einstein's Field Equation 2.1 can be expressed as:

$$R_{\mu\nu} - \frac{1}{2}g_{\mu\nu}R + \Lambda g_{\mu\nu} = \frac{8\pi G}{c^4}T_{\mu\nu}$$

where Λ is the 'Cosmological Constant' coefficient. The Cosmological Constant has the same effect as an intrinsic energy density of the vacuum, to which is associated a vacuum pressure governed by the vacuum fluid Equation of State.

Testing Black Hole Theorems The physicality of Black Holes has been widely demonstrated thanks to a large number of experimental evidences that emerged in the last fifty years. Despite the evidence for their existence, most of the features of this extremely compact objects and of the nature of space-time that surrounds them remains unknown.
Due to the Uniqueness theorem, which states that the Kerr metric is the unique end state of gravitational collapse, it is generally accepted that rotating Black Holes are described by the Kerr Metric of General Relativity (see Sec.6.6 of [14] for more details). However, the theorem is based on several assumptions, namely that the system is stationary and axisymmetric, that there is a spacetime horizon and that there are no closed timelike curves. If one of these assumptions were violated, then objects that deviate from the Kerr metric could exist.
These assumptions on the nature of spacetime surrounding a Black Hole can be tested by monitoring the dynamics of an object that transit in proximity to a BH horizon. This could be enabled by Einstein Telescope with the detection of Intermediate-Mass-Ratio Inspirals (IMRIs), that are inspirals of a $m \sim 1M_{\odot}$ object into a $M \sim 100M_{\odot}$ Black Hole, thanks to its enhanced sensitivity in the $[1, 10]$ Hz frequency band. In such an asymmetric system, many Gravitational Wave cycles are emitted while the smaller object is in the strong field region close to the larger object, allowing to obtain information on the spacetime structure surrounding the more massive BH. Einstein Telescope is expected to detect IMRIs up to redshifts of $\sim 1 - 5$, depending on the mass and spin of the larger Black Hole [39], translating in an expected detection rate of tens or hundres IMRIs events per year [40].
Einstein Telescope could also allow to test the No-Hair theorem by looking at quasi-normal modes, the superposition of damped sinusoids that constitutes the Gravitational Wave signal of an asymmetric Black Hole evolving towards the spherical shape. Informations on quasi-normal modes are buried in the last instants of a Gravitational Wave signal, when the merger of two compact objects has happened and the resulting Black Hole rapidly radiates away the residual potential energy stored in its asymmetric mass distribution, in what is known as the ringdown phase. As a consequence of the No-Hair, which states that a Black Hole can be completely characterized by just three externally observable variables (mass, electric charge, angular momentum), the frequencies and time-constants of the quasi-normal modes depend only on same three observables. The No-Hair theorem could be tested by comparing the mass and spin parameters of the final Black Hole obtained from quasi-normal modes fitting with the same parameters inferred from the inspiral and merger dynamics, searching for eventual departurtures.

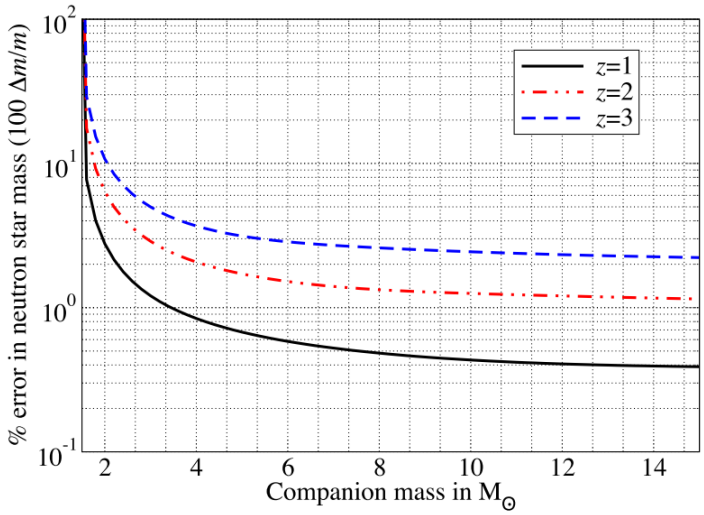

Figure 4.5: ET Accuracy of the NS mass determination in a NSBH merger as a function of the BH mass and for different redshifts. The Neutron Star mass is assumed to be $M_{NS} = 1.4M_{\odot}$.

Limits on the maximum mass of a compact star There exist several theoretical upper limits on the mass of a compact system before it encounters instability due to the fact that the gravitational pressure overcomes the degeneracy pressusure of stellar fluid. The most known examples are the Chandrasekar limit for White Dwarfs ($M_{Chand} \approx 1.4 M_{\odot}$) that are sustained by electron degeneracy pressure and the Tolman–Oppenheimer–Volkoff limit for Neutron Stars ($M_{TOV} \approx 2.2 - 2.9 M_{\odot}$) that are sustained by neutron degeneracy pressure. This limits this limits are also dependent on the stellar fluid Equation of State, the conditions of which cannot be reproduced and studied with current experimental techniques. The direct observation of BNS or NSBH mergers by the Einstein Telescope could provide a valuable insight on the properties of compact astrophysical objects.
Fig.4.4 shows the maximum distance to which compact binary inspirals are expected to be seen in Einstein Telescope for systems with two equal mass companions[6]. In particular Eintein Telescope is expected to observe NSBH merger events up to several units of redshift, translating in a $10^5 - 10^6\,\mathrm{yr}^{-1}$ detection rate. In addition, the diagram in Fig.4.5 shows the accuracy with which the mass of a Neutron Star can be determined in an NSBH inspiral as a function of the companion mass and redshift, for an instrument with the sensitivity of Einstein Telescope. As the large majority if the confirmed mergers events in the advanced detectors host Black Holes with masses $M \geq 4 M_{\odot}$, it is expected that ET could determine Neutron Star masses with few percent accuracy up to $z = 3$ redshift.

4.3.2 Astrophysics

Einstein Telescope will be a unique observatory to study Neutron Stars and Black Holes dynamics, compositions and distribution as it will be sensitive to a large variety of relativistic phenomena in addition to the many compact binary mergers that are already revealed by the second generation detectors. Examples include quakes in Neutron Stars, Supernovae, Proto-Neutron Stars formation and Gamma-Ray Burst sources. In the following section it is presented what the Einstein Telescope can unveil about this compact objects and their enviroments.

Neutron Star Physics The detection of Gravitational Waves from BNS mergers will provide a wide variety of physical information on the progenitor stars. It is particularly important to gain an insight on the Equation of State of bulk stellar matter in the extreme pressure and temperature conditions that are reached in the core of Neutron Stars and even more during the BNS merger phase. The behaviour of nuclear matter in this enviroments is currently not well understood and measurements of Gravitational Wave signals from NS sources can usefully constrain its Equation of State.
The Neutron Star Equation of State leaves its signature not only in BNS and BHNS merger signals but also in the peak frequencies of supernova waveforms, in the magnitude and damping time of NS crust mountains or in NS glitches and other oscillation mode excitations. Fig.4.6 illustrates the differences in the Power Spectral Density of a BNS merger signal in the case the two components have a cold (blue solid) or hot (red dashed) Equations of State, comparing them to sensitivities of different generation detectors. Despite the fact that this are the two extremal cases for the EoS of neutral matter, it is clear that the observation of several high-SNR BNS signals with the Einstein Telescope could provide decisive evidence to discriminate between different models.
Einstein Telescope data could also be crucial to shed light on the Neutron Star glitches enigma. Glitches are events in which a Neutron Star is seen to suddenly spin-up, followed by a relaxation period towards stable secular spin-down. Hundreds of single glitches have been observed in the radio emission of pulsar and magnetars, while some Neutron Stars, like the Vela pulsar, exhibit regular large glitches with a fractional frequency change amplitude of the order of $O(10^{-6})$. The mechanisms that

[6]For a binary system with symmetric mass ratio $\eta = \frac{m_1 m_2}{(m_1+m_2)^2}$, the maximum expected observable distance would be smaller by a factor $\sqrt{4\eta}$.

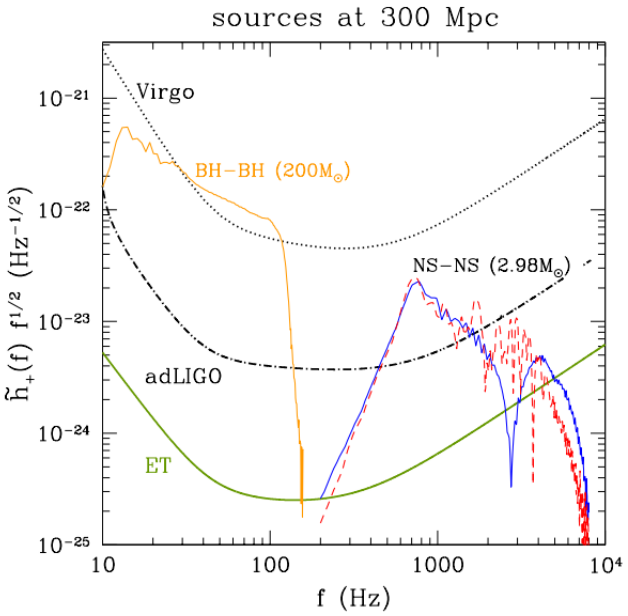

Figure 4.6: Gravitational wave spectra of BNS mergers compared to sensitivities of Virgo, aLIGO and ET, in the case the two components have a cold (blue solid) or hot (red dashed) Equations of State. Also shown for comparison is the corresponding spectrum of an equal-mass, non-spinning BBH (orange solid). Simulations from [41].

originate this phenomena remains a mistery to this day[7]. Einstein Telescope could provide an insight on the phenomena if Neutron Star sourced signals are detected in coincidence with an EM glitch, or it could set upper limits on the asymmetry of the process in alternative.
Rotating Neutron Stars may also suffer several instabilities that are associated with unstable modes of oscillations. Of special intrest are GW driven instabilities such as f-modes which deform the star into a bar-shape and r-modes which radiate predominantly through the current multipoles. Upon better understanding of the Neutron Star interior and consequent modelization, waveforms associated with glitches and instabilities can be obtained, enabling direct observation of the phenomena in the $[10 - 100]$ Hz frequency band of the Einstein Telescope.

Gamma-Ray Burst progenitors Gamma-Ray Bursts are the most energetic electromagnetic events that have been observed in the universe. They are classified either as short-hard or long-soft bursts depending on their duration and spectra. Long GRBs are associated with supernovae in late-type star-forming host galaxies while short GRBs are observed at lower redshifts inside a variety of galaxy types including early-type elliptical and lenticular galaxies without active star forming regions, so that it is thought that the progenitors of the latter type of events are BNS and BHNS mergers. A longer-lived optical afterglow is usually emitted at longer wavelengths, which allows to locate the host galaxy of the event.
Then the detection of BNS and BHNS mergers by the Einstein Telescope, in coincidence with electromagnetical GRB events, could give a clearer picture of the mechanisms at the core of short Gamma-Ray Bursts. Predicting the Gravitational Wave emission of core-collapse supernovae associated with long GRBs is instead more difficult and involves modelling the complicated internal dynamics of the collapsing star. In the absence of proper modeling of long GRB sourced Gravitational Wave signals,

[7]The favoured hypotesis is that glitches are associated to transfer of angular momentum between superfluid components of the star and/or the star crust and charged core [42]. Still the hydrodinamics and instabilities of this quantum superfluid system remain unmodelled.

a less effective unmodelled source can be performed.
A significant fraction ($\sim 15\%$) of short GRBs may instead be associated with flaring activity in Soft Gamma-Repeaters. As the name suggests, these sources periodically emits long GRBs signals with luminosities of $L \sim 10^{41}\,\mathrm{erg\,s^{-1}}$ and photon energies in the range $[10-30]$ keV, accompanied by sporadic short GRBs with luminosities that can reach $L \sim 10^{47}\,\mathrm{erg\,s^{-1}}$. It is hypotized that SGRs are associated with sudden violent reconfigurations of complex magnetic field topologies inside magnetars, or alternatively to impacts of neutron stars with fossil disks around them.
Observations of quasi-periodic shear mode oscillations in Gravitational Wave signals in the $[10-40]$ Hz frequency band, without an accompanying inspiral signal, could provide decisive evidence for the SGR model. Current models for SGRs indicate that they will emit less than 10^{46} erg in Gravitational Waves [43]. Fig.4.7 shows the 90%-confidence level limits on the distances to which the ET detector will be sensitive to GW bursts with such energy. It can be noted as Einstein Telescope could enable the detection of extra-galactic SGR events.

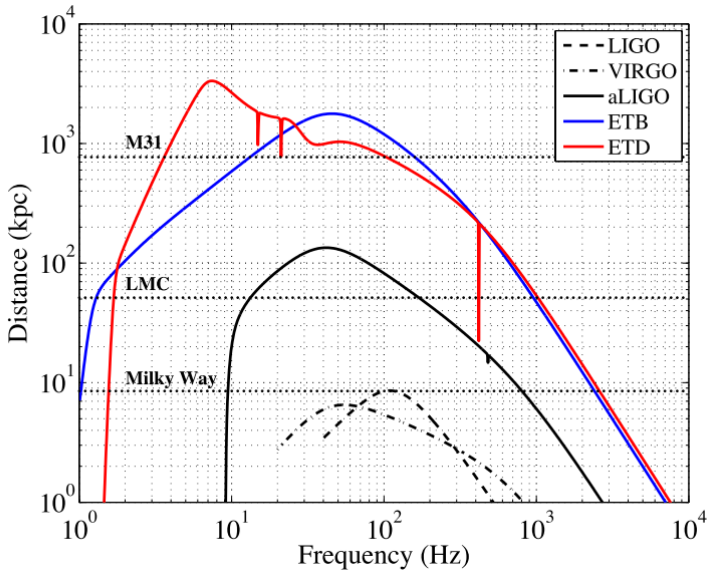

Figure 4.7: 90%-confidence lower limit on the observation range of various detectors for SGR sources with 10^{46} erg enegry radiated as GWs. The solid horizontal black lines show the distances to various galactic locations (centre of Milky Way, Large Magellanic Cloud, M31 galaxy).

4.3.3 Cosmology and Cosmography

As stated in the introduction to Sec.4.3, Einstein Telescope could observe coalescence GW signals up to the edge of the Universe. By properly identifying the host galaxy of such events one can obtain reconstruct the evolution of the distributions of variuos GW emitting phenomena throughout the history of the universe. Einstein Telescope interferometers will also be sensitive to stochastic background radiation from primordial processes, thus providing an useful tool to investigate unanswered cosmological questions.

Compact Binary Coalescences as Standard Sirens Estimates of astronomical distances are a non trivial task and rely on the elaborate Cosmic Distance Ladder system, which correlates short-range methods, like parallax, with middle- and long-range methods that rely on various types of standard candles. There are several issues affecting these techniques, the most relevant of which regard standard

candles, astronomical objects with known absolute magnitude: the theoretical debate on the 'standardness', that is the level of constancy of the absolute magnitude between different objects of the same type, is open for many candle candidates and beside this calibration and correct identification issues, especially in the case of object and galaxies at cosmological redshifts, add a significant contribution to the overall uncertainty of the estimate.
Accurate measurements of Gravitational Wave signals coming binary system inspirals could provide an independent method for estimating astronomical distances that does not suffer the main issues affecting the Cosmic Distance Ladder. Chirping signals from the coalescence of compact stars are then named Standard Sirens, as their amplitude depends only on a number of source parameters that can be directly inferred by looking at the waveform signature and on the luminosity distance. It is necessary to have system of at least three independent interferometers to fully disentangle the angular dependency of the Gravitational Wave signal, allowing for a correct sky location of the event and leaving the luminosity distance as the only free parameter left in the system.
The only contributions to the uncertainty of this kind of distance estimate come from detector calibration issues and SNR of the detected signal, plus systematic errors due to weak gravitational lensing. Moreover, there is no way to infer the redshift of the source from a Gravitational Wave signal.Then an accurate sky location of the signal is needed to identify the host galaxy of the event, the redshift of which can be extracted from electromagnetical observations.
Not only Standard Sirens would offer a powerful tool for cosmography, but they would also provide an independent technique to estimate the Hubble Constant H_0. This is because, at small redshifts ($z << 1$), the Hubble Law $D_L = c\,z/H_0$ that links the luminosity distance to the redshift of a specific source is valid, offering a new method to infer the Hubble constant by combining GW and EM observations of mergers event in our cosmic neighborhood. Other cosmological parameters, such as Ω_Λ, Ω_M and ω could be estimated starting from large catalogues of distant objects multimessenger observations, like GRBs progenitors discussed in Sec.4.3.2.

Cosmological evolution of compact object populations and coalescence rates Coalescence rate of compact objects is expected to be dependent on redshift. There are various features that contribute to the overall shape of the dependency and each one of them can be investigated with unprecedented depth with the Einstein Telescope. For instance the compact objects coalescence rate evolution throughout the history of the universe is affected by the following factors: the star formation rate history SFR(z), the binary fraction $f_b(z)$, the formation efficiency of a given type of binary and their distribution of merger times. Einstein Telescope will be able to distinguish between coalescence rate predictions from different SFR models hence providing evidence for history of star formation, expecially at high redshifts where electromagnetical investigation becomes problematic.

Intermediate Mass Black Holes and Supermassive Blach Hole Seeds The Virgo and LIGO Scientific Collaboration have recently announced the first detection of a BBH merger that resulted in the formation of an Intermediate Mass Black Hole [44]. IMBHs are Black Holes with masses in the $[10^2 - 10^5]\,M_\odot$ range, that is significantly more than the few solar masses black holes directly formed in the star life-ending explonsion and at the same time many orders of magnitude less than the Supermassive Black Holes at the center of the galaxies ($[10^2 - 10^5]\,M_\odot$). The GW190521 event observed in the aLIGO and AdV detectors is the first direct evidence for the existence of IMBHs. Still the mechanisms that lead to the formation of IMBHs remain debated. An in depth understanding of IMBHs abundancy and distribution throughout the history of the universe is also crucial to understand the mechanisms that lead to the formation of SMBHs.
Einstein Telescope will be the most efficient tool to investigate the nature of Intermediate Mass Black Holes. In particular, exploiting the cooperation of the Einstein Telescope with the LISA space-based detector, an IMBH binary system coalescence event could be fully reconstructed from the inspiral phase, which Gravitational Wave emission is peaked in the sub-Hz band, to the final merger in-

stants, which signal will instead enter the low-frequency detection band of the Einstein Telescope ($[1 - 10]$ Hz), as can be seen in fig.4.8.

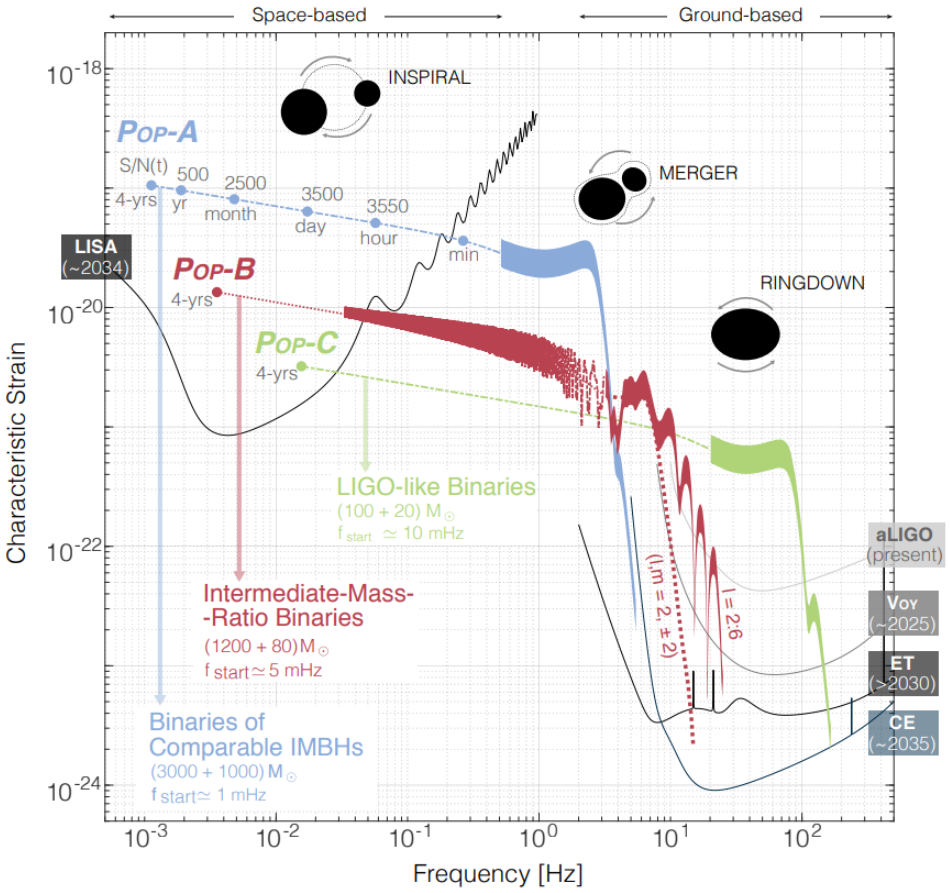

Figure 4.8: Power spectra of the inspiral, merger and ringdown signal from different types of binary IMBH at redshift $z = 0.5$, compared to the design sensitivity of the main space- and ground-based third generation detectors [45].

Primordial gravitational waves Electromagnetical observations can directly probe the universe only up to to Recombination, as before this moment the primordial universe was populated by an hot ionized H-He plasma that was opaque to light. Gravitational radiation does not suffer screenings of any type so that it can freely propagate to us from the very first cosmic instants, potentially carrying direct informations on the early phases of the Big Bang up to the GUT scale of 10^{16} GeV. Various inflation models predict an almost scale-invariant Gravitational Wave spectrum, the amplitude of which is directly correlated to the scalar perturbation of the Cosmic Microwave Background via the Tensor-to-Scalar Ratio coefficient r. Combining the observed amplitude of the CMB electromagnetic spectrum and the more recent constraint on various inflation parameters that determine the final primordial GW spectrum [46], it is possible that a primordial GW background signal could overcome Einstein Telescope sensibility in the $f \leq 10$ Hz frequency band.
There are also other phenomena happening the very early universe that contributes to the generation of a primordial Gravitational Wave background, such as Cosmic String evolution or phase transition reheating and colliding bubbles. Einstein Telescope could also allow to empirically investigate for the first time all this new physics topics that are currently subject just to theoretical debate.
There is another important Gravitational Wave background that superimposes to the primordial one.

That is a stochastic background originating from a large number of unresolved sources since the beginning of stellar activity. The main contributions to this astrophysical background come from BNS coalescences, core collapse Supernovae, rotating Neutron Stars instabilities and triaxial emission.
The detection of such a stochastic Gravitational Wave background with the Einstein Telescope would provide an unprecedented insight on the initial mass function and star formation history, along to costraining physical properties of compact objects, but it could also constitute a noise source hiding the primordial GW background.

Part II

Chapter 5

The Thermal Noise Issue in a Cryogenic Interferometer

As seen in Ch.4, the Einstein Telescope will achieve a wider band sensitivity respect to second generation Gravitational Wave antennae by employing two interferometers for each one of its three planned detectors, separately optimizing each component of the pair for Low Frequancy or High Frequency detection. Different noise contributions affect the sensitivity of an interferometer across its frequency domain, so that different issues must be addressed to maximize the sensitivity in the two LF and HF interferometers.
The aim of this thesis work is to contribute to the research that is being carried out to improve the Low Frequency interferometer sensitivity in third generation Gravitational Wave detectors. The main noise contributions in the sub-10^1 Hz band comes from Seismic Noise, Thermal Noise and Newtonian Noise. While the latter is a fundamental noise that requires post-processing correlation of the interferometric signal with informations coming from arrays of independent detectors, the first two contributions are technical noises that can be lowered by means of better performing substrate materials, anti-reflection coatings and suspension systems for the test masses. In particular, the two contributions are necessarily interconnected: if one desire to lower the thermal noise contribution by employing suspension fibers with a larger section to better conduct heat away from the test mass to the outer enviroment, then this would imply a greater coupling of the test mass with the enviromental vibrations; the same is valid if one is intrested in lowering the Seismic Noise contibution implementing a more advanced suspension system that results in a larger thermal isolation of the test mass, thus increasing its working point temperature and its overall Thermal Noise. Innovative solutions are required to minimize one of the two technical noise contributions without increasing the other one.
The Einstein Telescope design requires that, in order to tackle the Thermal Noise problem the Low Frequency detector will be operated at cryogenic temperatures. Considering the technological challenge related to cooling large volumes and masses to cryogenic temperatures, avoiding to inject back in the system mechanical noise due to cryocolers vibrations, the operating temperature designed for the LF detector is $10\,\mathrm{K}$. This feature will drastically reduce Brownian Thermal Noise and Thermo-Elastic Noise in the test masses bulk and coating, as manifestly shown in Eq.3.44 and Eq.3.48 where it was derived that the two contributions are respectively proportional to $S_x^{1/2} \propto T$ and $S_T^{1/2} E \propto T^2$. On the other hand this would have no direct effect on the Seismic Noise contribution.
The downside of operating an interferometer at cryogenic temperatures is instead indirect. In a low temperature detector the last suspension stage is crucial in the determination of the total Thermal Noise not only for its mechanical losses but also because it needs to extract the thermal load that is put into the optical component by the laser beam. In second generation interferometers that are operated at room temperature, mechanical losses in the last suspension stage are minimized by melting together the test mass and the suspension fiber in a monolithic fused silica part. Unfortunately fused silica, being an amorphous material, has a very small termal conductivity at low temperatures, so that it is

unsuited to serve as suspension substrate in a cryogenic interferometer. It is also important to consider the temperature dependence of the Q factor of the canditate materials for a cryogenic operated detector. If the Q factor of a substrate or cating material lowers considerably for decreasing temperature, operating in a cryogenic environment will not result in thermal noise minimization, due to the larger heat flow contribution that is associated to mechanical losses in the mirror.

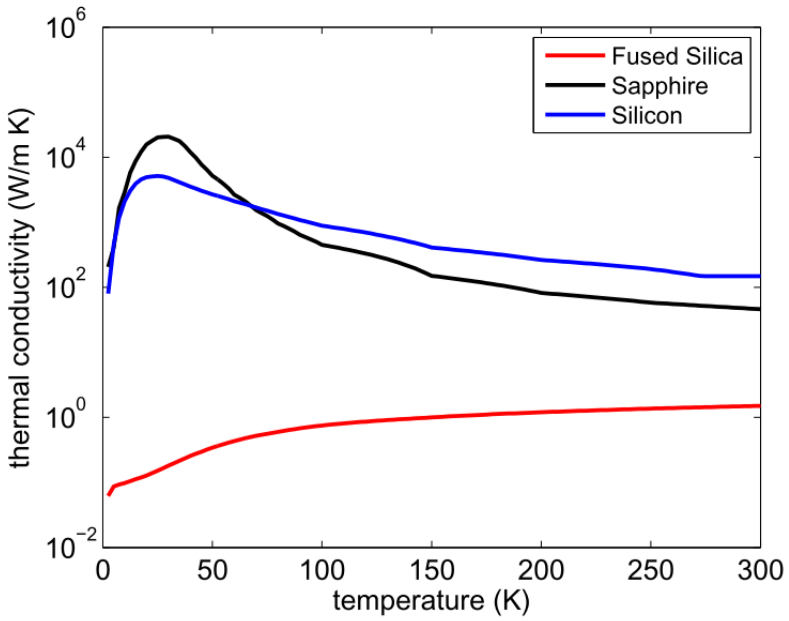

Figure 5.1: Thermal conductivities of various ET-LF detector test mass substrate candidates ([47], [48]).

On the contrary, crystalline materials have a very high thermal conductivity at low temperatures which makes them ideal substrate candidate for cryogenic detector suspension fibers. A comparison between the thermal conductivities of crystalline (Silicon, Sapphire) and amorphous (Fused Silica) materials can be seen in fig.5.1. A qualitative explanation for the low temperature thermal conductivity increase of crystalline materials can be given as follows. At high temperature the finite value of thermal conductivity is due to scattering of phonons amongst themselves via Umklapp processes. U-scattering cross section decreases exponentially with decreasing temperature. Then phonon mean free path increases and as a consequence thermal conductivity rises at low temperatures, reaching a maximum at around $0.05\theta_D$, where θ_D is the Debye temperature of the crystal. At lower temperatures the thermal conductivity falls as T^3, mirroring the temperature dependence of specific heat, due to the fact that the phonon mean free path becomes comparable to the crystal dimensions.
Crystalline materials thermal conductivity depends not only on the sample geometry and dimensions but also on the density of impurities and imperfections. Impurities and imperfections acts as scattering centers for the phonons, decreasing thermal conductivity. Their effect is most important where thermal conductivity peaks, as phonon-phonon U-processes and boundary scattering are relatively weaker in this temperature region (see Fig.5.2). Also the presence of different isotopes spoils the symmetry of the cristalline structure, affecting the final thermal conductivity of the sample.
There are also other parameters that must be considered in the choice for a ET-LF test masses and suspensions substrate besides thermal conductivity. Thermo-Elastic Noise is proportional to the square of the thermal expansion coefficient of the material $S_{TE}^{1/2} \propto \alpha^2$ (Eq.3.48) while mechanical losses of the substrate increase Brownian Thermal Noise in the suspensions. Another factor that plays a key role in the substrate material choice is the availability of large enough samples of the material to serve as interferometric mirror and recoil mass. Silicon is then the favored canditate for ET-LF test masses sub-

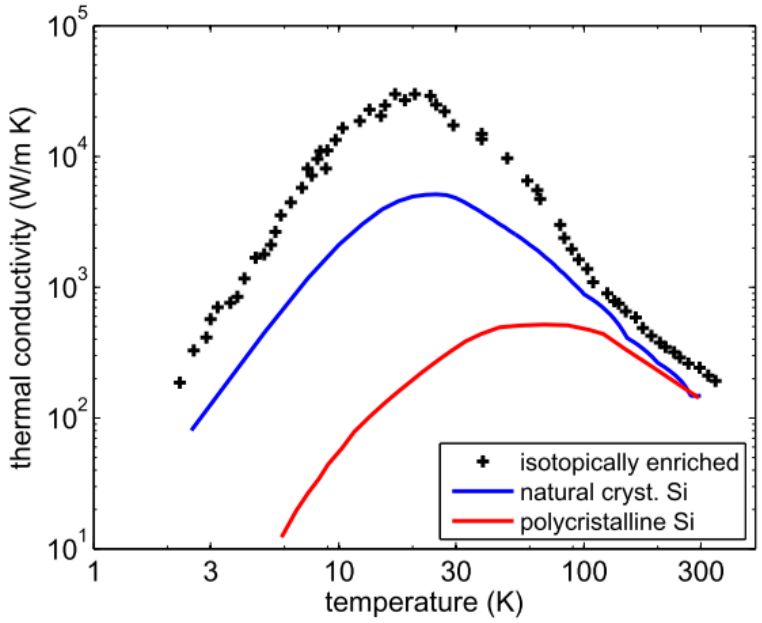

Figure 5.2: Thermal conductivity of polycrystalline Silicon compared to monocrystalline Silicon with different isotope fractions (Natural: $(92.2\%\ ^{28}\mathrm{Si},\ 4.7\%\ ^{29}\mathrm{Si},\ 3.1\%\ ^{30}\mathrm{Si})$; Enriched:$(100\%^{28}\mathrm{Si})$). Data from [47], [49].

strate as Sapphire is currently not available in large enough samples. Then Silicon should be preferred also as suspension substrate candidate, due to the fact that silicon-silicon bonds based on hydroxid-catalysis-bonding are stronger than sapphire-silicon bonds; a different thermal expansion coefficient between the two materials would cause further stress in the connection and bonding imperfections would contribute to increase the overall mechanical losses of the system.

Aside from the general motivations for substrate material choice in a cryogenic detector that were carried out in previous paragraph, additional care must be taken to assure that Silicon, the favoured candidate so far, could satisfy all the specific requirements of the Einstein Telescope Low Frequency interferometer.
The main design parameters for the High and Low Frequency interferometers of the Einstein Telescope are summarized in Tab.5.1. The reasons for the differences between the two interferometer have been explained in previous chapters. It should be noted that the shift to Silicon as mirror substrate material would require a shift also in the laser wavelength to $\lambda = 1550\,\mathrm{nm}$, due to the fact that crystalline Silicon is not transparent to $\lambda = 1064\,\mathrm{nm}$ light currently used in second generation interferometers. As a consequence, Erbium-Fiber lasers will replace Nd:Yag lasers in the Low Frequency interferometers.
Of particular intrest for Thermal Noise computations are the circulating power inside the LF-interferometer arms and its mirror size. That is because in a real optical element, the Reflectance and Trasmittance do not sum up to unity due to a net optical absorption in the substrate that is proportional to the incident light power[1]. The larger the total absorbed optical power inside the mirror, the higher the stress that is put on the suspension fibers which are designed to extract the excess heat from the test mass system. This is a crucial issue in third generation cryogenic detectors, as Suspension Thermal Noise is expected to be one of the dominant noise contributions in the sub-10^1 Hz frequency region (Fig.4.3). Moreover the total heat capacity of the test mass system, that is proportional to the mirror mass, will determine the operating temperature of the mirror at a given absorption level, directly contributing to the total mirror thermal noise.

[1] Or to the incident light power raised to an arbitrary power in the more general case of non-linear absorption.

Parameter	ET-HF	ET-LF
Arm Length	10 km	10 km
Input Power (after IMC)	500 W	3 W
Arm Power	3 MW	18 kW
Temperature	290 K	10 K
Mirror Material	Fused Silica	Silicon
Mirror Mass	200 kg	211 kg
Mirror Diameter / Thickness	62 cm/30 cm	min 45 cm/T
Laser Wavelength	1064 nm	1550 nm
Beam Shape	TEM_{00}	TEM_{00}
Beam Waist	12 cm	9 cm
Scatter Loss per Surface	37.5 ppm	37.5 ppm
Filter Cavities	1×500 m	2×1000 m
Quantum Noise Suppression	10 dB FDS	10 dB FDS
Seismic Isolation	SA, 8 m tall	mod SA, 17 m tall

Table 5.1: Main design parameters for ET-HF and ET-LF interferometers (SA= SuperAttenuator, FDS=Frequency Dependent Squeezing). The parameters refer to the most recent ET-D design ([50]).

It is then of primary importance to obtain not only a characterization but also a deep understanding of the optical absorption process in candidate materials for the Einstein Telescope Low Frequency interferometer test masses at cryogenic temperatures. Still a detailed analysis of optical absorption in crystalline Silicon at cryogenic temperatures is lacking to this day.
Two different research groups investigated Silicon optical absorption at $\lambda = 1550\,\mathrm{nm}$ in the last decade obtaining somehow conflicting results, the first based at Leibniz University and Max Planck Institute in Hannover ([51], [52], [53]) and the second being a collaboration between scientists of the Laboratoire des Matériaux Avancés in Lyon and the Friedrich Schiller University in Jena ([54], [55]). While the first analysis pointed out that bulk absorption in crystalline Silicon substrates could reach values as low as $\alpha \leq 5\,\mathrm{ppm/cm}$ [54], subsequent studies agreed on a different attenuation coefficient of $\alpha \approx 300\,\mathrm{ppm/cm}$, oppositely attributing the optical absorption to bulk [55] and surface [52] effects. It must be also noted that only [55] measurements are performed at cryogenic temperatures. This last result should be then given more importance, as the fragmentary evidences make it impossible to formulate a comprehensive theory that is capable to extend the room temperature values to cryogenic enviroments.
This thesis work then aims at clarifying the experimental evidences on crystalline Silicon optical absorption at $\lambda = 1550\,\mathrm{nm}$ thanks to an independent direct measurement of the absorption coefficient, enabling the formulation of a coherent theoretical framework that is capable to explain Silicon optical absorption processes at various temperature scale and providing deciding elements for the substrate material choice in a third generation Gravitational Wave interferometer test masses.

Chapter 6

Experimental Set Up Design and Characterization

A cryogenic detetector such as Einstein Telescope Low Frequency interferometer requires very low overall absorptions in its optical elements. Test masses substrate candidates must ideally posses an absorption coefficient of few $\mathrm{ppm/cm}$. Measuring such a low levels of optical absorption is a non trivial operation: accuracies of commercially available powermeters reach at best few percentage points so that a direct measurment of a ppm power absorption in the sample is made impossible. Moreover there exist no ready-to-use facilities or instrumentation that can provide a high accuracy optical absorption measurment in a cryogenic enviroment.
In the following chapter, we're going to present an innovative technique for measuring crystalline Silicon optical absorbtion at $\lambda = 1550\,\mathrm{nm}$ and cryogenic temperatures, the Modulation Calorimetry technique (Sec.6.1). The development of this technique was initially favoured by various constraints in the available experimental equipment (Sec.6.2) that made impossible to replicate the Silicon absorption measurement methods found in literature. It eventually resulted in a solid and accurate optical absorption measurement technique that could find broader applications in power absorption measurements.

6.1 Measurement Technique

The invention of Modulation Calorimetry dates back to more than one hundred years ago when Orso Mario Corbino, an italian physicist and politician, managed to use oscillations in the electrical resistance of a wire to measure the temperature oscillation of the filament material. The technique was originally intended to infer the specific heat capacity of a substance from the oscillations of the heating power and temperature of a sample but it can be reversed to perform a power absorption measurement upon an indepentement acquisition of the specific heat capacity of the material.
The theory of this measurement technique is simple. The fundamental equation of Modulation Calorimetry is the heat balance equation for a system in which the input power is modulated by a sine wave $p_0 + p\sin(\omega_p t)$, evaluated on an arbitrary small time interval Δt:

$$\big(p_0 + p\sin(\omega_p t)\big)\Delta t = mc_p\Delta T + Q(T)\Delta t \tag{6.1}$$

where m, c_p and T are the mass, specific heat and temperature of the sample, $Q(T)$ are the heat power losses of the sample system. Performing a linear expansion of the quantities T and $Q(T)$:

$$T = T_0 + \frac{dT}{dt}\Delta t + O((\Delta t)^2) \approx T_0 + \Theta \qquad \text{for} \qquad \Theta << T_0 \tag{6.2}$$

$$Q(T) = Q(T_0) + \frac{dQ}{dT}\frac{dT}{dt}\Delta t + O((\Delta t)^2) \approx Q(T_0) + Q'\Theta \qquad \text{for} \qquad Q'\Theta << Q(T_0) \tag{6.3}$$

the fundamental equation of Modulation Calorimetry can be rewritten as:

$$p_0 + p\sin(\omega_p t) = mc_p\Theta' + Q(T_0) + Q'\Theta \tag{6.4}$$

where $\Theta' = dT/dt$ is the first derivative of the sample temperature. Upon defining as ϕ the phase shift between the oscillations of the dissipated power and the temperature oscillations induced in the sample, the steady-state solution ($Q(T_0) = p_0$) to the above differential equation can be given as [56]:

$$\Theta = \Theta_0\sin(\omega_p t - \phi) \tag{6.5}$$

where:

$$\Theta_0 = \frac{p}{\sqrt{m^2c_p^2\omega_p^2 + Q'^2}}, \tag{6.6a}$$

$$\tan(\phi) = \frac{mc_p\omega_p}{Q'}. \tag{6.6b}$$

The behaviour of the amplitude and phase retardation of temperature oscillations in the sample can be seen in Fig.6.1. The solution of Eq.6.4 can be analyzed in analogy to the one of an RC circuit fed by a voltage containing both DC and AC components. In this case, when the condition $\tan(\phi) >> 1$ is fulfilled, the corrections for heat dissipations in the system related to the oscillating AC voltage component become negligible and the Adiabatic Regime is reached.

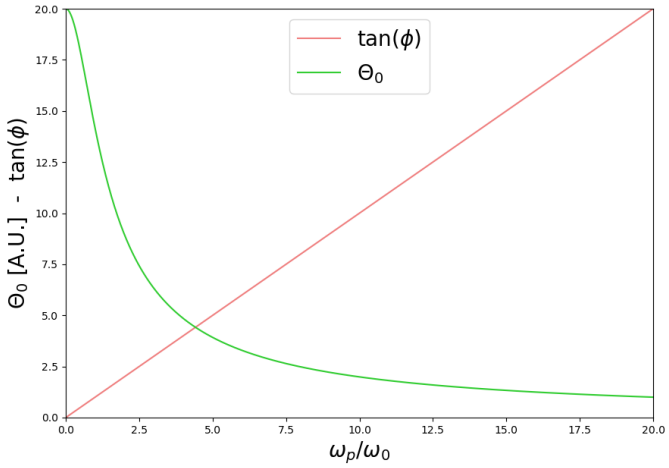

Figure 6.1: Distribution of the Θ_0, $\tan(\phi)$ parameters in the solution of the Modulation Calorimetry equation as a function of the input power modulation frequency ω_p. The critical frequency ω_0 is defined such as $\tan(\phi)(\omega_0) = 1$.

An analogous Adiabatic Regime can be defined in our laser-sample system for $\tan(\phi) > 10$. When the Adiabatic Regime condition is fulfilled, the heat loss oscillations caused by temperature oscillations in the sample are much smaller than the input power oscillations. That is, the condition $Q' << mc_p\omega_p$ is fulfilled and Eq.6.6a can be rewritten as:

$$p_{abs} = mc_p\omega_p\Theta_0. \tag{6.7}$$

Eq.6.7 is the basic equation of Modulation Calorimetry and it was explicitely put in a form that underlines the fact that in our experiment it is p_{abs}, the amplitude of absorbed power oscillations, to be the unknown parameter. This method will then allow to directly estimate the total absorbed optical power inside the crystalline Silicon sample, that must be compared with the total beam power that is entering

the Si sample at the input surface to compute Silicon optical absorption coefficient.
In order to extract from this quantity the optical attenuation coefficient of crystalline Silicon the absortion process should be modelled as linear, that is independent from the optical intensity in the sample. In [52] it has been shown that non-linear effects in Silicon at $\lambda = 1550\,\mathrm{nm}$ start becoming relevant for intensities larger than $I = 10^3\,\mathrm{W/cm^2}$. An indepent test will be performed to verify the linearity condition in our experimental set up in a cryogenic enviroment.
Then, due to the Poissonian nature of linear photon absorption in a medium, the optical intensity has an exponential scaling respect to the distance x travelled by the beam inside the sample substrate:

$$I(x) = I_{in} e^{\frac{x}{\lambda_{Si}}} = I_{in} e^{\alpha_{Si}\, x} \tag{6.8}$$

where α_{Si} and λ_{Si} are the optical attenuation coefficient and characteristic length of crystalline Silicon respectively. An analogous relation can be obtained for the transmitted power p_{out} upon integration of the optical intensity, so that the total absorbed power immediately obtained as:

$$p_{abs} = p_{in} - p_{out} = p_{in}\big(1 - e^{\alpha_{Si}\, x_{Si}}\big). \tag{6.9}$$

Then, upon a precise determination of the beam optical path inside the sample x_{Si}, the above equation can be reversed to obtain an estimate of the Silicon attenuation coefficient:

$$\alpha_{Si} = \frac{1}{x_{Si}} \ln\left(1 - \frac{p_{abs}}{p_{in}}\right). \tag{6.10}$$

A final substitution of Eq.6.7 in the above equation provides the complete expression that will be used to extract the Silicon optical attenuation coefficient from a temperature oscillation measurement:

$$\alpha_{Si} = \frac{1}{x_{Si}} \ln\left(1 - \frac{m c_p \omega_p \Theta_0}{p_{in}}\right). \tag{6.11}$$

Then it is evident the advantage of the Modulation Calorimetry technique compared to alternative measurement methods, such as the Impulsive method that was performed in [55], where a fixed power beam is suddendly shined through a Silicon sample that is thermally decoupled from the outer enviroment so that excess heat that is injected through absorption could not be dissipated and the sample temperature is expected to exhibit an exponential rise towards the new equilibrium temperature of the system. The exponential approach to equilibrium temperature is acquired, fitted and compared to a reference signal that was previously obtained by resistively heating the sample with known input power. The Modulation Calorimetry technique does not require calibration, as it only requires to independently determine the $c_p(T)$ relationship for the material under analysis, something which is extensively documented in literature for Silicon throughout all the temperature region of intrest for the experiment. Conversely, it was not possible install a resistive heater on our Silicon sample so that in order to obtain a reference signal for an Impulsive measurement in our set up we would need to shine a different wavelenght laser beam through the sample, assuming that the absorption coefficient for optical absorption in cryogenic environment at the new wavelenght has been independently determined in literature.
As a consequence, the Modulation Calorimetry technique not only could be performed with a relatively easy and less expensive set-up, but it would also provide a self-contained method for the determination of Silicon optical absorption coefficient. The uncalibrated impulsive technique will instead prove to be useful for testing and debugging purposes during construction phase of the experimental facility.

6.2 Experimental Set-Up

The primary aim of this work is to obtain a direct estimate of the crystalline Silicon optical absorption coefficient at cryogenic temperatures and for $\lambda = 1550\,\mathrm{nm}$ light. In order to achieve this goal it is

required to place a crystalline Silicon sample in a cryogenic enviroment, allowing for a $1550\,\mathrm{nm}$ laser beam to pass through the test material while recording temperature changes of the sample. All the technical specifications of the analyzed Silicon sample are summarized in Tab.6.1.

Manufacturer	Siltronix
Material	Crystalline Silicon
Growth Technique	Float-Zone
Doping Type	Intrinsic
Orientation[1]	(1 0 0)
Polished Surfaces	2
Resistivity	$> 500\,\Omega/\mathrm{cm}$
x-axis Dimension (cm)	1.990 ± 0.005
y-axis Dimension (cm)	1.005 ± 0.005
z-axis Dimension (cm)	1.020 ± 0.005
Mass (g)	4.71 ± 0.01

Table 6.1: Parallelepipedal silicon sample technical specifications.

In this section experimental set up and instrumentation that was needed to perform the final absorption measurement is examined in detail. All the technical specifications of the cryogenic system will be given in Sec.6.2.1 in addition to an in-depth account of calibration and characterization of cryogenic equipement (Sec.6.2.2, Sec.6.2.3). Sec.6.2.4 will present in detail the design process of the support system inside the cryogenic chamber, exploring the various thermodinamical and spatial constraints that had to be met in order to accomodate the sample above the cryocooler cold head. Design and characterization of the optical line are described in Sec.6.2.5. The presentation of the experimental set up will end with a brief outline of the Labview program that allowed for digital power modulation and signal acquisition. In the end, Sec.6.2.7 will be devoted to present a preliminary analysis that was made to evaluate the sensitivity of the Modulation Calorimetry technique within the constraints imposed by the experimental system designed throughout the chapter.

6.2.1 System Overview

All the cryogenic instrumentation that is described in this section was inherited from previous experiments conducted at the Laboratori Nazionali di Legnaro by the AURIGA and Prof. G. Carugno groups. The cryocooling apparatus we disposed of was a CTI-Cryogenics 8300 Compressor that employed a helium based thermodynamic cycle to perform heat extraction on a $d = 5cm$ cylindrical cold head. The cold head was housed inside a CTI-Cryogenics vacuum chamber equipped with two CF-sealed 1550nm-coated optical windows and various access ports to allocate vacuum feedthroughs for thermometrical instrumentation electrical connections (see Fig.6.2). All the system was operated in high vacuum. In order to reach high-vacuum pressure inside the $0.1\,\mathrm{m}^3$ CTI-Cryogenics chamber we employed a Varian Turbo-V 81-M turbo-molecular pump, in series with a pre-vacuum dry pump. We also installed a system of vacuum gauges that was able to monitor the chamber pressure and to alert when the system pressure reached sub-$10^3\,\mathrm{mbar}$ values.
In Fig.6.2 it can be also found a scheme of the system that was designed to house the Silicon crystal inside the cryogenic chamber. All the payload is enclosed inside the radiative shield, which is actively cooled. The supports and sample are mounted above the cold head. The copper support temperature is stabilized to a constant value by the PID controlled resistive heater.

[1] Normal to the main surface

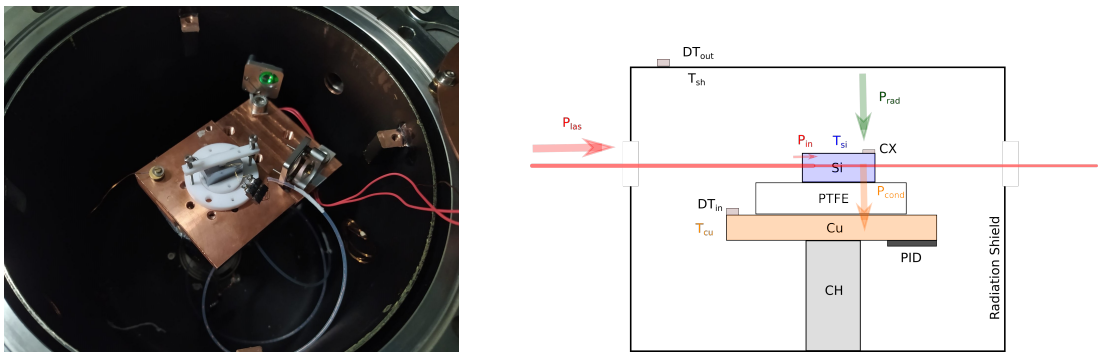

Figure 6.2: Left: Final set up of the cryogenic chamber interior; Right: Scheme of cryogenic chamber thermodynamics. Heat flow contributions: radiation heat flow (P_{Rad}); conduction heat flow (P_{Cond}); optical power of the laser beam at the input surface (P_{Las}); optical absorption heat flow (P_{In}). Thermometers: in-loop DT-470 (DT_{In}) measuring copper support temperature (T_{Cu}); out-of-loop DT-470 (DT_{Out}) measuring radiadiation shield temperature (T_{Sh}); CX-1050-SD (CX) measuting silicon sample temperature (T_{Si}). Chamber parts and materials: cold head (CH); PID resistive heater (PID); copper (Cu); teflon ($PTFE$); crystalline silicon (Si).

To fully monitor the temperature variation of the various system parts, three thermometers are employed: the in-loop LakeShore DT-470 thermometer is mounted on the copper to extract an error signal for the PID control; the out-of-loop LakeShore DT-470 thermometer is coupled to the radiation shield; the LakeShore CX-1050 thermometer is mechanically clamped on the sample upper surface to monitor temperature variations of the Silicon crystal. All the thermometers are wired with a 4-wire connection to the read-out instrumentation in order to bypass potential voltage drops that are happening in the wiring and assure to acquire an unbiased voltage signal.
DT-470 are diode thermometers so that they must be operated with a fixed excitation current to produce a temperature dependent voltage signal. They have a compact design allowing for easy clamping with a single M2 screw and they guarantee a fast response time which make them ideal to extract the error signal for the PID temperature stabilization system. A standard calibration curve for DT-470 thermometers which has $< 0.1K$ accuracy across all the operating temperature range is provided by the manufacturer. We disposed of two different Lakeshore thermometer reading instruments which were programmable to convert the DT-470 voltage signal in a temperature measurement and which provided the proper excitation current for the thermometers; the Model 820 was employed to read the out-of-loop thermometer signal; the DR91C was used to acquire the in-loop thermometer signal and had a built-in anlog PID control system that allowed to stabilize the copper support temperature to the desired setpoint by sending a controlled current to the resistive heater.
LakeShore CX-1050-SD thermometer is instead an uncalibrated resistive thermometer and its resistance signal is acquired by an HP 3458A $6 - 1/2$ digit multimeter through a 4 wire connection. CX-1050-SD is much more compact than DT-470 thermometers, so that it can be directly installed on the sample. Its purpose is the direct measurement of the sample temperature increase upon absorption due to the laser beam and is therefore the most important sensor of the apparatus. To thermally couple the thermometer to the sample we opted for a mechanical clamping provided by a spring aided teflon cap. This method resulted to be the most stable and consistent during various calibration attempts.

[2] At $T = 77\,\mathrm{K}$.
[3] At reccomended excitation and $T = 4.2\,\mathrm{K}$.

	DT-470	CX-1050-SD
Type	Diode	Resistive
Size	$\varnothing 7.95 \times 4.343\,\mathrm{mm}$	$3.175 \times 1.905 \times 1.080\,\mathrm{mm}$
Operating Range	$[1.4 - 500]\,\mathrm{K}$	$[0.1 - 325]\,\mathrm{K}$
Response Time[2]	$0.1\,\mathrm{s}$	$0.25\,\mathrm{s}$
Dissipation[3]	$17\mu\,\mathrm{W}$	$0.1\mu\,\mathrm{W}$

Table 6.2: LakeShore thermometers technical specifications.

6.2.2 CX-1050-SD Thermometer Calibration

Due to very limited available space inside the cryogenic chamber and in particular to the small dimensions of the Silicon sample upper surface, several attempts were required to find the optimal technique to perform thermal coupling of the CX-1050-SD thermometer with the crystal. Calibration of a resistive thermometer requires to obtain an unique and monotonical $T(R)$ function, taking advantage of a yet calibrated thermometer, specifically the in-loop DT-470 thermometer. To quantify the goodness of a thermal coupling method, reproducibility of the $T(R)$ function obtained during different calibration attempts with the same coupling method were compared between different coupling techniques. Left side of Fig.6.3 shows one of the failed calibration attempts, where the CX-1050-SD thermometer was glued to the crystal surface with electrically and thermally conductive silver glue. Reproducibility issues of this thermal coupling method are evident: after each cooling/heating cycle the acquired CX-1050-SD resistance was lowered at equal temperature. The problems were probably caused by stress happening on the contact surface due to different thermal expansion coefficients of Silicon, Silver glue and CX-1050-SD materials, as the cooling obtained curve is well superimposed to the previous heating curve, while after the system reached cryogenic temperatures the subsequent heating acquired curve visibly differed from the previous $R(T)$ function. This silver glue coupling method is compared to the spring aided teflon cap mechanical clamping (right side of Fig.6.3). The superior reproducibility of the second method is evident as the $R(T)$ curves acquired during subsequent cooling/heating cycles appear to be perfectly superimposed.

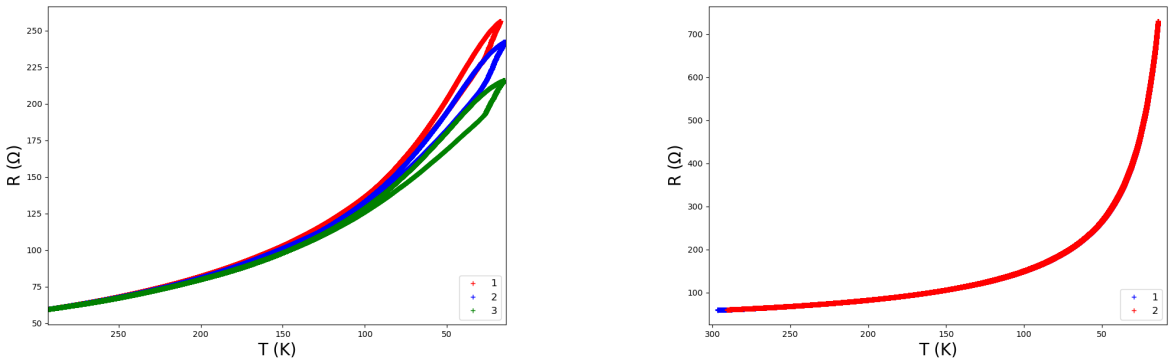

Figure 6.3: $R(T)$ curves acquired during subsequent cooling/heating cycles.
Left: Silver glue method; Right: Spring aided teflon cap method.

Thermal coupling method reproducibility can be examined in greater detail by computing the difference between $R(T)$ curves acquired during different calibration attempts. The difference will be performed across all the operating temperature range. The difference is separately computed between cooling and heating phases of the acquisition due to reasons that will be later analyzed. In order to

obtain a meaningful information on calibration non-reproducibility errors, the CX-1050-SD resistance signal is converted in a temperature signal with the use of a temporary calibration based on $dR/dT(T)$ normalization of the resistance data. Fig.6.4 illustrates the CX-1050-SD temperature difference between the same phase (cooling or heating) of different acquisitions performed with the mechanical clamping configuration, as a function of the DT-470 reference temperature.

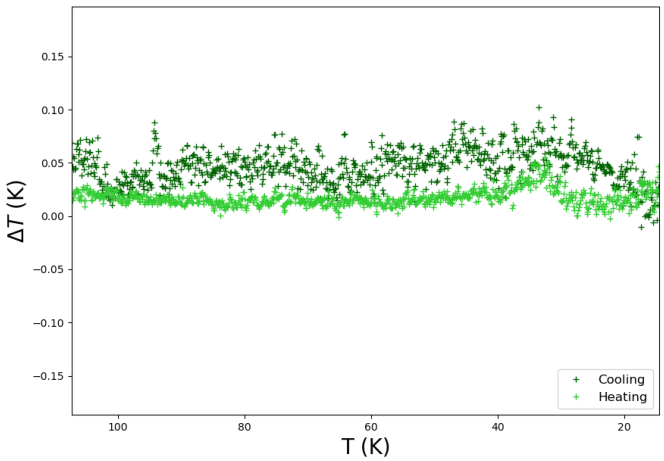

Figure 6.4: CX-1050-SD temperature difference between same phase (dark green:cooling; light green: heating) of different calibration acquisitions with the mechanical clamping configuration as a function of the DT-470 reference temperature. Close view of the analysis in the temperature region of intrest for the final absorption measurement ($T < 100\,\mathrm{K}$).

It can be seen as the temperature difference measured by the CX-1050-SD thermometer between the same phase of different acquisiton in a cryogenic environment is constantly below $\Delta T < 0.1\,\mathrm{K}$. As a consequence the spring aided teflon cap mechanical clamping can be considered a consistent thermal coupling method for the Cernox thermometer-Silicon crystal system.
Aside from the reproducibility issue it is also important to quantify the isteresis phenomenon that is present in the CX-1050-SD signal between different phases (cooling ad heating) of the same acquisition. To this purpose it is useful to compute the CX-1050 temperature difference between cooling and heating phases of the same calibration acquisition with the same procedure of previous paragraph. The result of the analysis is shown in the dark blue line of Fig.6.5.
The calibration acquisitions exhibit an isteresis behaviour over the course of a cooling/heating cycle, as the sensed CX-1050-SD temperature during cooling phase is larger than the heating phase acquired temperature across all the operating temperature range, with differences that grow over $1\,\mathrm{K}$ even at cryogenic temperatures. This isteresis-like behaviour is probably caused by the fact that this initial calibration was performed with a 'drifting' method, that is CX-1050-SD and DT-470 temperatures were acquired while the system temperature was decreasing/increasing without waiting for the system to reach equilibrium; if the two thermometers have different response time to temperature changes, with such discrepancy evolving with temperature, it is expected that they will respond differently to cooling and heating temperature drifts, which happen at considerably different rates.
The difference of the time derivative of the CX-1050-SD temperature evolution between cooling and heating phase of the same acquisition was computed and plotted against the DT-470 reference temperature (light blue curve of Fig.6.5). It can be seen that the behaviour of the two quentities in Fig.6.5 is qualitatively similar across the whole temperature range of the calibration acquisitions, providing evidence in support of the explanatory hypothesis fo the observed isteresis phenomenon that was pre-

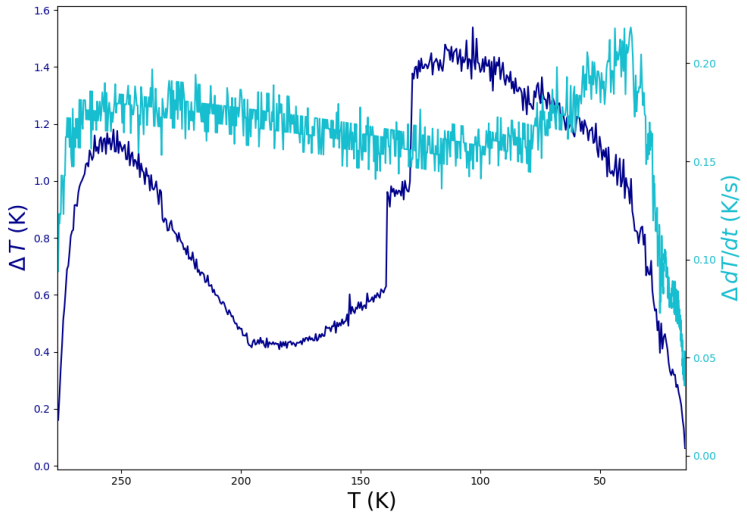

Figure 6.5: Dark blue: difference of the CX-1050-SD temperature between cooling and heating phase of the same acquisition. Light blue: difference of the time derivative of CX-1050-SD temperature evolution between cooling and heating phase of the same acquisition.

sented in this paragraph.[4]

The above issue can be significantly mitigated by switching to a 'static' calibration. That is, the CX-1050-SD and DT-470 temperature acquisitions should be performed in equilibrium conditions after having stabilized the copper support temperature by means of the PID controlled resistive heater. This calibration technique was performed in the $T < 25\,\mathrm{K}$ temperature range, as when the maximum output current that the DR91C controller is able to erogate to the resistive heater is used the copper support stabilizes to such temperature. In a static calibration acquisition each $(T_{DT} \pm \sigma_T, R_{CX} \pm \sigma_R)$ data point is computed in the following way: both in-loop and out-of-loop DT-470 thermometers are installed on the copper support along to the CX-1050-SD thermometer amd the copper temperature is stabilized at a given value with the use of the PID heater; after equilibrium has been achieved a $100\,\mathrm{s}$ long acquisition of both out-of-loop DT-470 temperature and CX-1050-SD resistance signals is performed[5]; each acquisition data is averaged to obtain the (T_{DT}, R_{CX}) data point, to which the standard deviation of the acquisition is associated as uncertainty on each axis. Three different dataset were acquired, the first (a) by progressively increasing the temperature stabilization set points from $20\,\mathrm{K}$ to $25\,\mathrm{K}$, the second (b) by decreasing the temperature stabilization set points from $25\,\mathrm{K}$ to $15\,\mathrm{K}$ and the third (c) by increasing the temperature stabilization set points from $15\,\mathrm{K}$ to $20\,\mathrm{K}$. The three dataset were analyzed by fitting the obtained results with a phoenomenological function. As a simple expression able to fit the observed datapoints, it was chosen an hyperbolic model, which was fitted to the data by performing an orthogonal distance regression method, in order to take into account both the incertitudes on R and T:

$$T(R) = a + \frac{b}{R - c} \tag{6.12}$$

The three different calibration datasets are shown in the left side of Fig.6.6 along with the respective fits. The fitting curves shows good agreement across all the $[15 - 25]\,\mathrm{K}$ range.
The same isteresis analisis of previous paragraph, where CX-1050-SD temperature differences are

[4]The major exception to the curves similarity are the two discontinuities in the $\Delta T(T)$ data in the $[120 - 130]\,\mathrm{K}$ region. The nature of this discontinuity was not investigated. If the discrete ΔT variations are ignored and removed, the qualitative match between the two curves is clear.

[5]The system is considered in equilibrium if the relative value of the temperature drift registered by DT-470 thermometer do not exceed 1% throughout the whole acquisition.

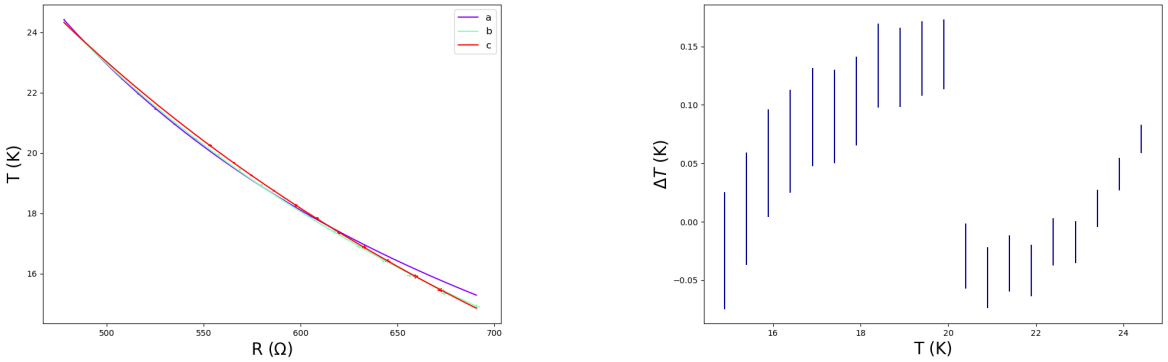

Figure 6.6: Left: comparison of different static calibration acquisitions. Right: difference of the CX-1050-SD temperature between cooling and heating acquisitions ($T < 20\,\mathrm{K}$: b-a; $T > 20\,\mathrm{K}$: b-c).

computed between cooling and heating phase, is perfomed in the right plot of Fig.6.6. Here the two set of acquisition in which the data points were acquired in a heating trend (a,c) are compared with the calibration data set that was acquired while progressively cooling the system from $25\,\mathrm{K}$ to $15\,\mathrm{K}$. The acquisitions are compared only in their shared temperature range of acquisition. The CX-1050-SD temperature difference between different acquisition is reduced of an order of magnitude respect to cooling versus heating phase differences in drifting calibration acquisitions, so that static calibration should be regarded as the preferable calibration method in the temperature range of intrest for the final absorption measurement. In the following sections all the CX-1050-SD acquisitions will be implicitely calibrated with the $T(R)$ curve of the 'b' static calibration acquisition, as the second dataset is the one with the largest number of data points. A dedicated plot of the 'b' acqusition calibration fit is shown in Fig.6.7 along with the residual plot of the data points respect to the fitting curve.

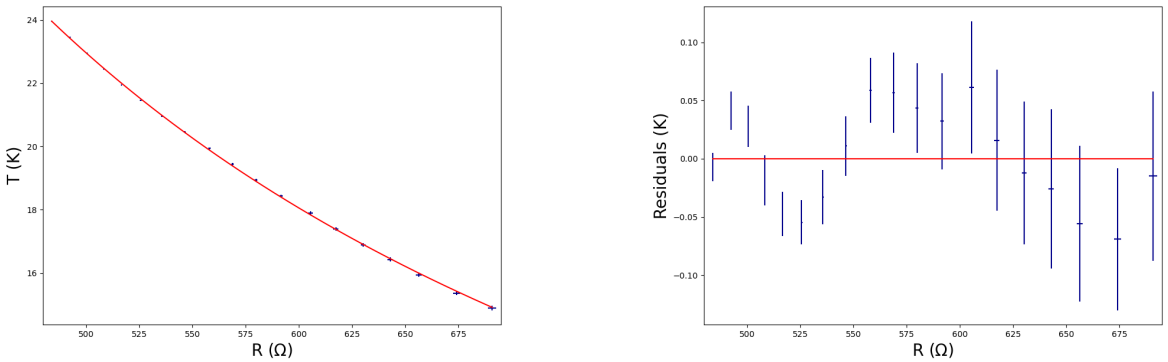

Figure 6.7: Static calibration b dataset superimposed to the fitting curve (left) and related residual plot (right).

a (K)	b (K Ω)	c (Ω)
$-4.4 \pm 1.0 \times 10^{0}$	$1.25 \pm 0.1 \times 10^{4}$	$4.27 \pm 2.0 \times 10^{1}$

Table 6.3: Parameters for the Eq.6.12 model fit to the b dataset of static calibration acquisitions.

The fact that all the data points are within 3σ uncertainty from the fitting line ensure the validity of the empirical model across all the temperature region of intrest for the experiment.
With the aim of monitoring the crystal temperature during cooling phase in order to detect in real-time possible issues on the sample mounting or on CX-1050-SD clamping, it was also performed a fit to the full-range cooling phase of the drifting calibration data with an empirical model of the following type:

$$T(R) = a + \frac{b}{R - c} + d\,R. \tag{6.13}$$

The result of the calibration fit along with the related residual plot and summary of the fit parameters is shown in Fig.6.8 and Tab.6.4. It is worth underlining that this secondary full-range calibration serves the only purpose of real time monitoring of the sample-thermometer system during cool down phase, so that model simplicity should be favoured over accuracy.

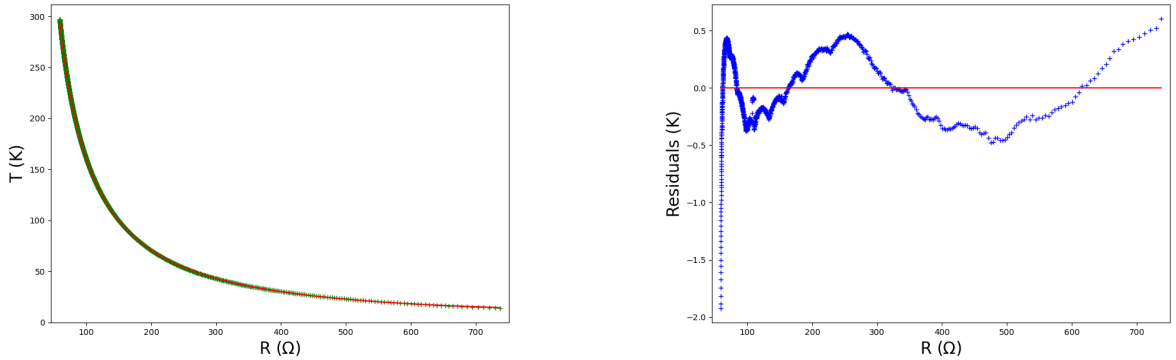

Figure 6.8: Full-range cooling phase calibration curve data along with empirical model fitting curve (left) and related residual plot (right).

a (K)	b (K Ω)	c (Ω)	d (K/Ω)
$-1.62 \pm 0.01 \times 10^{1}$	$1.64 \pm 0.02 \times 10^{3}$	$6.06 \pm 0.04 \times 10^{0}$	$1.12 \pm 0.02 \times 10^{-2}$

Table 6.4: Full-range cooling phase fit parameters ($T(R) = a + b/(R - c) + dR$).

6.2.3 PID Temperature Stabilization System

The LakeShore DR91C, which is employed for in-loop DT-470 signal acquisition and calibration, is equipped with a built-in analog Proportional Integrative Derivative electronic circuit that controls a $[0 - 1]$ A current generator feeding a 50Ω resistive heater. By gluing the resistive heater to the copper support that is contacting the cold head, the copper temperature could be stabilized to a desired temperature setpoint by controlling the Joule heating dissipated power on the resistor with the PID system. Various test acquisition have been performed to debug and characterize the PID temperature control system. The test acquisitons has been carried out by gluing the resistive heater to a prototype support that was cooled down to limit temperature. At first it was performed a simple test to characterize the stability of the temperature control as a function of the set point temperature. The system was stabilized at different set point temperatures in the $[14 - 20]$ K range; for each temperature setpoint, PID

parameter optimization was performed; after the system temperature fluctuations has been minimized, a $120\,\mathrm{s}$ acquisition of the copper clamped out-of-loop DT-470 thermometer was started. To quantify the stability of the temperature locking it was computed the standard deviation of the acquired dataset. The following plot illustrates the RMS error of the PID control system as a function of the temperature setpoint:

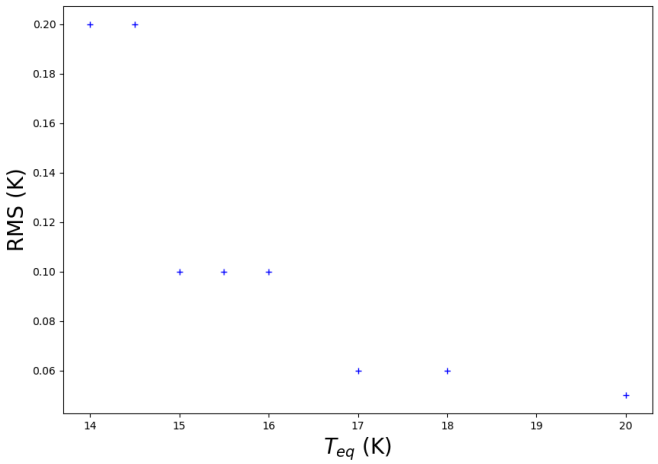

Figure 6.9: Out-of-loop DT-470 temperature RMS error versus PID setpoint temperature.

To increase the stability of the PID temperature locking system it is essential to understand which are the main noise sources that contribute to the RMS of temperature fluctuations as a function of the temperature setpoint and of the PID parameters.
To this purpose two types of acquisition were collected. In the first case several dataset were obtained by setting different temperature setpoints and adjusting the PID parameters to be the optimal ones for each set temperature. In the second case the temperature setpoint was kept fixed and the PID parameters were slightly detuned from their optimal value.
Each dataset was analized by performing a FFT on time intervals of 120 s.

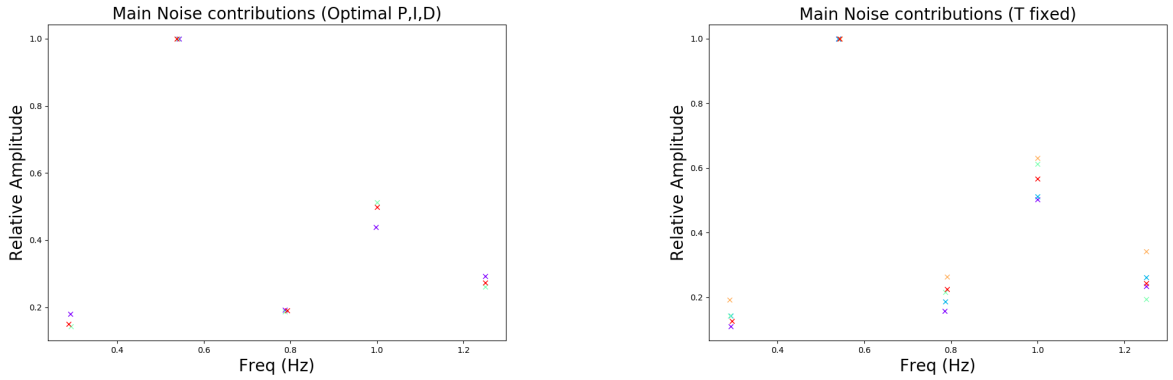

Figure 6.10: Main Noise Contributions in different setpoint temperature changing (left) and PID parameters changing (right) acquisitions. Noise peaks belonging to the same acquisitions are marked with the same colour.

The main noise contributions are independent of the temperature setpoint and the PID parameters. The dominant contribution in the noise spectrum of all the acquisition is a $0.54\,\mathrm{Hz}$ peak, which is followed from a higher frequency contribution at $1\,\mathrm{Hz}$. In order to investigate if the noise contribution pattern was an artifact of the digital acquisition, that was performed via a Labview program performing

temperature measurements at a fixed sampling rate throughout all the previous acquisitions, a third dataset was obtained in which the temperature setpoint and PID parameters were kept fixed while varying the sampling frequency of the temperature measurements. The sampling rate was varied in the $[1.4 - 6.7]$ Hz range. The result of the analysis is shown in the following plot, where noise peaks belonging to slower sampling rate acquisitions are marked with red-shading colours and noise peaks belonging to faster sampling rate acquisitions are marked with blue-shading colours:

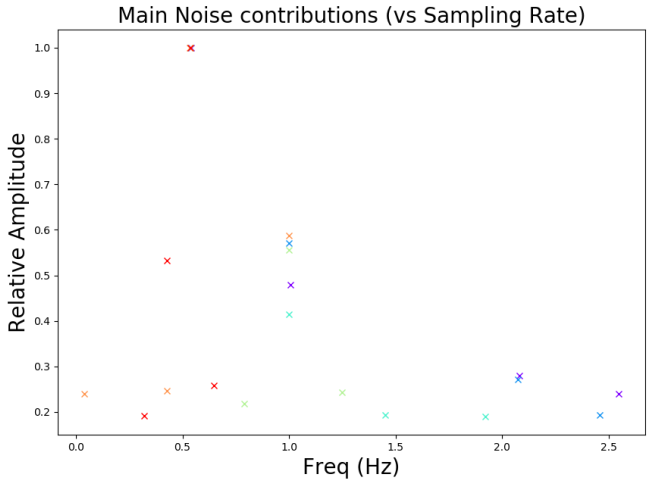

Figure 6.11: Main Noise Contributions in different sampling rate changing acquisitions. Faster sampling rate data points are marked with red-shading colours, while slower sampling rate data points are blue-shaded.

The fact that the red points are distributed in the lower frequency range while the blue in the higher frequency range is a manifestation of Nyquist theorem: an acquisition that is performed with sampling rate f_s is only able to inspect frequencies up to $f_{Ny} = f_s/2$, while higher frequencies are aliased back into the $[0, f_{Ny}]$ range. The aliasing phenomenon is clearly visible in the $0.4\,\mathrm{Hz}$ peak of the $f_s = 1.429\,\mathrm{Hz}$ acquisition (red), as this data point represent the usual $1\,\mathrm{Hz}$ contribution aliased back in the Nyquist frequency range ($f_s/2 - (1\,\mathrm{Hz} - f_s/2) \approx 0.4\,\mathrm{Hz}$). This means that the $0.54\,\mathrm{Hz}$ and $1\,\mathrm{Hz}$ noise peaks are present also in all the sampling rate varying acquisitions and they are not an artifact of the Labview program digital sampling rate. Also other peaks that have a precise frequency location in the first two $f_s = 3.33\,\mathrm{Hz}$ acquisitions are identifiable with larger frequency aliased noise contribution, like the $1.2\,\mathrm{Hz}$ peak which is actually caused by the $2\,\mathrm{Hz}$ first harmonic of the $1\,\mathrm{Hz}$ peak ($f_s/2 - (2\,\mathrm{Hz} - f_s/2) \approx 1.2\,\mathrm{Hz}$).
After the prototype copper support was replaced with the definitive model it was possible to turn back investigating the PID control system stability issue with the use of the independently acquired CX-1050-SD thermometer. In fact, by clamping all three thermometers to the copper support and performing an acquisition after the system had reched its limit temperature without turning on the PID heater, when the three independently acquired temperature signals were Fast Fourier Transformed the following result was obtained:
The $0.5\,\mathrm{Hz}$ noise peak along with its higher frequency harmonics is only present in the DT-470 acquisitions, while the CX-1050-SD signal exhibits a $1/f$ noise spectrum, that is the typical pink noise spectrum of electronic devices. This fact points out that the configuration independent noise peaks that were observed in the previous analysis are caused by an internal problem inside the DT-470 readout chain. This internal $0.5\,\mathrm{Hz}$ noise contribution is then translated in a copper support temperature fluctuation, as the in-loop signal that is used to stabilize it is obtained from a DT-470 thermometer. Nevertheless, as the overall copper temperature fluctuations in the temperature region of intrest for the

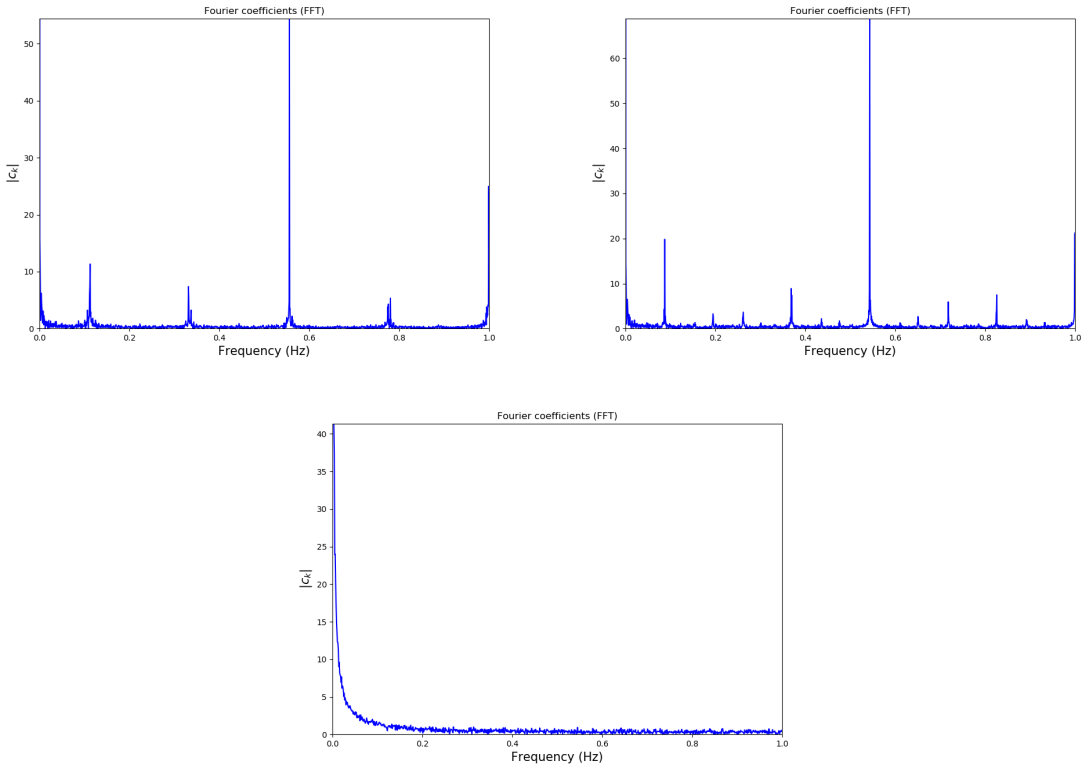

Figure 6.12: Fast Fourier Trnasform coefficient of in-loop DT-470 (up left), out-of-loop DT-470 (up right) and CX-1050-SD (down) signals during a PID temperature stabilization system test acquisition.

final measurement have RMS$< 0.1\,\mathrm{K}$, then we can try to live on with the issue by limiting ourselves to analyze its impact on a Modulation Calorimetry acquisition.

6.2.4 Cryogenic Chamber Design

A fundamental requirement for the creation of a cryogenic environment for the study of Silicon crystal optical absorption is to set up a cryocooling facility that could accomodate the required sample housing and the thermometrical instrumentation, while disposing of a window system to allow for laser beam input and evacuation. The sample housing is specifically designed to thermally decouple the Silicon crystal from the cold head of the cryocooling apparatus, so that the sample temperature is allowed to vary independently from the cold head temperature variations when heated by an external power source. This is achieved by inserting a layer of thermal insulating material between the crystal and the cold head wich sharply reduces the sample conductive heat dissipation; at equilibrium in cryogenic environment the dominant heat flow contributions on the sample becomes heat radiation to the chamber inner surfaces and thermal conduction to copper through teflon. To lower the sample equilibrium temperature as much as possible it is then necessary to encapsule the payload inside at least one radiation shield that prevents the sample to directly see the inner surface of the chamber at room temperature. The cryocooling apparatus should be properly dimensioned accordingly to the payload total thermal capacitance, to chamber heat dissipations and to the desired limit temperature on the sample.
The Silicon sample was placed along the optical axis of the chamber by means of a three stages support. The support system has undergone several prototype phases so that its design could fulfill all the technical requirements needed for correct sample housing and temperature monitoring. An exploded view of the CAD project of the sample support system is shown in Fig.6.13, while detailed dimensioned drawings of all the individual pieces can be found in App.A. The volume and surface of various

pieces have been kept as small as possible to minimize the radiation heat flow to the inner shield surface and the time required for the whole system to be cooled down to cryogenic temperatures.

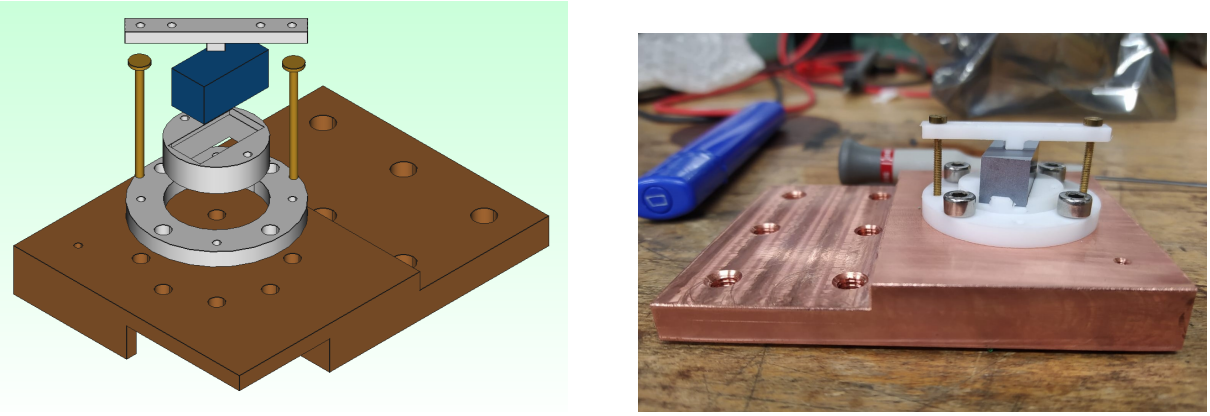

Figure 6.13: Left: Exploded view of sample support system;
Right: Assembling of sample support system.

The lower stage of the sample support is made of copper to ensure optimal thermal coupling with the cold head. The copper support shape is constrained by several logistic requirements. At first it should provide a solid clamping system to the cold head for the payload so that a consistent thermal coupling is established between the two bodies; clamping is provided by means of a circumference of $d = 4\,\mathrm{mm}$ clearence holes on the copper support, that allow for screw fixing to the cold head threaded holes. The copper support should then be equipped with an asymmetrical prolongation to extend below the optical line after the beam has passed through the sample. This extension is provided of six M6 threaded holes to serve as optical plane in the case the beam exiting the sample needs to be steered towards the chamber output window by means of small $1550\,\mathrm{nm}$ HR coated mirrors. The optical plane dimensions and position along the z axis of the chamber had to be carefully designed to allow for New Focus 9871 mirror mounts to be clamped on it with mirrors placed in a centered configuration respect to the beam axis. New Focus 9871j clamping to the optical plane was provided by dedicated mounters that allowed 3-degree-of-freedom positioning of the mirror whithout blocking the fixing holes of the plane. The detailed design of the mirror mount clampers can be found in App.A. The copper support also disposes of a M2 threaded hole to allow for in-loop DT-470 thermometer clamping; the PID controlled resistive heater was glued to the lower surface of the optical plane extension.
The second stage of the support was made by two separate PTFE (teflon) pieces, a thermal insulating material which provides thermal decoupling between the silicon crystal and copper temperature fluctuations. The stage is formed by an inner cylindric body that is concentrical to an outer toroidal piece; this configuration allows tu tune the orientation of the sample respect to the beam axis, so that the system could be positioned at Brewster Angle where beam reflections towards the radiation shield are minimized. The outer teflon support has only a structural function: it allows mechanical clamping of the upper stages of the sample housing to the copper support and cold head via four perpendicular $d = 4\,\mathrm{mm}$ clearence holes; it is also equipped with four M2 threaded holes to allow for clamping of the third stage teflon cap. The inner teflon support instead houses the parallelepipedal crystal inside a dedicated socket. The area of contact between the sample and the support is reduced as much as possible to minimize conductive heat flow through teflon.
The third stage of the support consist of a teflon bar structure (teflon cap) which has the aim of keeping fixed the sample orientation respect to the beam axis during cooling phase. The bar is equipped with four $d = 2\,\mathrm{mm}$ holes for screwing the piece to lower stages of the support. The contact area between the teflon cap and the sample is kept as small as possible to minimize conductive heat flow through teflon cap and screws towards copper. During developement phase the teflon cap also took on a structural function, allowing for CX-1050-SD clamping to the crystal. This was achieved by placing

the thermometer below the teflon cap contact surface and adding two M2 springs between the screw heads and the teflon cap upper surface.

Another crucial constraint on the sample housing system is imposed by the fact that the laser beam must enter in a centered location respect the vertical axis of the chamber windows. This forces the distance between the sample lower surface, which is landed on the inner teflon support socket, and the cold head support surface to take a fixed value ($h = 9\,\mathrm{mm}$). The copper support and the inner teflon piece must be fitted inside this constrained vertical slot, so that an optimization procedure is required to determine the ratio between the width of the two different material. Increasing the width of the teflon layer at the expense of the copper width would favour thermal decoupling between silicon and copper while increasing the minimum equilibrium temperature achievable on the sample; on the contrary decreasing the teflon width would allow to study Silicon optical absorption at lower temperatures but the small temperature fluctuations on the sample predicted by Modulation Calorimetry theory could become undetectable due to the leading contribution of copper temperature fluctuations.
Then the main requirement for performing Modulation Calorimetry measurements is the thermal decoupling of the Silicon crystal from the copper support, which is actively stabilized via PID heater. In the end the teflon support height parameter optimization will be a trade off between thermal decoupling of the sample from the copper support and the need of testing Silicon optical absorption at lowest possible temperatures.
As the Silicon optical absorption measurement was initially meant to be performed with the impulsive technique, the teflon support width optimization has been carried out by discussing results of thermodynamicals simulations modeled upon this type of measurement. After the first support system prototype was built, we learnt about the Modulation Calorimetry technique; we then performed a feasibility study to estimate if a Modulation Calorimetry measurement could be realized without heavily modifying the already existing set up. The initial teflon support width optimization will be illustrated in the following section, while the Modulation Calorimetry feasibility study will be presented in a dedicated section.

Before starting with thermodynamical modelization of the sample response to laser illumination, it should be at first estimated the minimum achievable temperature on the sample as a function of the teflon support width. This estimate is based on the direct measurements of the copper support and Silicon crystal limit equilibrium temperatures that were acquired during the first chamber cooling test with a prototype teflon sample support of $z_P = 5\,\mathrm{mm}$ width placed upon a $z_C = 4\,\mathrm{mm}$ copper layer. When the sample is placed on the teflon support, equilibrium is reached when the conductive heat extraction performed by the cooling apparatus on the sample is balanced out by radiation heat that is flowing from the hotter radiation shield to the colder sample ($P_{cond} = P_{rad}$). Thermal conduction between the crystal and the copper support, which is kept at constant temperature T_{Cu}^{lim} by the PID control system, is proportional to the temperaure difference between the two bodies and inversely proportional to the width of the teflon layer that is separating them:

$$P_{cond} = \frac{k_P(T_P)\,A_c}{z_P}(T_{Si} - T_{Cu}^{lim}) \tag{6.14}$$

where k_P is the teflon thermal conductivity, which is a function of the teflon temperature T_P, $A_c \approx 10^{-5}\,\mathrm{m}^2$ is the contact area between silicon and teflon[6] and T_{Si} is the sample temperature.
Modelling the sample-shield system as two spherical contcentric surfaces, thermal radiation between the two bodies is given by Stefan-Boltzmann law:

$$P_{rad} = A_{eff}\sigma\big((T_{Sh}^{lim})^4 - (T_{Si})^4\big) \tag{6.15}$$

[6] As the contact area between silicon and teflon is much smaller than the contact area between teflon and copper we can approximate the conductive heat flow to happen only in a teflon tube of area equal to A_c.

where σ is the Stefan-Boltzmann constant, T_{Sh}^{lim} is the limit temperature of the copper radiation shield and $A_{eff} \approx 5 \times 10^{-3}\,\mathrm{m}^2$ is the effective area for radiative heat transfer, which correspond to the smaller body area in the concentric cylinders model. At first the information on the sample limit temperature above the prototype teflon support ($T_{Si}^{pro} \approx 70\,\mathrm{K}$) should be used to estimate the radiation shield limit temperature by isolating T_{Sh}^{lim} in the equilibrium equation:

$$T_{Sh}^{lim} = \left(T_{Si}^4 + \frac{k_P(T_P)\, A_c}{A_{eff}\sigma z_P}(T_{Si} - T_{Cu}^{lim}) \right)^{1/4}. \tag{6.16}$$

Teflon temperature can be approximated as the average temperature between copper and silicon ($T_P = (T_{Si}+T_{Cu}^{lim})/2$) and teflon thermal conductivity as a function of the teflon temperature can be estimated by fitting [57] data with a linear model in the temperature region of intrest. Substituting the sample and copper support limit temperatures measured during preliminary test ($T_{Si} \approx 70\,\mathrm{K}$, $T_{Cu}^{lim} \approx 13\,\mathrm{K}$), the estimate of the copper radiation shield temperature comes out as $T_{Sh}^{lim} \approx 100\,\mathrm{K}$.
Then we can proceed to estimate the Silicon sample equilibrium temperature as a function of the teflon support width by approximating the copper support and shield temperatures as fixed. As it is not possible to analitically solve the equilibrium equation in T_{Si}, the sample equilibrium temperature was numerically computed with the bisection method for non-linear equations. The results of the analysis is shown in Fig.6.14.

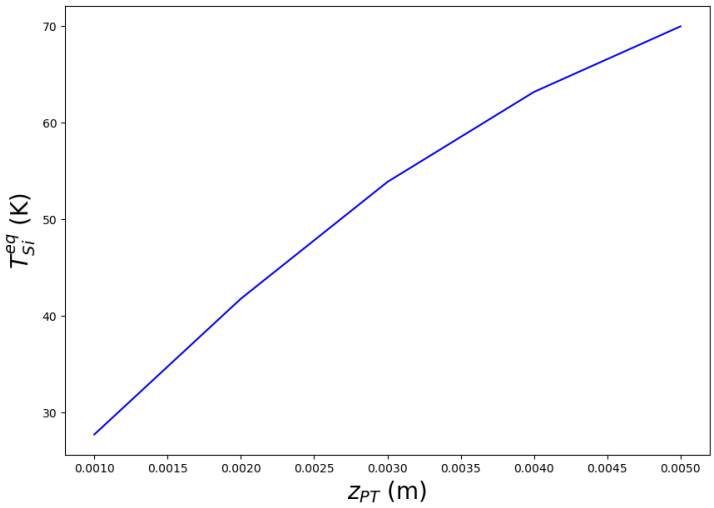

Figure 6.14: Estimate of Silicon sample equilibrium temperature as a function of the teflon support width.

Next, the sample thermodynamics in impulsive measurements conditions can be estimated by modelling the system according to Fig.6.2. When the laser is turned on the heat flow contribution coming from the fraction of the input laser beam power that gets absorbed by the crystal must be added to the conductive and radiative components that are present in equilibrium conditions. As this simulation is aimed at obtaining a first rough feeling of the system thermodynamics in impulsive measurement conditions, we can use literature data on Silicon optical absorption for $\lambda = 1550\,\mathrm{nm}$ light in cryogenic environment to produce an estimate of the absorbed optical power contribution. Inheriting the [55] Silicon optical absorption estimate of $\alpha = 300\,\mathrm{ppm/cm}$ and approximating the beam optical path inside the sample as $l = 1\,\mathrm{cm}$, we can compute the constant absorbed optical power contribution as:

$$P_{In} = \alpha\, l\, P_{las} \tag{6.17}$$

where P_{las} is the total power of the input laser beam. Then, starting from the equilibrium temperature for each given teflon support width that was computed above, we can numerically solve the non-equilibrium thermodinamics first-order ordinary differential equations with the Euler method. Writing out the first-order expansion of the non equilibrium thermodynamics equation for the sample temperature we get:

$$\begin{aligned}\Delta T_{Si} =& \frac{P_{in} + P_{rad} - P_{cond}}{c_p^{Si}(T_{Si})\, m_{Si}} \Delta t \\ =& \frac{1}{c_p^{Si}(T_{Si})\, m_{Si}} \Big(\alpha\, l\, J_{las} + \sigma A_{eff}(T_{Sh}^4 - T_{Si}^4) - \frac{k_P(T_P) A_{cont}}{z_P}(T_{Si} - T_{Cu}) \Big) \Delta t\end{aligned} \tag{6.18}$$

where c_p^{Si} is the specific heat of crystalline silicon, which is a function of the silicon temperature T_{Si}, and m_{Si} is the sample mass.
There exist various references ([58], [59], [60]) in which c_p^{Si} has been empirically determined in the temperature range of intrest for our experiment. The c_p^{Si} values of the three references agree up to 1% relative differences across all the relevant temperature interval. The c_p^{Si} model in [58] is then taken as reference in all the thermodynamical simulations. A temperature-dependent Debye model:

$$c_p^{Si}(T_{Si}) = k \Big(\frac{T_{Si}}{T_D(T_{Si})} \Big)^3 \tag{6.19}$$

was used to obtain an analytical expression for the Silicon Specific Heat over the temperature range of intrest (Fig.6.15).

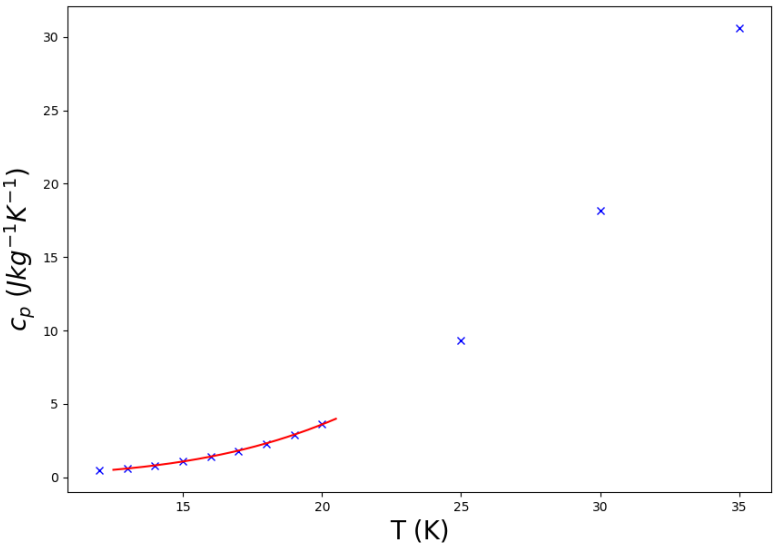

Figure 6.15: Specific Heat of crystalline Silicon containing less than 0.01% P-type impurities at cryogenic temperatures. Data from [58].

Then, assuming the copper and shield temperature as constant throughout all the transient and approximating the teflon temperature as the average of the temperatures of the two bodies contacting its surfaces ($T_P = (T_{Si} + T_{Cu})/2$), the sample temperature evolution can be computed by iterating Eq.6.18 and Eq.6.19 through sufficiently small Δt time steps. An example simulation of the evolution of the sample temperature in the $P_{las} = 1\,\mathrm{W}$, $z_P = 1\,\mathrm{mm}$ case can be seen in Fig.6.16, where the temperature rise clearly behaves as an exponential approach to new equilibrium temperature.

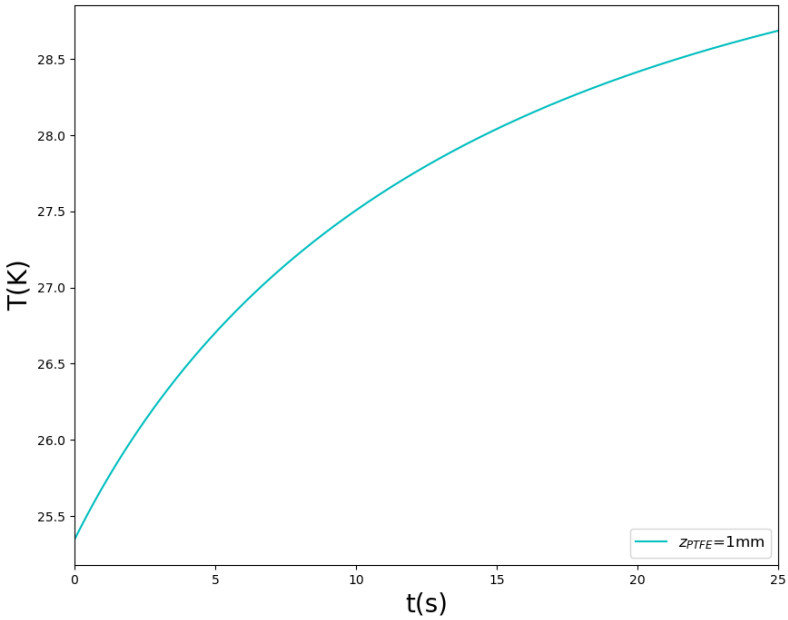

Figure 6.16: Example of impulsive measurement acquisition simulation.
Free parameters: $P_{las} = 1\,\mathrm{W}$, $z_P = 1\,\mathrm{mm}$.

It was performed at first a set of simulations where the input optical power P_{las} was kept constant while it was varied the teflon layer width. The temperature rise that resulted from each acquisition was fitted with an inverse exponential model:

$$T(t) = T_{In} + k\left(1 - e^{-\frac{t}{\tau}}\right). \tag{6.20}$$

The fit parameters obtained with with the above procedure are then plotted as a function of the teflon layer width in Fig.6.17. There is a monotonous increase of the characteristic time τ of the exponential temperature rise respect to teflon layer width. There is instead a decreasing trend in the temperature difference between the two initial and final equilibrium temperature for larger teflon layer widths, after the system reaches a maximum ΔT for $z_P \approx 2\,\mathrm{mm}$.

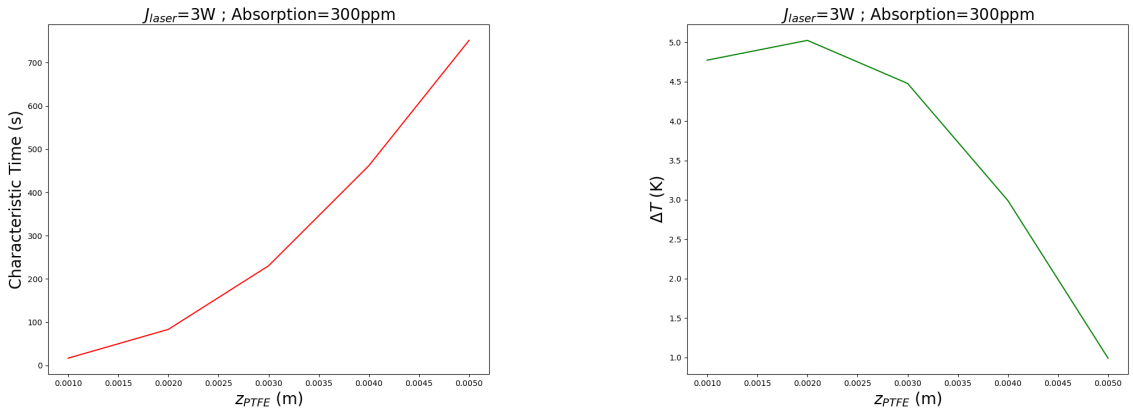

Figure 6.17: Fit parameters of z_P-varying impulsive measurements simulations.

A second set of simulations was performed by keeping a constant teflon layer width ($z_P = 2\,\mathrm{mm}$) and

varying the input optical power P_{las}. Due to the fact the relationship between input laser power and absorbed power is assumed to be linear, this analysis qualitatively illustrates the change in the system response to impulsive measurements as a function of the Silicon optical absorption coefficient. The plots illustrating the evolution of the main fit parameters as a function of the input optical power are shown in Fig.6.18. The characteristic time τ of the exponential temperature rise is weakly dependent from input power, while the ΔT parameter exhibits a linear proportionality respect to P_{las}. Then, if performing the final absorption measurement with the impulsive method, k is the only relevant parameter to extract for estimating the total absorption inside the sample. The characteristic time τ of exponential equilibrium temperature approach can be used instead as identifying signature for the sample induced signal.

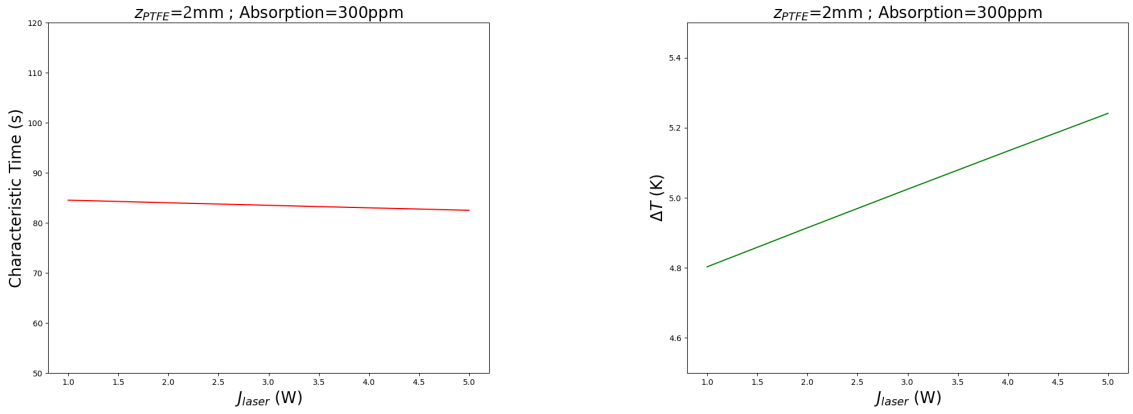

Figure 6.18: Fit parameters of P_{las}-varying impulsive measurements simulations.

From the above analysis it results that the impulsive measurement technique yelds a consistent method for identyfing the sample temperature variation signal. Moreover the characteristic time of the exponential sample temperature rise is at least of the order of $10^1\,\mathrm{s}$ for all the tested teflon layer configuration, so that it would imply that we could easily resolve the exponential rise by acquiring the CX-1050-SD temperature at $f_s \geq 5\,\mathrm{Hz}$ via Labview program. The main downside of the impulsive measurement is that it requires careful calibration for an accurate estimate of the sample optical absorption. In fact, due to the complicated form of the differential equation, it is not striaghtforward to relate the temperature change of the sample to the absorbed optical power. The calibration procedure consists in sending a known thermal flux to the sample and measure its temperature increase. However this procedure is unpractical and requires to be repeated for each sample. Furthermore one must assume that the thermal flux provided to the sample is know with good accuracy, for this assumption cannot be checked. If this is not the case for some reason, the measurement will bring along with it a systematic error.
In the end it was decided to settle to a $2\,\mathrm{mm}$ teflon layer prototype to ensure that the silicon sample exponential temperature rise under impulsive optical power input is easily resolvable at $[5-10]\,\mathrm{Hz}$ sampling frequencies ($tau_{2\,\mathrm{mm}} \approx 85\,\mathrm{s}$) in order to provide a characteristic signature signal that allows for debugging during Modulation Calorimetry measurement set up preparation.

6.2.5 Optical Line

A simple optical line was set up to allow for $\lambda = 1550\,\mathrm{nm}$ laser beam alignment and polarization tuning. The $\lambda = 1550\,\mathrm{nm}$ source was provided by a Keopsys CEFL-KILO-05 Erbium fiber Laser. The Keopsys laser is equipped a feedback system that allows for $< 0.5\%$ RMS output power stabilization in the $[0.5-5]\,\mathrm{W}$ range. A Faraday Isolator is installed after the fiber output to prevent beam reflection

from reaching back the laser cavity. A HWP phase retardating plate is mounted before the Farady Isolator to control the ratio of the transmitted versus reflected power at Faraday Isolator. A small portion of the optical line is reserved for the insertion of the IR-photodiode for system calibration purposes. A complete scheme of the optical line can be found in Fig.6.19.
Indepently of the selected measurement method, in order to properly perform an absorption measurement the optical line must met few crucial constraints. First of all, all reflections inside the cryogenic chamber must be minimized, in addition to prevent beam clipping phenomena, as any excess input power contribution would spoil the system thermodynamics when operated at cryogenic temperatures. In fact the aim of the experiment is to measure few ppm absorption on the silicon crystal, so that alternative sample heating sources could easily dominate the absorption contribution and must be minimized. To this purpose the beam-sample system will be aligned at Brewster Angle to minimize the reflected power at sample input surface; a Qarter Waveplate-Half Waveplate system was installed just before the input window of the cryogenic chamber to control polarization ellipticity and orientation; the p-polarized beam is then accurately aligned respect to the sample input surface, which is already placed at $\Theta_B \approx 74^\circ$ respect to the chamber optical axis, by means of two steering mirrors that are placed before the QWP-HWP system.

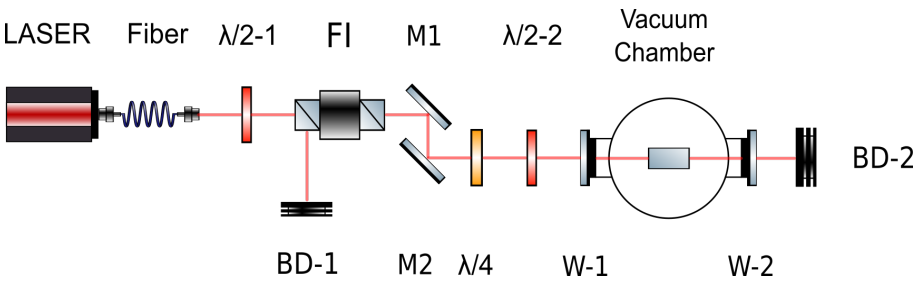

Figure 6.19: Schematic view of the optical line. $\lambda/2$: half waveplate; $\lambda/4$: quarter waveplate; FI: faraday isolator; BD: beam dump; M: mirror; W: window.

In order to perform a ppm-accurate power absorption measurement, all the optical line elements must be carefully characterized to have precise control of the optical power that is injectted into the sample. The CEFL-KILO laser working principle is to have a fixed output power seed laser that gets independently amplified by a doped erbium fiber to enhance the laser output power. The Keopsys laser has two different operation mode: Automatic Current Control (ACC) and Automatic Power Control (APC). In ACC mode the user can control the setpoint of the current supplying the amplification fiber while output power is unstabilized; in APC mode the system asks to specify an output power setpoint, so that a feedback control system is turned on to actively tune the amplifier current to obtain a drift-less, stabilized output power signal. The APC mode power stabilization system takes a finite time of $O(1\,\mathrm{s})$ to reach equilibrium around the desired power setpoint. Then it is not possible to perform a Modulation Calorimetry measurement in APC control mode, as the modulation frequency would be constrained to excessively small values[7].A sinusoidally modulated output power can be instead obtained by operating the instrument in ACC mode and accounting for eventual output power instabilities. To this purpose it was performed at first a $P(I)$ calibration acquisition to determine whether and in which range the laser power amplification was linear. A plot illustrating the output power response as a function of amplifier current variation is shown in Fig.6.20. Both quantities were acquired with the Keopsys CEFL-KILO internal sensors. Output power sensor accuracy has been independently tested with a Thorlabs infrared powermeter.

[7]The APC is instead the ideal operation mode for an impulsive measurement. After having waited for the laser output power to stabilize while the beam is dumped, the beam dump is removed and stabilized input power flows steadily through the sample.

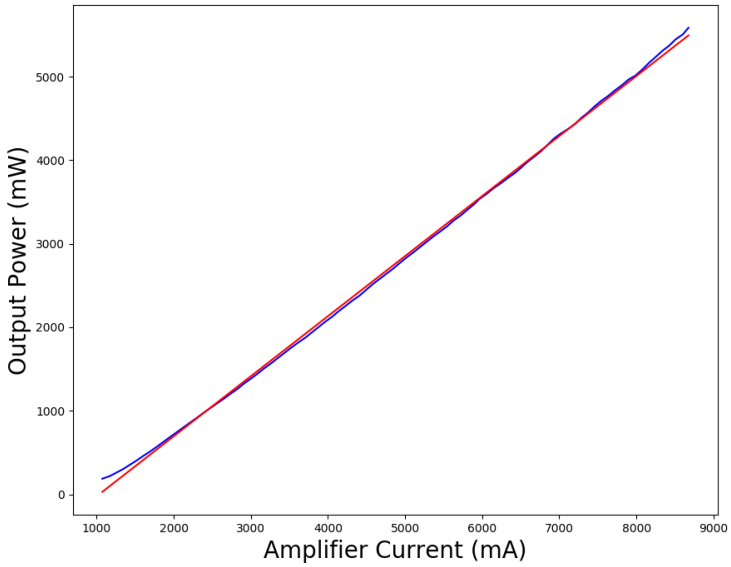

Figure 6.20: Keopsys CEFL-KILO $P(I)$ calibration.

a (mW)	b (mW/mA)
-783 ± 8	0.724 ± 0.001

Table 6.5: Keopsys CEFL-KILO calibration fit parameters ($P(I) = a + b\,I$).

The (I, P) data points distributes linearly in the $([2 - 8]\,\mathrm{A}, [0.7 - 5]\,\mathrm{W})$ range, while outside of it the laser power behaviour starts becoming non-linear. A linear model fit to the experimental data was performed in this region.
As a consequence, modulating with a sine wave the amplifier current in the $[2 - 8]\,\mathrm{A}$ region it is expected an analogous sinusoidal response of the laser output power in the $[0.7 - 5]\,\mathrm{W}$ range. The Amplifier current sinusoidal modulation was digitally performed via Labview program which was interfaced to the laser through a dedicated serial port. The main issue in the amplifier current modulation was posed by the fact that the instrument is only able to support current slopes up to $(dI/dt)_{Max} = 875\,\mathrm{mA/s}$ (Maximum Current Slope). If the system is asked to perform a given ΔI current variation, it will reach the new current setpoint after a time interval equal to $\Delta t = \Delta I/(dI/dt)_{Max}$.
A limitation to the current variation translates in a constraint on the slope of output power variations: $(dP/dt)_{Max} = b\,(dI/dt)_{Max} \approx 630\,\mathrm{mW/s}$ (Maximum Power Slope). In fact this turns out to be a limitation in the modulation amplitude of the output power signal as a function of the modulation frequency. By increasing the modulation frequency at fixed modulation amplitude the zero-crossing region of the sine wave, where the signal derivative is maximal, will eventually overcome the Maximum Power Slope limit, causing the output signal to be distorted and the effective modulation amplitude to be reduced.
In addition to the physical limitation to current/power variations in the system there is also a second issue for Modulation Calorimetry measurements: if the instrument is asked to perform a current variation that exceeds the maximum current slope treshold, retardation in serial communication with the main PC starts adding up, eventually leading to a control program crash that could not be avoided at

programming level. Then, to avoid potential acquisition-killing crashes, when operating the system at a given modulation frequency ω the current modulation amplitude should be mantained below a certain safety value . This ω-dependent safety value has been empirically determined by testing the system at different modulation frequency, progressively increasing the modulation amplitude until crashes were induced in the read-out Labview program. The power modulation amplitude value that divides the safe operative region from the crash-inducing range of the parameter space is plotted as a function of modulation frequency in Fig.6.21. The experimental data was fitted with a parametric iperbolic model to account for output power attenuation when actuating at higher frequencies[8]:

$$P_{Las}(\omega_p) = \begin{cases} \frac{k}{\omega_p} & \text{for } \omega_p \leq \omega_c \\ \frac{k}{\omega_p}\frac{q+m\,\omega_p}{q+m\,\omega_c} & \text{for } \omega_p > \omega_c \end{cases} \tag{6.21}$$

where $\omega_c = 0.18\,\mathrm{Hz}$ is the critical frequency for output power attenuation. A control system was implemented in the Labview read-out program to prevent working in the unsafe region of the parameter space.

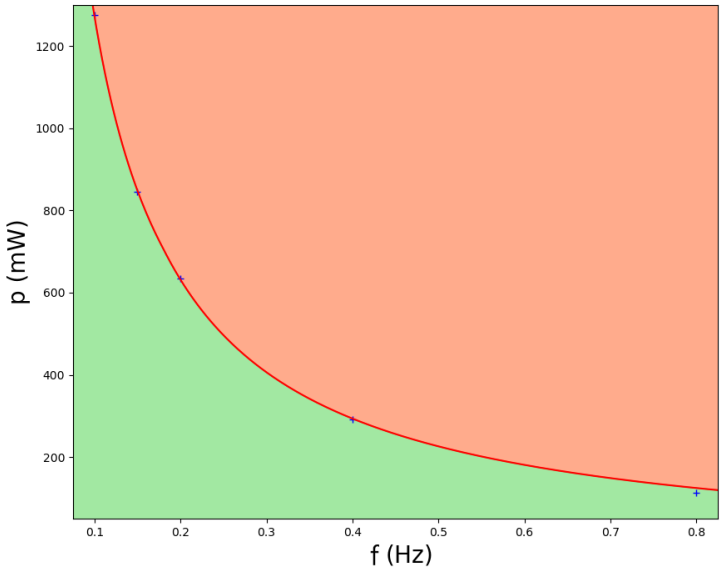

Figure 6.21: Allowed (green) and unsafe/prohibited (red) optical power modulation amplitudes at fiber output as a function of the modulation frequency. Power Modulation: $P(t) = P_0 + p\sin(f\,t + \phi)$.

Special care must be given to ensure that the beam is entering and exiting the sample in a central position respect to the sample surfaces, so that beam clipping on the sample is minimized. In order to further minimize beam clipping on the sample a focalizing lens with focal length approximately equal to the chamber radius should have been mounted in front of the entrance window, so to drastically reduce the radius of the beam that is entering the sample; as we did not dispose of a lens of such focal lenght, the only option to decrease the beam radius inside the sample was to reduce as much as possible the optical path of the line before the chamber.

[8]The attenuation was caused by a modulation frequency dependent phase retardation between power and current signals. When the amplifier current is increased, output power starts increasing after a finite amount of time, so that when the current modulation reaches its maximum value, power modulation is not fully completed and cannot achieve values as the amplifier current starts decreasing after that moment.

k (WHz)	q	m (Hz^{-1})
0.1272 ± 0.0002	0.727 ± 0.002	-0.085 ± 0.004

Table 6.6: Parametric model fit parameters for the constraint on power modulation amplitude. ($\omega_c = 0.18\,\mathrm{Hz}$)

It is then of primary importance to obtain informations on the spatial evolution of the beam radius along the optical line. It should be recalled that the sample input/output surfaces are rectangles of size $2 \times 1\,\mathrm{cm}$[9] and that the sample is entered at Brewster angle, that for Silicon at $\lambda = 1550\,\mathrm{nm}$ light corresponds to $\Theta_B \approx 74°$. In order to comply with the 3σ rule for safe beam interaction with optical element, the largest beam radius that could be tolerated at input surface, accounting for the non-zero angle of incidence, is $r^{max} = \frac{l_x \cos(\Theta_B)}{6} \approx 0.9\,\mathrm{mm}$. As said, the only option that was available to reduce the beam radius in the sample region below this threshold was to minimize the optical line lenght.
It is then crucial to determine the spatial evolution of the beam radius along the line. CEFL-KILO fiber laser provides an highly collimated output laser: its waist w_0 is located in the fiber output region and its Rayleigh Range z_R is of $O(1\,\mathrm{m})$. This allows to linearize the evolution of the beam radius in the spatial range of the optical line, which is small if compared to z_R. A knife edge test was performed at two reference distances from the output fiber so to retrace the spatial evolution of the beam in between them. The two knife edge tests data is shown in Fig.6.22 along with a least square fit of the model describing trasmitted power for a partially truncated beam:

$$s(x) = \frac{P}{2}\Big[1 - \mathrm{erf}\Big(\frac{\sqrt{2}(x - x_0)}{w_z}\Big)\Big] \tag{6.22}$$

where x is the position of the scanning knife edge, x_0 is the center of the beam, P is the total power contained in the laser beam, and w_z is the $1/e^2$ beam radius at position z along the optical line. The two knife edge test were permormed at $z_1 = 50\,\mathrm{cm}$ (blue) and $z_2 = 120\,\mathrm{cm}$ (red) distance from the fiber output.

z (cm)	P (mW)	x_0 (mm)	w_z (μm)
50	53.9 ± 0.1	0.035 ± 0.002	808 ± 5
120	107.0 ± 0.2	-0.049 ± 0.003	997 ± 7

Table 6.7: Knife edge tests fit parameters.

Having performed two beam profiling acquisitions far from the waist at fiber output in terms of the beam Rayleigh range, it is possible to approximate the beam propagation as linear. Then in order to satisfy the 3σ requirement for beam clipping minimization, in absence of focalizing lenses, it is necessary to reduce the optical distance between fiber output and sample, which is placed at the center of the cryogenic chamber horizontal plane, below $l_{opt}^{max} = 80\,\mathrm{cm}$, so that the beam radius at sample center would be smaller than $r^{max} = 0.9\,\mathrm{mm}$. The optical line length was minimized and the fiber output-sample center distance was set to $l_{opt} = 60\,\mathrm{cm}$.
After having mounted and characterized the optical line, it was performed a characterization of the power budget after each optical element. Following the path of the optical line, the first optical element to be characterized was the Faraday Isolator. An optical isolator is a device which allows the

[9]The $l_x = 2\,\mathrm{cm}$ side is placed parallel to the optical plane while the $l_y = 1\,\mathrm{cm}$ side is perperndicular.

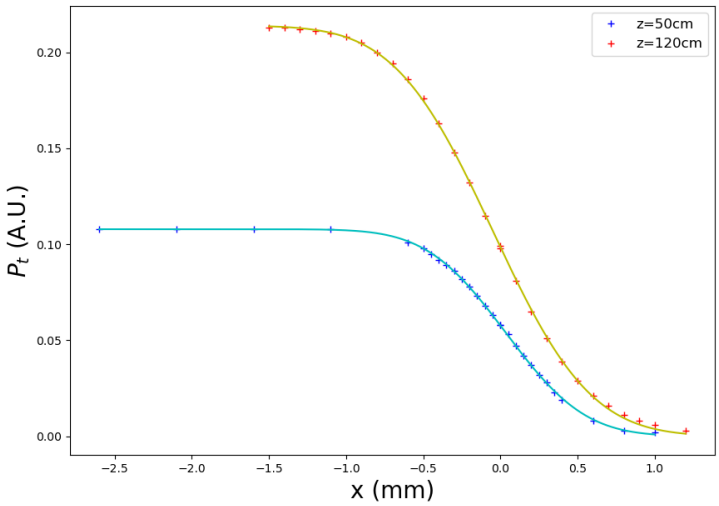

Figure 6.22: Transmitted power versus knife edge position for tests performed at $z_1 = 50\,\mathrm{cm}$ (blue) and $z_2 = 120\,\mathrm{cm}$ (red) distance from the fiber output.

transmission of light in only one direction, so that it is used to prevent unwanted feedback into an optical oscillator, such as a laser cavity. The Faraday Isolator is made of two polarizing beam splitters rotated by $45°$ respect to each other separated by a $45°$ polarization rotator, which ideally allows all the correctly polarized input radiation to be transmitted through the second polaroid, while completely disallowing the $45° + 45° = 90°$ rotated backreflection to pass through the input polaroid. The Faraday Isolator is used in combination with a HWP polarization rotator placed before the input polarizer to control the system transmittance. Considering the case of a real optical isolator system the $T = 1$ condition cannot be achieved due to small orientation misallignments in the PBS-rotator system and small optical absorption inside the various optical elements. It is then necessary to characterize the transmittance of the system.
In order to determine the maximal transmittance of the optical isolator system, the input HWP was rotated to different $\theta_{\lambda/2}$ angle on the mounter while acquiring the transmitted power P_T after the Faraday Isolator with a powermeter. The laser output power was set to $P_{Out} = 1\,\mathrm{W}$ (APC control mode). The result of the acquisition is shown in Fig.6.23. The experimental dataset was fitted with a Malus' law model:

$$P_T(\theta) = P_T \cos^2\left(2(\theta_{\lambda/2} - \theta_{\lambda/2,0})\right) \tag{6.23}$$

where $\theta_{\lambda/2,0}$ is the HWP rotary mounter orientation for transmission maximization.

P_T (W)	$\theta_{\lambda/2,0}$ (deg)
0.974 ± 0.002	173.64 ± 0.06

Table 6.8: Malus'Law fit parameters for $P_T(\theta_{\lambda/2})$ data (Fig.6.23).

As the transmitted power versus polarization orientation data is well fitted by Malus' Law model, it is possible to perform an analogous analysis with varying laser output power to investigate possible non-linear effects in the optical isolator system transmittance. The maximum transmitted power P_T^{max} is plotted against the Output power of the Keopsys laser, which directly inputs the optical isolator system

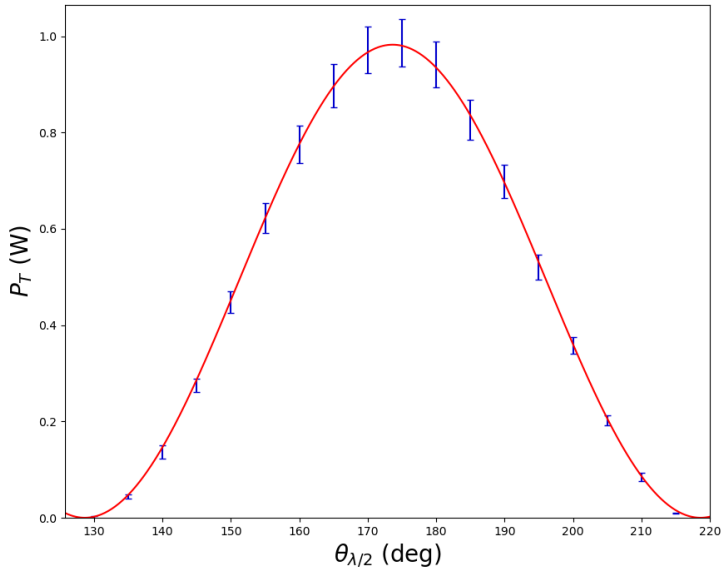

Figure 6.23: Transmitted power of the optical isolation system as a function of the HWP rotation angle (Input power: $P_{Out} = 1\,\mathrm{W}$).

(Fig.6.24). Experimental data is fitted with a linear model to investigate for departures from linearity. As linear behaviour of the optical isolator system is verified, the linear slope coefficient extracted from the fit quantifies the power-independent maximal transmittance of the optical isolator system: $T_{FI}^{Max} = 0.974 \pm 0.002$.

a (W)	b
0.000 ± 0.002	0.974 ± 0.002

Table 6.9: Optical isolator system: maximum transmitted power versus input power. Fit model: $P_T^{Max}(P_{Out}) = a + b\,P_{Out}$

6.2.6 Digital Acquisition and Control System

In order to perform the laser power modulation required from Modulation Calorimetry technique and to acquire both the sample temperature and output power modulated signals a dedicated Labview program was designed (Fig.6.25). All the various thermometers reading instruments were interfaced with the laboratory PC via GPIB connection, while the laser output control and acquisition was performed via serial comunication.
In its final version the acquisition and control program allows for complete monitoring of the system thermodynamics through real time acquisition and plotting of the in-loop and out-of-loop thermometers. The laser power modulation protocol was the following: as already explained, in order to have a fast response of the laser output to external cavity setpoint variations it is necessary to control the instrument in ACC mode; the user selects the parameters describing the power modulation curve (amplitude, frequency and offset); then the appropriate modulation for the laser current is computed using

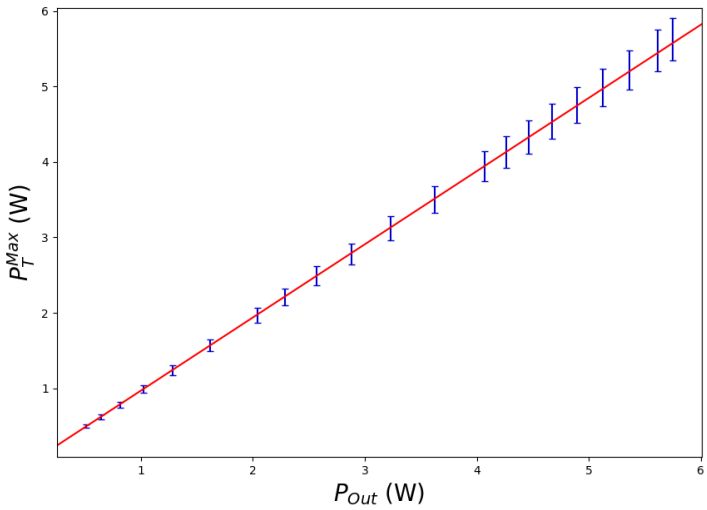

Figure 6.24: Maximum transmitted power versus input power of the optical isolator system.

Tab 6.5; the generated waveform is then discretized with a sampling frequency decided by the user; finally the laser current is adjusted at the so-determined setpoints, according to the time step decided by the user. When current and power modulation is started, two dedicated displays monitor in real time the laser amplifier current and output power signals that are acquired via the Keopsys CEFL-KILO internal multimeter and powermeter; acquisition of the sample temperature and output power signals can be started after the system has started responding to power modulation; achievement of the adiabatic regime condition can be monitored in real time with a dedicated indicator which extract phase shift information in temperature versus power oscillations by real-time fitting of small portions of the two signals.
A single cycle of the program acquisition and control while loop takes on average $t_{cycle} = 50 \pm 10\,\mathrm{ms}$ to be performed on a Desktop PC with Windows 7 operative system. This allows to run acquisitions at $f_s \approx 15\,\mathrm{Hz}$ sampling frequency without problems. As a consequence, beam power modulation could be performed at frequencies up to few Hz to obtain a fairly smooth and detailed digital sine wave. An indicator was placed on the program front panel to monitor the number of cycles that took a larger time than the sampling period to be completed.

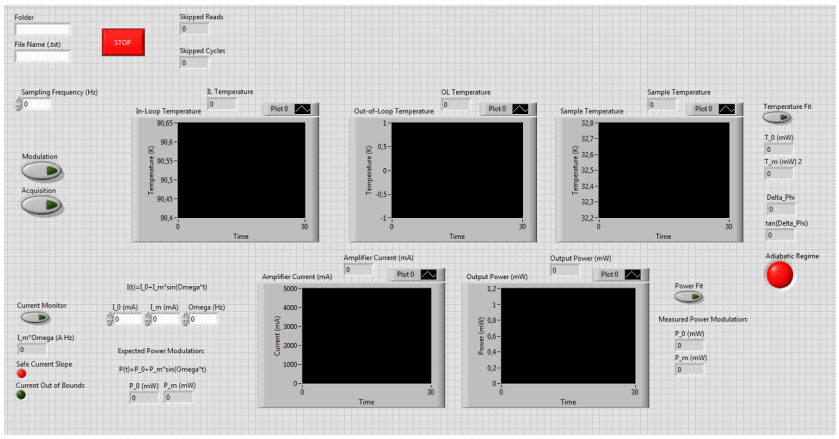

Figure 6.25: Front panel of the Labview program that automatized laser power modulation and temperature signal acquisition.

Different versions of the read-out program were built to allow for photodiode signal acquisition and a dedicated version allowed for the acquisition of the three temperature signals only in the case impulsive type of absorption measurements were performed. All the versions of the read-out program supported the possibility to monitor the system thermodynamics during cooling phase from ambient to cryogenics temperatures by implementing the full range calibration of Tab.6.4 for the sample temperature signal. When cryogenics temperature were achieved on the sample and the set up was ready for absorption meausurements, CX-1050-SD signal conversion switched to the static calibration curve (Tab.6.3), that was more accurate in the environmental conditions of the final absorption measurements.

6.2.7 Expected Sensitivity of Design Set-Up

Given that in the basic equation of Modulation Calorimetry the unknown parameter is the amplitude of absorbed power oscillation p_{abs}, one must investigate the main factors contributing to the uncertainty in the determination of the quantities in the right hand side of Eq.6.7 to estimate in advance the expected accuracy of the final absorption measurment. Moreover, it is of primary importance to evaluate when the adiabatic regime condition $\tan(\phi) > 10$ is met in our experimental system.
Concerning uncertainties in the determination of Eq.6.7 parameters, the estimate of the sample mass m and input power oscillation frequency ω_p measurements can be easily made with sub-$\%$ accuracy. Furthermore a detailed discussion over the determination of crystalline Silicon specific heat c_p at cryogenic temperatures has been carried out in Sec.6.2.4, allowing for O($\%$) accuracy also on the estimate of this quantity. The main uncertainty contribution in the right hand of the expression remains the measurement of small temperature oscillations amplitude Θ_0.

The optically induced temperature oscillations in the Silicon crystal will be extracted from a noisy sample temperature signal. The main noise contribution to the temperature signal acquired with the CX-1050-SD thermometer comes from the limited ability to stabilize the temperature of the sample in proximity to the equlibrium value. A PID controlled resistive heater is installed on the copper support that is conductively coupled to the sample by means of a $z_P = 2\,\mathrm{mm}$ wide teflon layer; fluctuations in the radiation heat flow contribution are not minimized instead, as the temperature of the copper radiation shield is not actively stabilized. With this configuration the temperature fluctuations acquired on the sample with the CX-1050-SD thermometer in steady-steate laser beam shining conditions exhibit a $0.001\,\mathrm{K}$ RMS. Therefore, in order to detect optical absorption induced temperature oscillation on the sample it is necessary to set up an experimental apparatus that is capable of producing $\Theta_0 = O(10^{-3}\,\mathrm{K})$ modulation on the sample.

As provided by Eq.6.7, sample temperature oscillations are proportional to the absorbed power oscillation, that in its turn is proportional to the input laser beam power oscillation. Therefore amplitude of input power modulation should be made as large as possible to maximize sample temperature oscillations while complying with the adiabatic regime constraint. Recalling from Sec.6.1, the requirement for adiabatic regime approximation was set to:

$$\tan(\phi) = \frac{m c_p^{Si} \omega_p}{Q'} \geq 10. \tag{6.24}$$

Hence the adiabatic regime requirement on the tangent of the phase shift between temperature and power oscillations can be fulfilled by performing the Modulation Calorimetry measurement at a sufficiently high modulation frequency ω_p. To establish the lowest modulation frequency working point for achieving adiabatic regime it must be estimated the heat transfer coefficient $Q' = dQ/dT$ in the cryogenic chamber system.
At equilibrium the heat flow contributions that dominate the sample thermodynamics are heat conduction to the copper support through teflon and radiation heat from the shield. A variation in the laser

beam input power would induce a variation in the temperature of the sample, which would eventually induce a variation in the two main heat flow contributions. Summing up and linearizing heat flow equations Eq.6.14 and Eq.6.15 for an arbitrary small sample temperature variation, an expression is obtained for the first order heat flow variation coefficient:

$$Q' = \frac{k_P A_C}{z_P}. \tag{6.25}$$

As a rough estimate, thermal conductivity of teflon can be approximated as a temperature independent quantity in the temperature range of intrest for the experiment: $k_p \approx 2{\times}10^{-1}\,\mathrm{WK^{-1}m^{-1}}$ ([57]). Hence by substituting also the support system design quantities $A_C = 2 \times 10^{-5}\,\mathrm{m}^2$ and $z_P = 2 \times 10^{-3}\,\mathrm{m}$ the estimate of the heat flow coefficient results as: $Q' \approx 2 \times 10^{-3}\,\mathrm{WK^{-1}}$.
Isolating ω_p in Eq.6.24 it can be obtained a temperature dependent equation for the minimum power modulation frequency required to fulfill the adiabatic regime condition:

$$\omega_p \geq \frac{10\,Q'}{m c_p^{Si}(T_{Si})}. \tag{6.26}$$

Inserting in the above equation the estimate for the heat flow coefficient Q' and the model for Silicon specific heat in cryogenic environments that was developed in Sec.6.2.4, the adiabadic regime requirement on modulation frequency can be computed across all the temperature range of intrest for the experiment. A plot illustrating the adiabati regime region in the frequency space as a function of the Silicon crystal temperature can be seen in Fig.6.26.

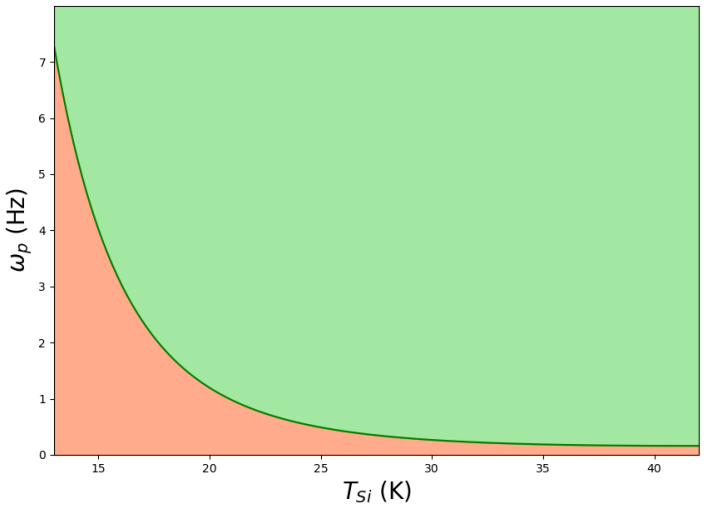

Figure 6.26: Temperature dependent requirement on modulation frequency to enter adiabatic regime. Green: adiabatic regime conditions; Red: non-adiabatic regime conditions

Remembering the $\omega_p^{<}1\,\mathrm{Hz}$ constraint on modulation frequency imposed by the finite sampling frequency allowed for digital modulation and acquisition, it follows that the adiabatic regime is easily attainable when working in the $T_{Si} > 20\,\mathrm{K}$ temperature range. Below such temperature greater care must be placed in performing a Modulation Calorimetry measurement: either the Modulation Calorimetry equations must be used outside of the adiabatic regime approximation or the experimental set up must be modified to allow for a different beam power modulation method.
The above constraint on modulation frequency has to be put together with the modulation frequency dependent limitation on the amplitude of laser beam power oscillations. In Sec.6.2.5 it was empirically

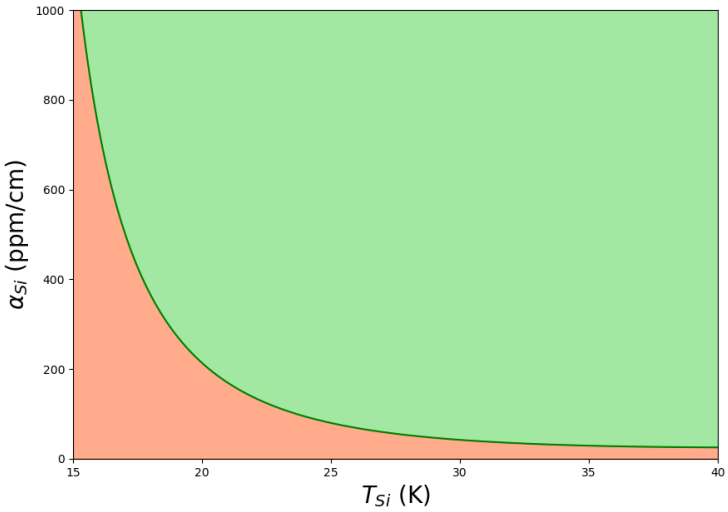

Figure 6.27: Lower limit on the detectable silicon absorption coefficient with design set up.

obtained a parametric model describing the maximum allowed power modulation amplitude P_{Las} as a function of the modulation frequency ω_p (Eq.6.21).
The lower limit on the input power modulation amplitude of Fig.6.26 eventually translates in a lower limit on the detectable optical absorption coefficient of crystalline silicon. This is because the $\omega_p(T_{Si})$ lower limit can be mapped to a $p_{Las}(T_{Si})$ upper limit through the Fig.6.21 constraint. As p_{Las} is proportional to Θ_0, with α_{Si} being the linear proportionality coefficient between the two quantity, for each maximal input power oscillation amplitude p_{Las} it is possible to find the α_{Si} value that renders the sample temperature oscillation amplitude Θ_0 too small to be detected. A sample temperature oscillation is conventionally considered detectable if it exceeds the sample temperature fluctuation RMS at equilibrium ($T_{Si}^{RMS} = 10^{-3}\,\mathrm{K}$). By performing the former computation, Fig.6.27 constraint on the minimum detectable silicon absorption coefficient as a function of the sample temperature in the design set up is obtained.
Ultimately, the Modulation Calorimetry technique will allow to perform $\alpha_{Si} \leq 300\,\mathrm{ppm/cm}$ measurement in all the $T_{Si} \geq 20\,\mathrm{K}$ temperature range. This would be already enough to independently verify or contradict [55] estimate of crystalline silicon optical absorption, which is the only direct measurement of this quantity for $\lambda = 1550\,\mathrm{nm}$ light and cryogenic environment that is present in literature. At lower temperatures the sensitivity of the Modulation Calorimetry technique to α_{Si} measurements fastly degrades. If it is desired to carry on the study of Silicon optical absorption at below-$20\,\mathrm{K}$ temperatures, then it is either needed to consistently modify the experimental set-up to allow for a faster and larger amplitude power modulation or to switch to an impulsive type of measurement, which would be able to provide a sub-$\%$ accuracy absorption measurement at the cost of lenghtier calibration process.

Chapter 7

Data Acquisition and Analysis

After all the components of the experimental system were designed, realized and tested, the whole apparatus was assembled inside a clean room in the LAE building at the Laboratori Nazionali di Legnaro. Once the performances of the power modulation and read-out system were optimized, several data acquisition campaigns were attempted. The optical line and cryogenic chamber set up were progressively modified between one set of acquisition and the other in order to tackle the major issues that arised after the analysis of the data acquired with each test configuration. Both impulsive and modulated measurements were performed during each single campaign: even if the acquisitions that were performed with the impulsive technique were uncalibrated, it was useful to compare the experimental data to numerical simulations for debugging purposes.
In this section will be presented the various tests that were carried out to investigate and analyze the main causes of systematic error affecting both impulsive and modulated measurements. The two final data acquistion campaigns will be illustrated in detail to point out the evidences and considerations that led to the conclusive estimate of the crystalline Silicon optical absorption coefficient.

7.1 Experimental System Preparation

Before starting each data acquisition campaign it was necessary to properly set up the optical system and, having found the optimal beam-sample system configuration, to seal the cryogenic chamber. At first the crystalline silicon sample was placed on its teflon housing support; the system was oriented such that the sample input surface was approximately at Brewster angle for crystalline silicon ($\theta_B \approx 74°$) respect to the optical axis of the cryogenic chamber; the laser beam was turned on and it was slightly misalligned respect to the optical axis of the chamber, so that the beams that entered and emerged from the sample were simmetrical respect to the optical axis of the cryogenic chamber (Fig.7.1b). This allowed the transmitted beam to be evacuated from the chamber output window without having to steer it with a pair of mirrors. The beam-sample system was then carefully oriented at Silicon Brewster angle by acquiring and maximizing the transmitted beam power at chamber exit with the IR-photodiode, placing special attention on avoiding to indroduce beam clipping in the system. Brewster angle orientation was fine tuned by acting on the two degrees of freedom of the mirrors-HWP system that was placed in front of the chamber input window. Despite extensive efforts, the maximum transmittance value that could be achieved on the sample-beam system was incompatible with the ($T_p = 1$,$R_p = 0$) theoretical expectation. As the angle of incidence of the laser beam on the input surface of the sample could be controlled very precisely by acting on the mirror mount orientation screws, it was suspected that the problem was caused by a residual fraction of s-polarization in the input beam.
In fact, the polarization orientation of the input beam could only be controlled before the input window of the cryogenic chamber by means of a HWP and the beam is assumed to input the HWP in a linearly polarized state, as it was previously transmitted through the two polarizing beam splitters of

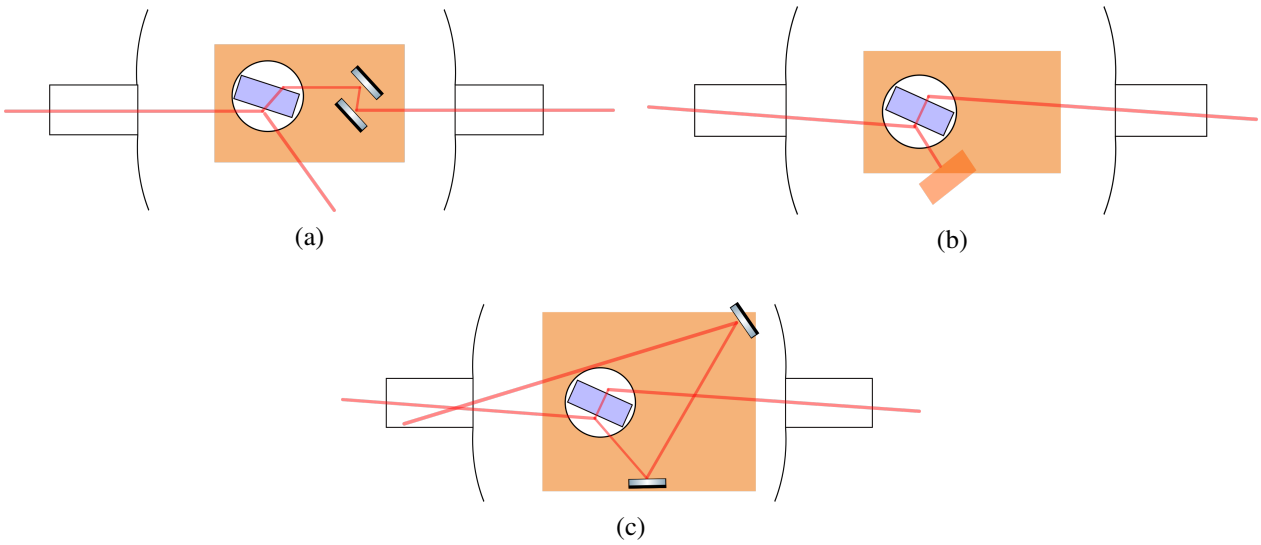

Figure 7.1: Schematical comparison of tested optical configurations in the cryogenic chamber. $a + b$: first acquisition campaign. c: second acquisition campaign.

the Faraday isolator. Moreover it was inserted a QWP right before the HWP to test this assumption by counteracting a potential deviation from linearity in the polarization of the faraday isolator transmitted beam. The maximum transmittance value of the cryogenic chamber system that was achieved after optimization of the three degrees of freedom of the optical system in this configuration was $T = 0.94 \pm 0.01$. As crystalline Silicon optical absorption for $\lambda = 1550\,\mathrm{nm}$ light at room temperature is negligible ([51]), it was concluded that all the missing transmitted power was reflected due to a slight depolarization happening at the cryogenic chamber input window.
This excess reflection could be a threat to the success of the Silicon optical absortion measurement. In the case of an impulsive type of measurement, the sample will be tested with different input power set point conditions ranging up to the largest setpoint value that the feedback control system of the Keopsys laser is able to operate, that is $P_{Las}^{Max} \approx 5\,\mathrm{W}$. In the case of a Modulation Calorimetry measurement, the laser will be controled in ACC mode to allow for power modulation with the largest possible amplitude at each given modulation frequency, that can reach up to $p_{Las} = 2\,\mathrm{W}$ at lowest frequencies. In both situations, considering the previous $R \approx 0.05$ estimate, this would translate in a $P_{Ref} \approx 100\,\mathrm{mW}$ reflected power that is confined and eventually absorbed inside the cryogenic chamber. At cryogenic temperatures this excess power could significantly alter the chamber thermodynamics that were modeled throughout the previous section.

Fit parameter	Old Configuration	New Configuration
$b\,(\mathrm{K/s})$	$8.98 \pm 0.03 \times 10^{-4}$	$1.91 \pm 0.01 \times 10^{-4}$

Table 7.1: Linear proportionality coefficient of the room temperature impulsive test acquistions. Fit model: $\Delta T(t) = a + b\,t$.

An initial test was conducted at room temperature, before sealing up the chamber. An impulsive type of measurement was performed with a $P_{Las} = 4\,\mathrm{W}$ beam on the sample. A comparison between two such acquisitions is showed in Fig.7.2. The blue-marked acquisition is relative to the very first test configuration, where the optical line lenght was still unminimized so that a non negligible portion of the input beam was not able to correctly enter the sample input surface, thus being directly scattered

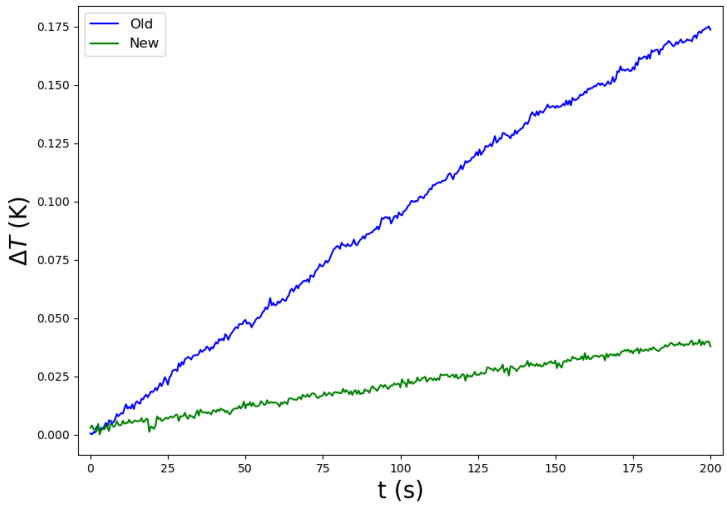

Figure 7.2: Comparison of room temperature impulsive measurement tests performed in two different system configurations. The slope of the sample temperature rise quantifies the spurious effect of excess beam reflections and scatterings inside the chamber.

across the chamber; the green-marked acquisition is relative to a later configuration where the beam clipping issue on the sample was mitigated. The two acquisitions were fitted with a linear model to quantify the undesired effect of excess beam reflections and scatterings in the chamber. Despite the order of magnitude improvement in the slope of the temperature rise, the slope of the sample temperature rise that was observed during the room temperature impulsive test could not be lowered below $b \approx 10^{-4}\,\mathrm{K/s}$ values. The first acquisition campaigns were then started to investigate the effects of the excess reflection on the system thermodynamics in a cryogenic environment, in addition to other possible issues in the experimental set up.

7.2 First Acquisition Campaign

During the first acquisition campaign two different cryogenic chamber configurations were tested. The first configuration was exactly the one described throughout Sec.6.2, where the sample was simply placed on its teflon housing and the laser beam was transmitted through the chamber and the crystal without active steering. As an alternative approach, a second configuration was prepared where a custom made copper beam dump was clamped to the copper support. The beam dump was designed to capture and absorb the window depolarization induced reflection, so that the excess input power could be actively compensated by the PID heater counteraction.
For reasons that will be made clear throughout the following section, the data acquisitions performed in this two configurations gave similar results, so that they are presented together.

7.2.1 Impulsive Measurements

Despite the fact that it was not possible to properly calibrate impulsive acquistions, so that this first measurment method could not produce an accurate estimate of the silicon optical absorption coefficient, it was useful to start each acquisition campaign by performing a set of impulsive measurements

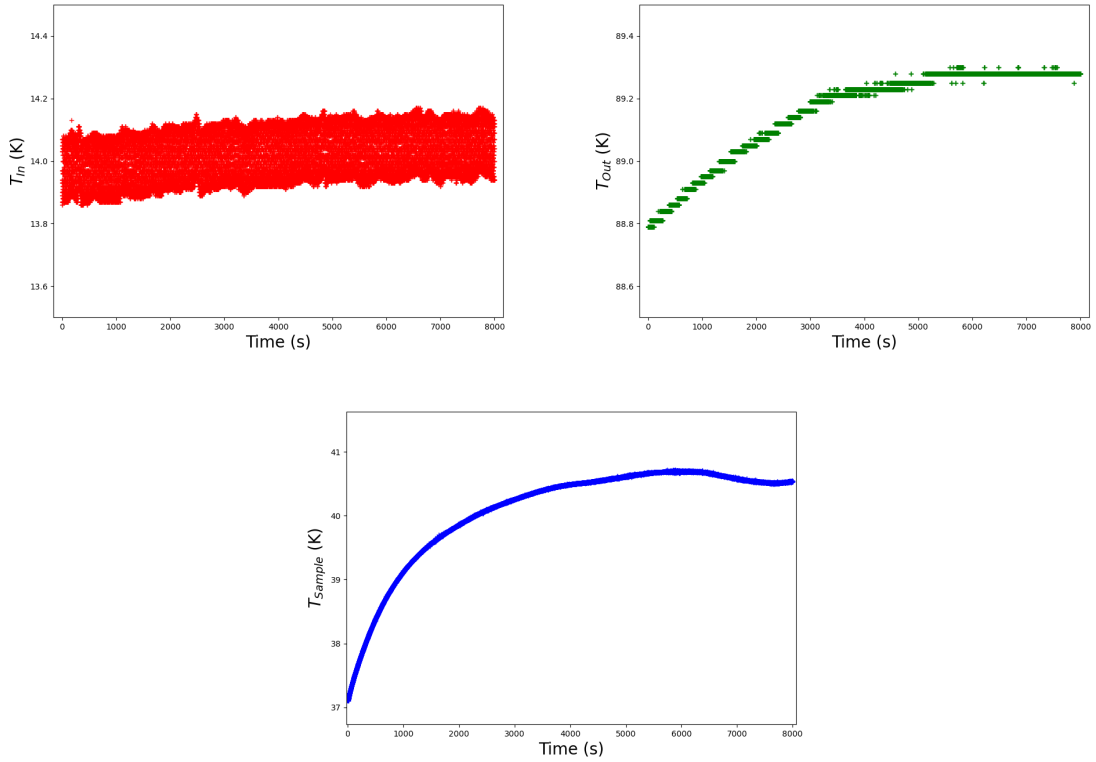

Figure 7.3: $P_{Out} = 2\,\mathrm{W}$ impulsive measurement acquisitions of in-loop DT-470 (up left), out-of-loop DT-470 (up right) and CX-1050-SD (down) signals.

to check if the system behaves according to the numerical simulations that were performed during design phase. Moreover impulsive acquisition would allow to extract complementary informations on the system thermodynamics compared to modulated measurements. Evidence obtained from impulsive measurements will then enable a complete understanding of the system thermodynamics.

Impulsive type of optical absorption measurement were performed according to the following procedure. After the system reached equilibrium at cryogenic temperatures the laser was set in APC mode and all the output power was blocked before entering the chamber; the data acquisition was started approximately $20 - 30\,\mathrm{s}$ before removing the beam dump; the beam dump was removed and the three temperature signal were recorded; the acquisition was stopped and the beam dump reinsterted in the optical line to allow for the system to cool down. The cool down phase should ideally be carried on until the system reaches thermal equilibrium conditions.During the first tests of the impulsive technique, data acquisition was performed from the starting point of the exponential temperature rise up until the new equilibrium was reached. The higher temperature equilibrium condition usually took more than one hour to be reached and the temperature rise covered a $\Delta T \approx 5 - 10\,\mathrm{K}$ range. Fig.7.3 illustrates an example of $P_{Out} = 2\,\mathrm{W}$ long-term impulsive acquisition, during which the PID temperature stabilization system on copper was turned off to investigate the influence on chamber thermodynamics of low frequency drifts in the cryocooling power and in the input optical power.
In the first hour portion of the above acquisition the sample temperature exhibits a clear exponential temperature rise, while in the second portion low frequency input/output power instabilities start dominating the thermodynamics of the Silicon crystal. The first portion of acquired data can be fitted with an exponential model such as the one presented in Eq.6.20. It can be immediately seen that the long term acquisition does not match with the simulated sample thermodynamics of Sec.6.2.4. The characteristic time of the exponential temperature rise and the total temperature range spanned by the process are considerably different from the predicted ones in Fig.6.16. The resulting characteristic

time of the exponential equilibrium approach is $\tau \approx 1100\,\mathrm{s}$, that is an order of magnitude larger than the $\tau \approx 80\,\mathrm{s}$ estimate for $z_P = 2\,\mathrm{mm}$ wide teflon support.
In order to search for a signal with same order of magnitude characteristic time as the one predicted by numerical simulation, the attention was focused on the first few hundred seconds of measurements after the laser is turned on. A set of short-termed impulsive acquisition was performed in different input power and polarization conditions, an example of which is shown in Fig.7.4. A smaller-τ exponential temperature rise can be clearly identified in the first region of the acquisition, which is then overwhelmed by the large-τ signal of previous paragraph. The acquisitions were fitted with a model in which a small-τ exponential temperature rise is summed to a linear curve. The linearization of the long-τ exponential is justified as this acquisition inspect only a small fraction of the characteristic time of the slower signal:

$$T(t) = T_0 + k\left(1 - e^{-\frac{t}{\tau}}\right) + b\,t. \tag{7.1}$$

The characteristic time of the exponential temperature rise obtained from the fits of the different acquisitions were comparable. An estimate of the characteristic time of the exponential signal was obtained by averaging the fit results of different acquisitions: $\tau = 23 \pm 5\,\mathrm{s}$.

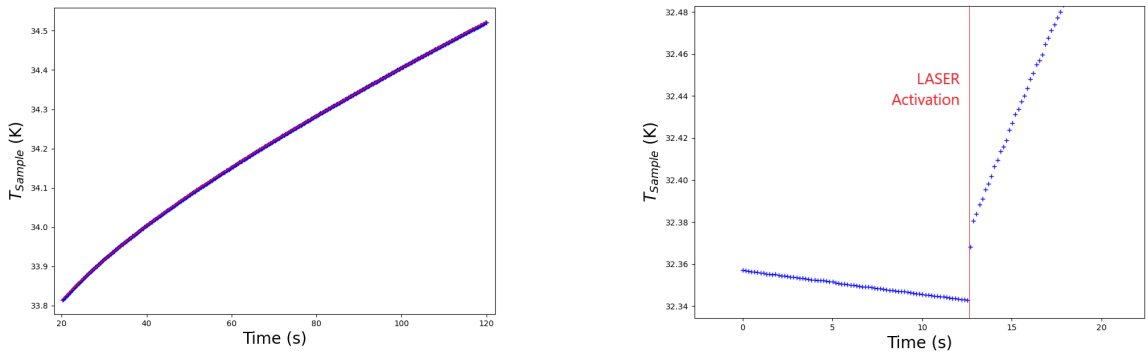

Figure 7.4: Left: Example of short-term impulsive acquisition ($P_{Las} = 2W$, $\lambda/2 = 183°$). The experimental data is fitted with Eq.7.1 model. Left: Close up view of a short-term impulsive acquisition in the temporal region where the laser is turned on. Before laser activation the sample temperature is slowly drifting due to $1/f$ noise. After laser activation the CX-1050-SD temperature exhibits a discontinuous variation, followed by the first portion of an exponential temperature rise.

There is actually a third independent body inside the chamber that exhibits a tempearature variation as a consequence of the power-up of the laser beam. The signal associated to the temperature variation of this third body is identifiable in the very first tenths of second of impulsive acquisitions. Fig.7.4 illustrates a close view of the temporal region in which the laser is switched on of an example impulsive acquisition. There is an evident discontinuity in the data when the laser is impulsively injected inside the cryogenic chamber. This characteristic discontinuity was not present in any other portion of the acquisition and several tests were conducted to investigate if this behaviour could be caused by a sistematic error in the read-out system, concluding that the observed behaviour at the start of the impulsive acquisitions is a physical signal. The signal is generated by a third indepentently heating body which has such a small characteristic time that its exponential temperature rise is not resolvable at the sampling frequency at wich the set of acquisition was performed. The third body has already reached thermal equilibrium after $O(0.1\,\mathrm{s})$ after the laser is switched on and as a result it is observed a discrete variation in the CX-1050-SD sensed temperature.

To further test the system in impulsive measurement conditions it was performed a set of input polarization varying acquisition. The linear slope coefficient b that was extracted from the Eq.7.1 fit of

the short term impulsive acquisitions is compared to the input polarization rotation angle $\theta_{\lambda/2}$. Fig.7.5 plot illustrates the experimental data distribution that was fitted with an offsetted Malus' Law model:

$$b(\theta_{\lambda/2}) = b_{min} + \left(k \sin\left(2(\theta_{\lambda/2} - \theta_{\lambda/2,0})\right)\right)^2 \tag{7.2}$$

Experimental data is in good agreement with the Malus' law model. Then first campaign impulsive measurement data indicates that there are three independent bodies with different characteristic times contributing to the signal that is sensed by the CX-1050-SD thermometer. Moreover the Malus' law distribution of the long-τ signal linearized slope already suggests that the dominant contribution in the system thermodynamics is linked to the excess reflection at sample input surface.

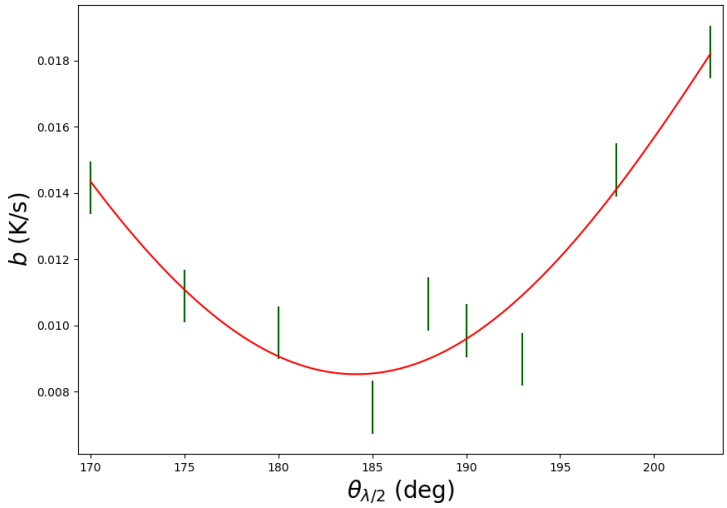

Figure 7.5: b coefficients extracted from Eq.7.1 fit to short-term impulsive acquisitions data against input polarization.

7.2.2 Modulation Calorimetry Measurement

Modulation Calorimetry optical absorption measurements were performed according to the following procedure. The system was cooled down to cryogenic temperatures and an ACC controled beam was injected through the sample; the current set point for the input beam was made equal to the average of the sinusoidal modulation; after steady-state input laser equilibrium was reached, beam power modulation was started on the automatized Labview control program (Sec.6.2.6); the PID system temperature set point was fixed to a value around which the heater could work at half of its maximum output power, to maximize its temperature stabilization ability; after few initial periods where the modulated temperature signal was left stabilizing, an $O(100\,\mathrm{s})$ data acquisition of both the sample temperature and the Keopsys laser internal powermeter was started. When power modulation on the input beam was started, the phase shift between temperaure and power oscillating signals was monitored to establish if the adiabatic regime condition was satisfied with the modulation parameter configuration in use. Despite extensive efforts the $\tan(\phi) > 10$ adiabatic regime condition could never be achieved in anyone of the tested configurations of the first acquisition campaign. In this section it will be illustrated in detail all the issues affecting experimental data that was acquired throughout the acquisitions of the first campaign, in which not only it was explored all the power modulation parameter space but also

the cryogenic chamber configuration was modified between the various set of acquisitions.

Starting from the basic configuration for the cryogenic chamber that was described in Sec.6.2.4, an ω_p-varying set of acquisition was performed to inspect the behaviour of the phase shift between the power and temperature signals as a function of the modulation frequency. During each acquisition both the sample temperature, measured by the CX-1050-SD thermometer, and the beam power at fiber output, measured by the Keopsys laser internal powermeter, were acquired. The acquired experimental data was processed according to the following procedure. The modulated power signal at fiber output was fitted with a sinusoidal model:

$$P_{Las}(t) = P_{0\,Las} + p_{Las}\sin(\omega_p t + \phi_p) \tag{7.3}$$

where $P_{0\,Las}$ is the offset of power modulation, p_{Las} the power modulation amplitude, ω_p the modulation frequency and ϕ_p is the arbitrary phase of the modulated signal at the starting interval of the acquisition. The fit was performed by means of a least squares minimization algorithm provided by the Scipy library in Phyton. Due to the non-linear nature of the fit, the algorithm convergence had to be aided by providing a set of adequate starting parameters, the automatized estimate of which relied on the analysis of the data distribution in the first period of the acquisition. After the power signal fit was completed, the oscillating sample temperature signal was fitted with the sum of a linear and sinusoidal model in which the modulation frequency was fixed to the ω_p value that was just extracted from the power modulation fit:

$$T_{Si}(t) = T_{0\,Si} + \Theta_0\sin(\omega_p t + \phi_t) + b\,t. \tag{7.4}$$

The linear component was added to the model to account for low frequency drifts around the equilibrium condition in the sample temperature signal[1]. The Θ_0 free parameter in the above model is the very same amplitude of sample temperature oscillations that will be inserted in the fundamental equation of Modulation Calorimetry (Eq.6.7) to obtain the concluding power absorption estimate. An example of a Modulation Calorimetry acquisition along with the least square fits to the power and temperature signals is shown in Fig.7.6.

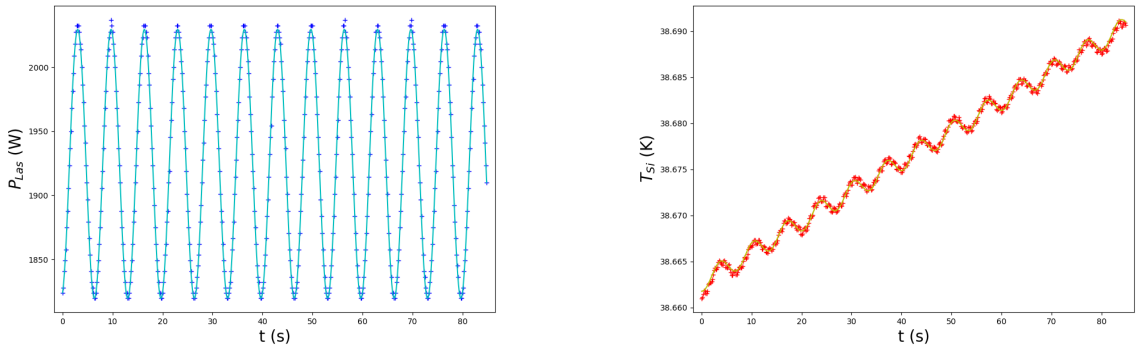

Figure 7.6: Example of Modulation Calorimetry measurement power (left) and temperature (right) signals.

The acquisition that is shown in the example figure is among the ones with the smallest modulation

[1]Low frequency drifts are caused by instabilities in the ACC controled output power and by cooling power oscillations. By computing the power density of the temperature fluctuations induced by this phenomena, it was found that the main noise contribution were located in the $f < 10^{-3}$ Hz region. As the characteristic time scale of such instabilities is much larger than the total duration of the modulated acquisition, the temperature drift linearization is justified.

$P_{0\,Las}$ (W)	p_{Las} (W)	ω_p (rad/s)	ϕ_P (rad)
1.9245 ± 0.0001	$1.049 \pm 0.002 \times 10^{-1}$	$9.4253 \pm 0.0006 \times 10^{-1}$	5.002 ± 0.004

T_0 (K)	Θ_0 (K)	ϕ_T (rad)	b (K/s)
38.6628 ± 0.0001	$1.04 \pm 0.02 \times 10^{-2}$	4.37 ± 0.02	$3.005 \pm 0.009 \times 10^{-4}$

Table 7.2: Fit parameters for Fig.7.6 data.

amplitude on the input power signal ($p_{Las} \approx 100\,\mathrm{mW}$). Nevertheless a sinusoidal oscillation is clearly distinguishable in the sample temperature signal. All the least squares fit converged without effort. The power modulation amplitude and frequency parameters are determined with sub-$\%$ uncertainty. A similar precision is achieved in the determination of the Θ_0 parameter, to which on average is associated a 2% relative error.
The phase retardation of the temperature signal respect to the power modulation signal is computed as $\phi = \phi_P - \phi_T$. The tangent of such phase shift angle is then computed to check the fullfillment of the adiabatic regime condition.

Analogously to Sec.7.2.1, it was performed a test to invesitgate the input polarization dependence of the Modulation Calorimetry signal. The ellipticity and orientation of the input beam polarization was varied between different modulated acquisitions with the used of the QWP-HWP system installed in front of the chamber input window.
This kind of acquisitions were performed in two tranches. For the first set of acquisitions only the HWP was installed before the chamber input window. A Modulation Calorimetry measurement of the sample temperature and fiber output laser power was performed for each tested value of the input polarization angle following the procedure that was illustrated at the start of the section.
Again, the observed $\Theta_0(\theta_{\lambda/2})$ data (Fig.7.7a) was fitted with an offseted Malus' law model:

$$\Theta_0(\theta_{\lambda/2}) = \Theta_{0\,min} + k \sin^2\big(2(\theta_{\lambda/2} - \theta_{\lambda/2,0})\big). \tag{7.5}$$

The $\Theta_{0\,min}$ offset accounts for the fact that, due to a depolarizing effect of the input window of the chamber, a portion of the input beam power is unavoidably s-polarized, causing a non-zero reflection even in the condition of Brewster angle alignment of the beam-sample system. After this first acquisition, the QWP was installed in the optical line in front of the HWP. An analogous set of acquisitions was performed by keeping fixed the orientation of the HWP and varying the QWP rotation angle. Also in this case the observed $\Theta_0(\theta_{\lambda/4})$ data (Fig.7.7b) was fitted with an offseted Malus' law model:

$$\Theta_0(\theta_{\lambda/4}) = \Theta_{0\,min} + k \sin^2\big(2(\theta_{\lambda/4} - \theta_{\lambda/4,0})\big). \tag{7.6}$$

Acquisition	$\Theta_{0\,min}$ (K)	k (K)	θ_0 (deg)
HWP	$8.0 \pm 0.1 \times 10^{-3}$	$4.3 \pm 0.2 \times 10^{-2}$	182.7 ± 0.3
QWP	$7.0 \pm 0.1 \times 10^{-3}$	$1.3 \pm 0.1 \times 10^{-2}$	23.9 ± 0.2

Table 7.3: Offsetted Malus' law model fit of Fig.7.7 data.

In both cases the experimental data is in good agreement with the ofsetted Malus' law model. All the

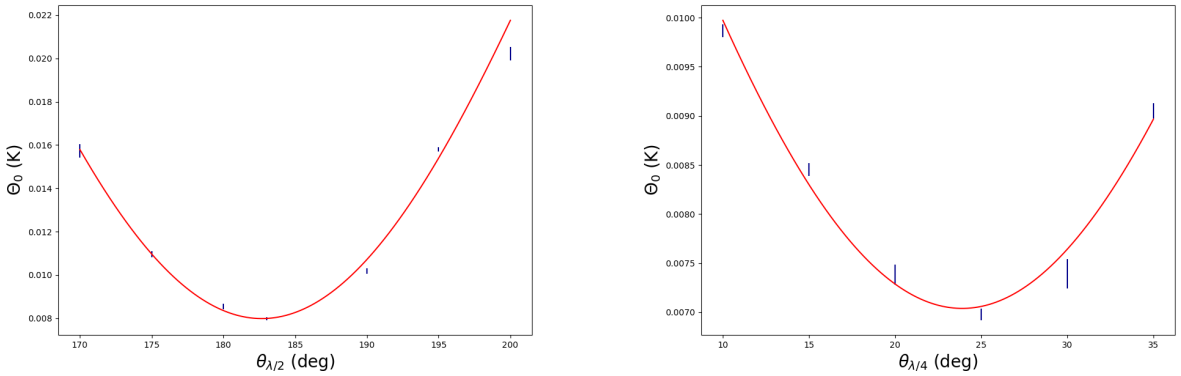

(a) (b)

Figure 7.7: First campaign input polarization varying acquisitions. Independent variables: a: HWP rotation angle; b: QWP rotation angle.

data points lie within 3σ uncertainty from the fitting curve. This result confirms the impulsive measurements findings on the input polarization dependence of the sample thermodynamics, suggesting that the dominant heat flow contribution in first campaign configurations is associated to the excess reflection at sample input surface.

Following this evidence for a reflection-dominated thermodynamics in the currently tested set up, a third polarization dependent analysis was performed to investigate over the depolarizing effect of the chamber input window. In this test both the QWP and HWP rotation angles were varied between different acquisitions. The QWP-HWP system would allow to actively compensate any non linear polarization that could be present in the beam at the chamber input, while allowing to also act on the polarization orientation. To this point, the chamber input window remains the only optical element between the QWP-HWP system and the sample. If the chamber window posseses a well defined birefringent nature, then the QWP-HWP system will be able to counteract the asymmetric phase retardation effect on the two orthogonal polarizations, consistently minimizing the residual portion of s-polarized beam that reaches the sample input surface. In this case, the oscillating temperature signal that is obtained after the minimization process would be at first approximation independent from variations in the input polarization. If instead the window induces an unknown depolarization on the input beam the insertion of the QWP will have no significant effect on the reduction of the excess s-polarized reflected power, so that the resulting Θ_0 distribution would still follow a Malus' law with similar parameters to the one found in the analysis of the previous paragraph.
The test acquisition in the aforementioned configuration was performed in the following way. At first, the HWP rotation angle was fixed to a given value, close to the reflection minimization angle that was found in the previous paragraph ($\theta_{\lambda/2,\,0} \approx 183°$). For each HWP orientation, the QWP was rotated to different angles on its mount. At each different QWP orientation a $O(100\,\mathrm{s})$ Modulation Calorimetry acquisition was performed with parameters $p = 1.080 \pm 0.002\,\mathrm{W}$, $\omega_p = 0.3142 \pm 0.0001\,\mathrm{rad/s}$. The modulated acquisitions were fitted with the usual procedure to extract the Θ_0 parameter from sample temperature signal. Then, Eq.7.6 model was fitted to the such obtained $\Theta_0(\theta_{\lambda/4})$ data to extract the minimum achievable amplitude of sample temperature oscillations $\Theta_{0\,min}$ at a given HWP orientation. The same process was replicated for different HWP orientations.

The resulting set of $\Theta_{0\,min}$ as a function of the HWP rotation angle $\theta_{\lambda/2}$ is shown in Fig.7.8. The experimental data was fitted with an offsetted Malus' law model analogous to the one in Eq.7.5. The experimental data exhibit good agreement with the fitting model. In addition, the insertion of the

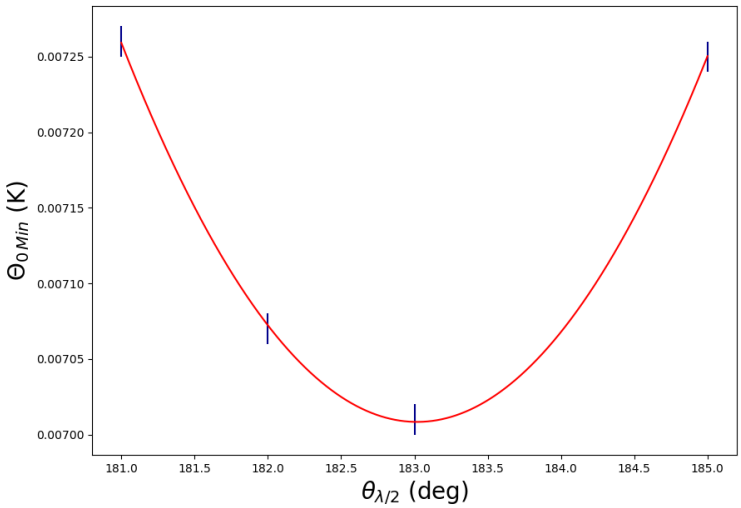

Figure 7.8: Minimum temperature oscillation amplitude that was achievable by tuning the QWP+HWP system as a function of the HWP rotation angle.

$\Theta_{0\,min}$ (K)	k (K)	θ_0 (deg)
$7.002.0 \pm 0.002 \times 10^{-3}$	$5.21 \pm 0.06 \times 10^{-2}$	183.022 ± 0.007

Table 7.4: Offsetted Malus' law model fit of $\Theta_{0\,min}(\theta_{\lambda/2})$ data (Fig.7.8).

QWP allowed for a mere $\sim 10\%$ reduction of the smallest achievable amplitude of temperature oscillations compared to the HWP only case. Then, according to the discussion of the former paragraph, this evidence supports the hypotesis by which the chamber input window is inducing an unknown depolarizing effect on the transmitted laser beam.

7.2.3 Discussion of First Measurement Campaign

Starting the discussion over the results of first campaign acquisitions from impulsive measurements, it is of primary importance to identify which is the portion of the cryogenic chamber system to which each one of the three observed exponential signals is linked to. To this purpose an updated set of numerical simulations was carried out to better understand the system thermodynamics in impulsive measurement conditions. The thermodynamical simulations that were developed in Sec.6.2.4 must be updated by extracting from the newly available data an empirical estimate for the A_c and A_{eff} quantities in Eq.6.14 and Eq.6.15 respectively. This quantities were initially computed with purely geometrical considerations but a more realistic model is required: an effective expression for the contact area in the conduction heat contribution must include an attenuation factor that accounts for non ideal coupling between different materials and bodies[2] ($A_c = \mu A_c^{geom}$); the computation of the effective area for the radiation contribution should instead include an attenuation factor that accounts for non-

[2]In the final configuration there are three different interfaces between the Silicon crystal and the temperature stabilized copper: the silicon sample is directly placed on its housing pocket in the teflon rotary support; the teflon rotary support is in direct contact with a copper cylinder of same diameter; the small copper cylinder is coupled to the main copper support by means of an indium foil. The coupling between the various interfaces is ensured by the compressive action excerted by the springs on the upper part of the teflon support system, that were primarily employed to press the CX-1050-SD thermometer against the silicon sample.

ideal emissivity of the sample and shield surfaces ($A_{eff} = \epsilon A_{eff}^{geom}$). For this reason, the A_c and A_{eff} quantities are the biggest source of error in the previously developed simulations.
The laser-off equilibrium equation that is obtained by equating the conduction (Eq.6.14) and radiation (Eq.6.15) heat flow contributions can be rearranged to isolate the ratio of the two aforementioned quantities:

$$r_{c/r} = \frac{A_c}{A_eff} = \frac{\sigma z_P}{k_P} \frac{T_{Sh}^4 - T_{Si}^4}{T_{Si} - T_{Cu}} \tag{7.7}$$

By inserting the laser-off equilibrium temperatures of the three bodies under analysis in the above equation it is obtained an empirical estimate of the A_c versus A_{eff} ratio, that is proportional to the ratio of the conduction and radiation attenuation coefficients ($r_{c/r} = \frac{\mu}{\epsilon} A_c^{geom}/A_{eff}^{geom}$). During the first measurement campaign, the laser-off equilibrium temperatures were only extracted by averaging the first seconds of the impulsive acquisitions, before the laser activation instant.
The sample, shield and copper support temperatures in laser-off equilibrium conditions were respectively measured to be $T_{Si} \approx 30.9\,\mathrm{K}$, $T_{Sh} \approx 64.9\,\mathrm{K}$, $T_{Cu} \approx 13.2\,\mathrm{K}$. Inserting this values in Eq.7.7, the empirical estimate of the A_c/A_{eff} ratio is obtained: $r_{c/r} = 3.8 \pm 0.2 \times 10^{-4}$. This notion should then guide the individual estimate for the A_c and A_{eff} values.
It should be noted at first that the emprical $r_{c/r}$ value differs considerably from the one of the geometrical modelization: $r_{c/r} \approx 3.8 \times 10^{-2}\, A_c^{geom}/A_{eff}^{geom}$. To this point there are no other avilable informations to decouple the two contributions to the $r_{c/r}$ value, so that it is necessary to perform a new educated guess for the A_c and A_{eff} values, keeping the empirical constraint on their ratio. In the following paragraph will be analyzed the two extreme cases to gain a qualitative understandment of the thermodynamics of the system. In the first case the conduction effective contact area A_c is approximately equal to its geometrically computed value while the effective area for radiation heat flow is much larger than its expected value ($\mu_1 \approx 1$; $\epsilon_1 = \frac{1}{r_{c/r}} A_{eff}^{geom}/A_c^{geom} \approx 260$). To realize this configuration of the two surface values it is necessary to drop the concentric spheres modelization for the sample and shield surfaces when computing the heat flow contribution. In the second case instead it is the radiation effective area to be the correctly estimated one by the geometrical model while the expected contact area for conduction is largely overestimated respect to the real case ($\mu_2 = r_{c/r}\, A_{eff}^{geom}/A_c^{geom} \approx 3.8 \times 10^{-2}$; $\epsilon_2 = 1$). This second configuration corresponds to the case of an high thermal resistance between silicon crystal and copper support due to non-ideality in the contact surfaces between different parts of the support system.

It was then performed an independent numerical simulation of impulsive measurement thermodynamics in each one of the two aformentioned cases. A comparison between $\tau(\alpha_{Si})$ curves obtained from the two different simulations is shown in Fig.7.9. The simulations examined the expected silicon absorption coefficient range based on previous literature estimates. The results of the simulation cannot help to identify the nature of the two signal with larger characteristic time that were observed in impulsive measurements during the first acquisition campaign: the characteristic times obtained from the $\mu \approx 1$ simulations are order of magnitude compatible with the ones of the faster sub-dominant signal of Fig.7.4 ($\tau_{expm} \approx 25\,\mathrm{s}$, $\tau_{sim} \approx 50\,\mathrm{s}$); the characteristic times obtained from the $\epsilon \approx 1$ simulations are instead order of magnitude compatible with the slower dominant signal in short-termed impulsive acquisitions($\tau_{expm} \approx 1000\,\mathrm{s}$, $\tau_{sim} \approx 1500\,\mathrm{s}$). Further evidence must be collected to understand which body is sourcing each one of the two signals so that the discussion is postponed to Sec.7.3, where the second campaign acquisitions are presented.

Turning the attention to Modulation Calorimetry acquisitions, the distribution of the phase retardation and amplitude of sample temperature oscillations as a function of the modulation frequency must be analyzed in detail. The ω_p-dependent behaviour of the $\tan(\phi)$ quantity is shown in the left part of Fig.7.10. The observed phase shift behaviour is incompatible with the theoretical expectation of

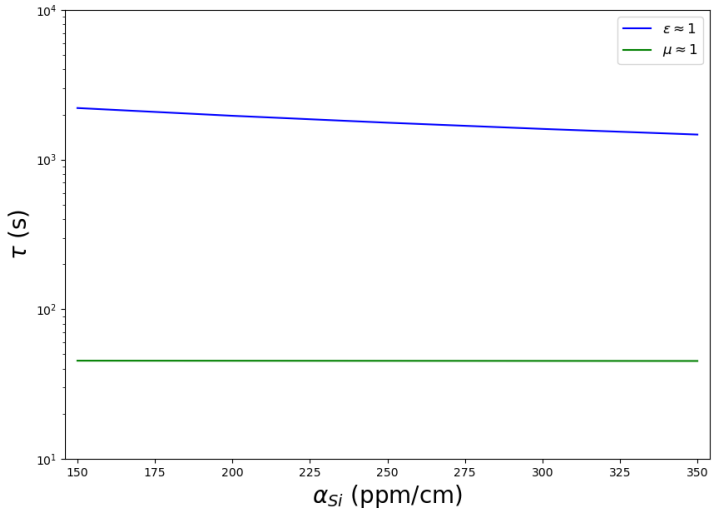

Figure 7.9: Comparison between $\tau(\alpha_{Si})$ curves obtained from simulations run with different estimates of the effective values of the conduction and radiation area. Green: $A_c = 10^{-5}\,\mathrm{m}^2$, $A_{eff} = 2.6 \times 10^{-1}$; Blue: $A_c = 3.8 \times 10^{-7}\,\mathrm{m}^2$, $A_{eff} = 10^{-3}\,\mathrm{m}^2$.

Eq.6.6, namely a linear proportionality between the quantities under analysis. In fact an inverse proportionality between the phase retardation of the temperature variation in respect to a change in the input power and the modulation frequency of the varying heat flow contribution cannot be explained with any physical process related to a single-body system[3]. In order to properly describe the observed phase shift between the two signals is required a model that accounts for the combined response of two thermodinamically coupled bodies responding to input power oscillations.

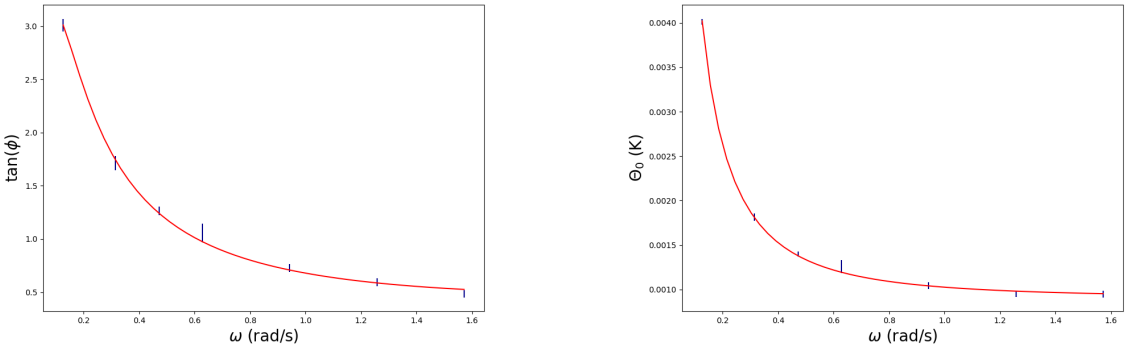

Figure 7.10: Example $\tan(\phi)$ and Θ_0 data obtained from ω_p-varying acquisitions. Experimental data is fitted with a model consisting of the superposition of two equal frequency and ω_p-dependent amplitude sinewaves (Eq.7.8).

[3]In any case the thermodynamical response of a body to a modulated input power excitation is analogous to the action of a low-pass filter. In the low frequency range the system is always able to thermalize within a fraction of the modulation period; the temperature signal is able to follow the power input with null phase retardation and the amplitude of the induced temperature variation is frequency independent. When the modulation frequency exceeds the characteristic frequency of the system the power variations happen too fast for the system to thermalize; the temperature variation response signal acquires a phase shift which eventually approaches $\phi = \pi/2$ and the temperature oscillation amplitude is heavily attenuated.

Data Set	k_1 (K/s)	k_2 (K/s)	j_1 (rad/s)	j_2 (rad/s)
$\tan(\phi)$	$8.82 \pm 0.03 \times 10^{-3}$	$4.8 \pm 0.1 \times 10^{-4}$	10.7 ± 3.0	$1.5 \pm 0.1 \times 10^{-2}$
Θ_0	$4.6 \pm 3.0 \times 10^{-3}$	$4.81 \pm 0.05 \times 10^{-4}$	5.5 ± 4.0	$3.0 \pm 2.0 \times 10^{-2}$

Table 7.5: Fit parameters extracted from the independent fit of $\tan(\phi)$ and Θ_0 in ω_p-dependent data acquisitions with the two sinewave model of Eq.7.8 and Eq.7.9.

The two bodies are characterized by a different responsivity to input power fluctuations. The first body, that will be referred as 'fast', has a fast responsivity to input power variations. Recalling Eq.6.6b, the fast responsitivity of the first body is provided either by a small thermal capacitance $C = mc_p$ or by a large thermal coupling with the outer environment, which is quantified by the linearized heat exchange coefficient Q'. Then, the fast body is operated at much lower frequencies than its characteristic cut-off frequency and it generates a constant-amplitude null-phase signal across all the tested range of modulation frequencies. The approximately constant amplitude of the signal can be understood by noticing that the fast body is operated far from the adiabatic regime so that Q' is the dominant contribution in Eq.6.6a. The second body, that will be referred as 'slow', has a low responsivity to input power variations. That is, the second body has a much larger capacitance than the first one, united to a smaller thermal coupling with the outside environment. The slower body is operated near its adiabatic regime region, so that the amplitude of its oscillating temperature response is almost proportional to $1/\omega_p$ and the tangent of its phase retardation is linear respect to the input power modulation frequency.
As the two bodies are thermally coupled, the CX-1050-SD will sense the sum of the two signals. The temperature response of each body exhibits a sinusoidal oscillation with equal frequency, so that the resulting signal can be obtained analitically:

$$\begin{aligned} T(t) - T_0 =& A\sin(\omega_p t + \gamma) + B\sin(\omega_p t + \delta) = \\ =& \Big[\big(A\cos(\gamma) + B\cos(\delta)\big)^2 + \big(A\sin(\gamma) + B\sin(\delta)\big)^2\Big]^{1/2} \\ & \sin\Big(\omega_p t + \tan^{-1}\big(\frac{A\sin(\gamma) + B\sin(\delta)}{A\cos(\gamma) + B\cos(\delta)}\big)\Big) = \\ =& \Theta_0 \sin(\omega_p t + \phi). \end{aligned} \tag{7.8}$$

In the above expression the phase of the input power modulated signal has been fixed to $\phi_P = 0$, so that the total phase shift is directly obtained by computing the temperature signal phase. As explained in the previous paragraph, the amplitude and phases of both temperature signals are described by Modulation Calorimetry equations:

$$\begin{aligned} A &= \frac{p_A}{\sqrt{m_A^2 c_{p\,A}^2 \omega_p^2 + Q_A'^2}} = \frac{k_A}{\sqrt{\omega_p^2 + j_A^2}} \\ \gamma &= \tan^{-1}\left(\frac{m_A c_{p\,A}\omega_p}{Q'_A}\right) = \tan^{-1}\left(\frac{\omega_p}{j_A}\right) \\ B &= \frac{p_B}{\sqrt{m_B^2 c_{p\,B}^2 \omega_p^2 + Q_B'^2}} = \frac{k_B}{\sqrt{\omega_p^2 + j_B^2}} \\ \delta &= \tan^{-1}\left(\frac{m_B c_{p\,B}\omega_p}{Q'_B}\right) = \tan^{-1}\left(\frac{\omega_p}{j_B}\right). \end{aligned} \tag{7.9}$$

Typical $\tan(\phi)$ and Θ_0 data obtained from ω_p-varying acquisitions during the first measurement campaign is shown in Fig.7.10. The $\tan(\phi)$ and Θ_0 data has been independently fitted with the analitical expression obtained by combining Eq.7.8 and Eq.7.9. All the four free parameters that were extracted

from the $\tan(\phi)$ fit are 1σ compatible with the corresponding parameters extracted from the independent Θ_0 fit. The fact that both data sets are excellently fitted by the analitical equations and that the characteristic parameters describing the two underlining signals match up to 1σ accuracy validate the model that was outlined throughout this paragraph. Aniway, the independent bodies that are sourcing the two sinewaves of the aforementioned model still cannot be identified, due to to large uncertainities in the amplitude and phase parameters that were extracted from the fit (Tab.7.5) due to scarcity of experimental data points. Also the discussion over signal identification in modulated acquisitions will then be posponed to Sec.7.3.

Thereby the only notion that could be confidently extracted from first measurement acquisition is the fact that the dominating heat flow contribution in both impulsive and modulated measurements is associated to the polarization dependent excess reflection on the sample input surface. The magnitude of the contribution that is sourced by the excess reflected power compared to the optical absorption driven contribution in the sample can be better understood by looking at Modulation Calorimetry measurements.
To this purpose it will be developed a model describing the response of the system to a change in the input polarization orientation in the case that optical absorption is the leading contribution to the sample thermodnamics. Then it will be performed a comparison between the fits to the polarization varying data of this absorption driven model and the Malus' law reflection dominated model.
Tha absorption driven model works under the assumption that the input beam is linearly polarized and that the sample is placed exactly at Brewster angle Θ_B respect to the beam axis. As already proven, only the second assumption is realistic in the currently tested experimental set up. Assuming also that crystalline Silicon optical absorption is polarization independent, it is possible to split the s and p polarization contributions and treat them in equal fashion. The polarization distribution of the beam power follows Malus' law:

$$\begin{aligned} P_p(\theta) =& P_{Las}\cos^2\left(2(\theta_{\lambda/2}-\theta_{\lambda/2,0})\right) \\ P_s(\theta) =& P_{Las}\sin^2\left(2(\theta_{\lambda/2}-\theta_{\lambda/2,0})\right) \end{aligned} \tag{7.10}$$

where θ_0 is the usual rotation angle of the HWP mount for which it is transmitted a purely p-polarized beam. The two components interact differently with the sample input surface. The p-polarized portion of the beam gets fully transmitted, being the sample placed at Brewster angle respect to the beam, and eventually it gets linearly absorbed inside the sample. The optical path of the beam inside the sample can be computed by estimating the transmission angle at Brewster angle for a vacuum-silicon system with the use of Snell's law. The reference refractive index value for crystalline Silicon at cryogenic temperatures for $\lambda = 1550\,\mathrm{nm}$ light is taken from [61]: $n_{Si} = 3.453$. Namely, it results that the incidence angle is $\theta_i = \theta_B = \tan^{-1}(n_{Si}) \approx 73.85^\circ \approx 1.29\,\mathrm{rad}$ and the transmission angle is $\theta_t = \sin^{-1}\left(\sin(\theta_i)/n_{Si}\right) \approx 16.15^\circ \approx 0.28\,\mathrm{rad}$. Then, recalling that the sample is entered by the beam on its wider lateral face, so that the $l_x = 1\,\mathrm{cm}$ side of the parallelepiped is orthogonal to the input surface, the fraction of p-polarized optical power that gets absorbed in the Silicon crystal is simply given by:

$$P_{In,p}(\theta_{\lambda/2}) = \frac{P_p(\theta_{\lambda/2})\alpha_{Si} l_x}{\cos(\theta_t)}. \tag{7.11}$$

The same argument of linear absorption is valid for the s-polarized component, which is instead partly transmitted and partly reflected. The transmittance and reflectance values for s-polarized $\lambda = 1550\,\mathrm{nm}$ light in Silicon at cryogenic temperatures are given from Fresnel equations:

$$R_s = \left(\frac{n_{vac}\cos(\theta_i) - n_{Si}\cos(\theta_t)}{n_{vac}\cos(\theta_i) + n_{Si}\cos(\theta_t)}\right)^2 \approx 0.714 \tag{7.12}$$

and the complementary $T_s = 1 - R_s \approx 0.286$. The larger portion of s-polarized optical power gets reflected at the sample input surface, non contributing to the optical absorption related heat flow in the

crystal. The transmitted part of the s-polarized beam gets linearly absorbed until it reaches the sample output surface, where the first internal refraction happens. In this case, a non negligible portion of the s-polarized transmitted beam gets reflected at the sample output surface, covering an additional $l_x/\cos(\theta_i)$ distance towards the sample input surface and contributing to the optical absorption heat flow. Due to the fact that optical absortion contribution that comes from multiple internal reflections fastly converges thanks to the R_s attenuation factor for at each subsequent reflection, as a first approximation it is sufficient to consider the contribution of an infinite series of internal reflections:

$$P_{In,\,s}(\theta_{\lambda/2}) = \frac{T_s P_s(\theta_{\lambda/2})\alpha_{Si} l_x}{\cos(\theta_t)} \sum_{n=0}^{\infty} R_s^n = \frac{T_s P_s(\theta_{\lambda/2})\alpha_{Si} l_x}{\cos(\theta_t)} \frac{1}{1-R_s} \tag{7.13}$$

where it was computed the geometric series limit in the $|R_s| < 1$ case. Then the total absorbed power for a linearly polarized input beam in a Silicon sample that is oriented at Brewster angle respect to the beam axis as a function of the polarization orientation is given by the putting together the polarized contributions Eq.7.11 and Eq.7.13:

$$P_{In}(\theta_{\lambda/2}) = \frac{P_{Las}\alpha_{Si} l_x}{\cos(\theta_t)} \left[\cos^2\left(2(\theta_{\lambda/2} - \theta_{\lambda/2,0})\right) + T_s \sin^2\left(2(\theta_{\lambda/2} - \theta_{\lambda/2,0})\right) \frac{1}{1-R_s} \right] \tag{7.14}$$

Then, as the amplitude of temperature oscillations in Modulation Calorimetry measurements is directly proportional to the optical absorption, if the experimental set up is providing an accurate estimate of the optical absorption in Silicon crystal, a similar pattern to the one in Eq.7.14 is expected to manifest in input polarization varying acquisitions.

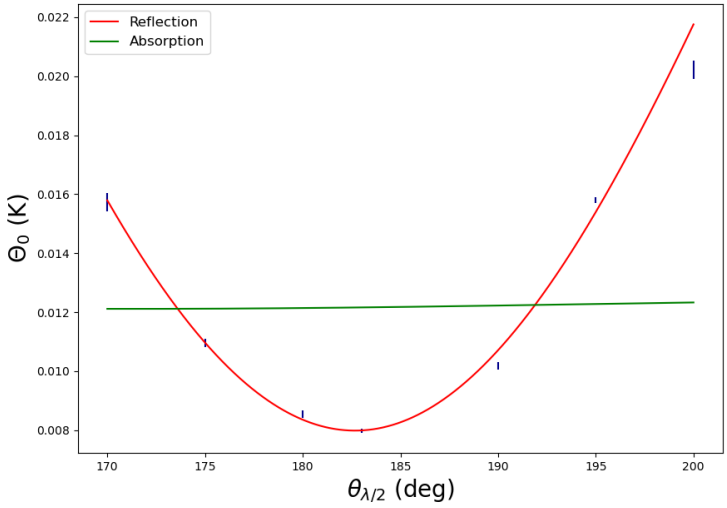

Figure 7.11: Comparison of different models fitted to the $\Theta_0(\theta_{\lambda/2})$ data. Red curve: excess reflection driven model, Eq.7.5; Green curve: optical absorption dominated model, Eq.7.14.

Fig.7.11 illustrates a comparison between the reflection and absorption driven models that were outlined in the course of this section to describe the sample thermodynamics as a function of the input beam polarization angle. The Eq.7.5 model, where the input beam polarization is non linear and the excess reflected power contribution dominates the system thermodynamics, was used to fit the experimental data (red curve). The model is in good agreement with the experimental findings as all the data points are compatible with the fitting curve within 3σ accuracy. It was not possible instead to converge on a meaningful set of parameters in the case of the Eq.7.14 fit, associated to the model where the input

beam was assumed as linearly polarized and optical apsorption is the leading heat flow contribution on the sample.
All this evidence further validate the hypotesis according to which, in the experimental set up of first campaign acquisitions, the reflected power induced effects are dominating the system thermodynamics even in Modulation Calorimetry conditions, making it impossible to perform an accurate estimate of crystalline Silicon optical absorption.

7.3 Second Acquisition Campaign

A second acquisition campaign was attempted in an effort to adress the excess reflection issue that spoiled the first acquisitions. In the previous section it was determined that the thermodynamics of the system are dominated by the excess input power associated with the reflection of the s-polarized component of the laser beam, which is caused by a depolarizing effect of the flange soldered input window of the cryogenic chamber. The excess reflection contribution cannot be lowered below $O(10\%)$ of the total power due to an impossibility to place a polarizing system inside the cryogenic chamber. As a consequence, the easiest option that was viable to minimize the unwanted heat flow contribution was to recycle the set of mirrors that was designed in Sec.6.2.4 to be placed on the copper support optical plane. The mounting system of this two mirrors was initially designed to steer the transmitted beam towards the chamber output window but it can be rearranged to control the reflected beam optical path.

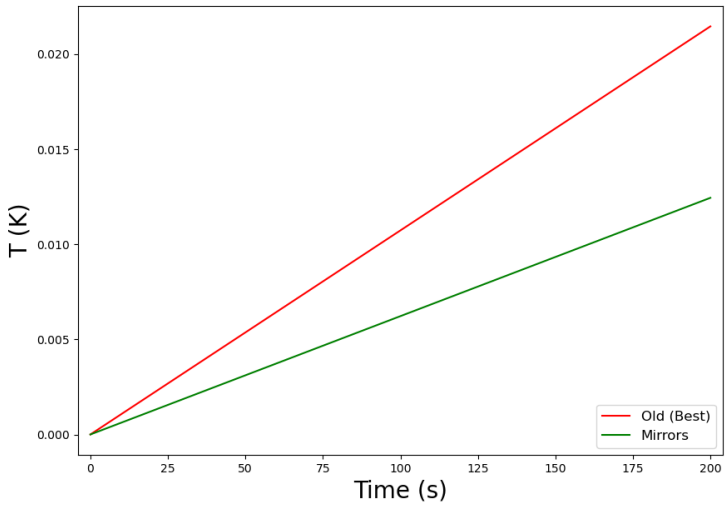

Figure 7.12: Comparison of room temperature impulsive measurement tests performed in different system configurations. Red: First campaign best configuration. Green: Second campaign configuration.

The major constraint on the placement of the mirrors on the copper support optical plane is imposed by the fact that the transmitted portion of the beam must be able to travel freely towards the chamber output window. This in fact prohibits a complete evacuation of the reflected beam: the last mirror must be placed in an offsetted position respect to the chamber optical axis; this way, due to the very limited space inside the cryogenic chamber the exiting beam has null view angle of the output window and its forced to impinge on the optical tunnel inner surface. This contact with the tunnel surface causes the reflected bem to partially diffuse. Due to the large incidence angle of the beam on the tunnel surface,

Fit parameter	Old Configuration	New Configuration
$b\,(\mathrm{K/s})$	$1.1 \pm 0.1 \times 10^{-4}$	$6.2 \pm 0.5 \times 10^{-5}$

Table 7.6: Linear proportionality coefficient of the room temperature impulsive test acquistions. Fit model: $\Delta T(t) = a + b\,t$.

the majority of the optical power in the reflected beam will still be able to output from the chamber window at the end of the tunnel. A small fraction of the reflected power will instead be diffused back inside the radiation shield. It is then necessary to quantify the residual heat flow contribution of diffused light in the chamber in order to understand if it will remain the dominant contribution for the sample thermodynamics. A schematic view of the optical system configuration inside the cryogenic chamber during the second acquisition campaign can be seen in Fig.7.1c.
Fig.7.12 illustrates a comparison between the room temperature test that were performed previously to the cooling of the system in different optical configurations employed in the first and second acquisition campaign. Again, the test consisted in shining a $4\,\mathrm{W}$ beam on the sample surface at Brewster Angle and ambient temperature and pressure. An $O(100\,\mathrm{s})$ acquisition of the sample temperature is performed and fitted with a simple linear model. The slope of different sample temperature fits are compared: under the hypotesis that the chamber thermodynamics are dominated by the effect of the excess contribution, a less steep temperature rise slope indicates a reduction in the excess reflection contribution. It can be clearly seen as the new configuration where the mirrors are employed to steer the reflection outside from the radiation shield performs significantly better respect to the best one among the first campaign configurations. The fit parameters indicates a factor 2 decrease in the sample temperature slope. It can be expected that this will translate in at least a factor 2 improvement in the system sensitivity to the excess reflection contribution, as the observed sample signal is eventually made up of a reflection induced contribution summed to an acquisition driven signal.

Heater-Only Acquisitions

In order to obtain a better understanding of the system thermodynamics in impulsive measurement conditions it was conducted a preliminary analysis before turning on the laser beam in cryogenic environment. The system was cooled down until it reached its limit equilibrium temperature. The laser-off, heater-off equilibrium temperature of the sample, shield and copper support were recorded. Starting from this condition, a temperature step ΔT was applied to the copper support by means of the PID controlled heater. An $O(1\,\mathrm{h})$ acquisition of the signals of the three thermometers was performed so that it was possible to run an accurate fit of the long-τ exponential rise observed in the sample temperature signal. It was possible to perform only two of such acquisitions with different PID setpoints due to limited availability of cryocooler operation time. An example of the evolution of the three temperature signal during this kind of acquisition is shown in Fig.7.13. The acquisitions were fitted with the usual exponential temperature rise model of Eq.6.20. The hour long acquisition is sufficient to perform an $O(\%)$ accurate fit of the temperature rise signals.
This test eventually allows to obtain a more accurate and precise estimate of the A_c/A_{eff} ratio respect to the one that was directly derived from impulsive measurement acquisitions during the first campaign. The exponential fits of the sample and shield temperature signals can be used to extract the new equilibrium temperatures of the system. From each different equilibrium condition, associated to a different PID setpoint, it is possible to obtain an independent estimate of $r_{c/r}$ following the same reasoning of Sec.7.2. The three independent estimates are compared in Fig.7.14, by plotting them against the copper support stabilization temperature. The three obtained $r_{c/r}$ values are 1σ compatible with each other, confirming the goodness of the derivation. Then, the A_c/A_{eff} ratio of

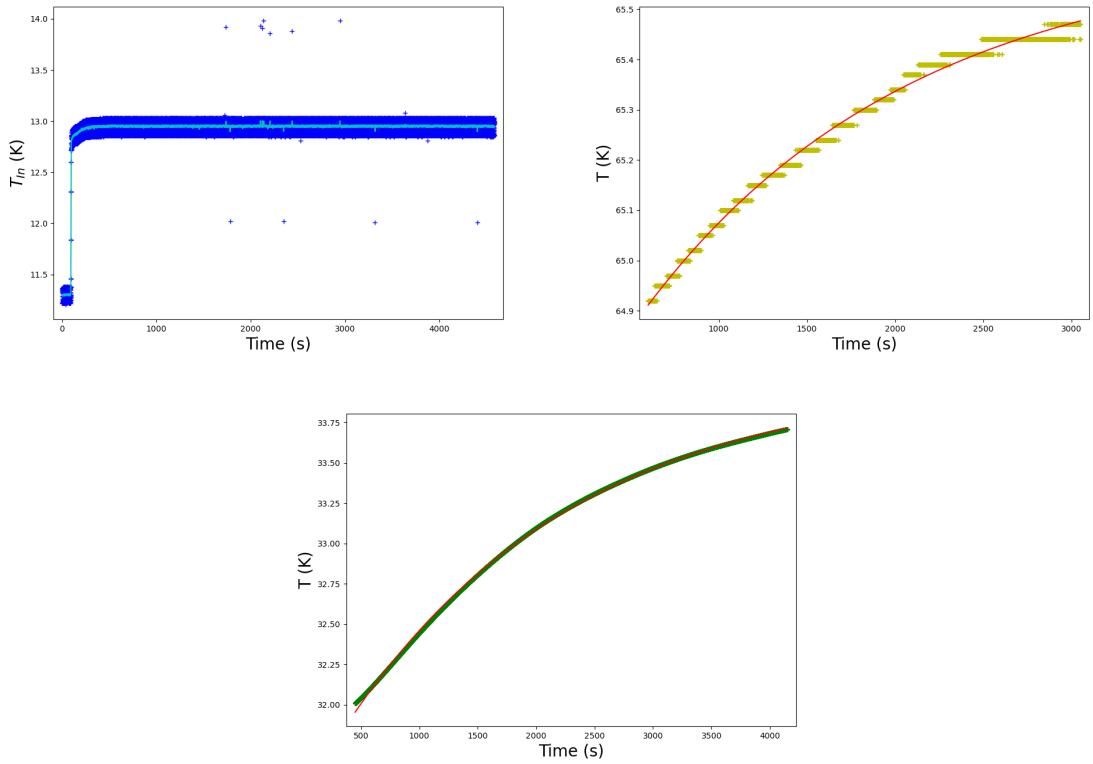

Figure 7.13: Example signals acquired during PID heating tests. Upper left: copper support. Light blue line shows a moving average of the in-loop temperature data.; Upper right: shield; Lower: sample. The red lines shows an exponential model fits to the temperature rise data.

the system in this new configuration can be taken as the average of the three independent estimates: $r_{c/r} = 4.63 \pm 0.06 \times 10^{-4}$.

Impulsive Measurements

During second acquistion campaign impulsive measurement were performed with the same procedure that was illustrated in Sec.7.2, except for the fact that more care was placed in waiting for the system to cool back down to equilibrium after each acquisition. In addition, all the impulsive acquisition had a minimum duration of $2\,\mathrm{h}$, in order to allow for sub-$\%$ accurate fitting of the large characteristic time signal recorded by the CX-1050-SD thermometer.
At first, an input polarization varying set of impulsive acquisitions was performed to investigate if the installation of the mirrors succeded in reducing the reflected power contribution to the sample signal. The HWP was installed in front of the chamber input window and the output optical power from laser fiber was set to $P_{Out} = 2.04 \pm 0.05\,\mathrm{W}$. The optical isolator system was set in transmission maximization configuration ($T_{FI} = 0.97$) so that the optical power that reached the sample input surface was $P_{Las} = 1.98 \pm 0.05\,\mathrm{W}$.
The copper support temperature was stabilized at the same value throughout all the different acquisitions of the second campaign ($T_{Cu} = 13.45 \pm 0.5\,\mathrm{K}$). All the temperature signals sensed by the three thermometers were registered during impulsive acquisitions.
Each CX-1050-SD acquisition was fitted with the exponential temperature rise model of Eq.6.20. The initial equilibrium temperature parameter was set to a fixed value of $T_{Si,0} = 31.7 \pm 0.1\,\mathrm{K}$ in all the different sample temperature fits, while all the other variables are left as free parameters. The same procedure was made on the shield temperature data. Also this signal exhibited an exponential rise due to the fact that the radiation shield temperature is not actively stabilized. The initial equilibrium

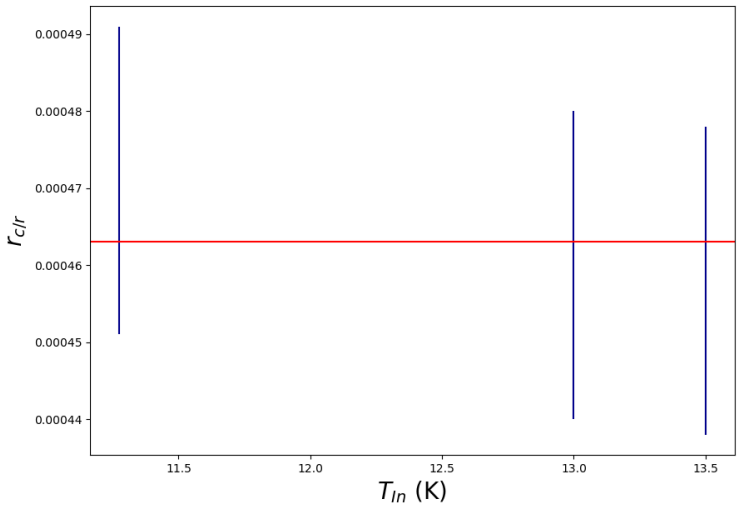

Figure 7.14: Comparison of A_c/A_{eff} ratio estimates obtained from different heater-only acquisitions.

temperature of the radiation shield was set to $T_{Sh,\,0} = 65.75 \pm 0.15\,\mathrm{K}$. The two former equilibrium vaules for the sample and shield temperature were obtained from the heater-only acquisition data that was analyzed in the previous section.

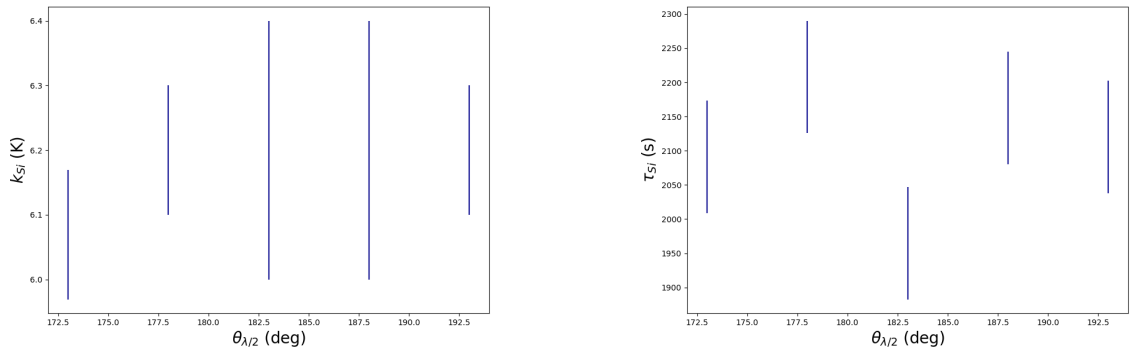

Figure 7.15: Fit parameters extracted from input polarization varying acquisitions of the silicon sample temperature.

The results of the k and τ parameters that were extracted from sample and shield temperature signal fits as a function of the $\theta_{\lambda/2}$ polarization orientation angle are presented in Fig.7.15 and Fig.7.16 respectively. Again, by extracting the characteristic time of the sample or shield signal and comparing them between different acquisitions, all the values are 1σ compatible with each other. The average values of the characteristic time of the two signals are $\tau_{Si} = 2.11 \pm 0.08 \times 10^3\,\mathrm{s}$, $\tau_{Sh} = 1.39 \pm 0.06 \times 10^3$. When considering the k parameters there is instead a considerable difference respect to the polarization orientation dependent behaviour that was observed in the acquisitions of the first campaign (Fig.7.5). The total excursion of the exponential temperature rise does not exhibit a Malus' law proportionality respect to the HWP rotation angle. This already indicates that the reflection steering mirror installation has produced a noticeable effect on the system thermodynamics. The $\theta_{\lambda/2}$-independent distribution of the exponential temperature rise amplitude can be explained in the framework of a reduced excess

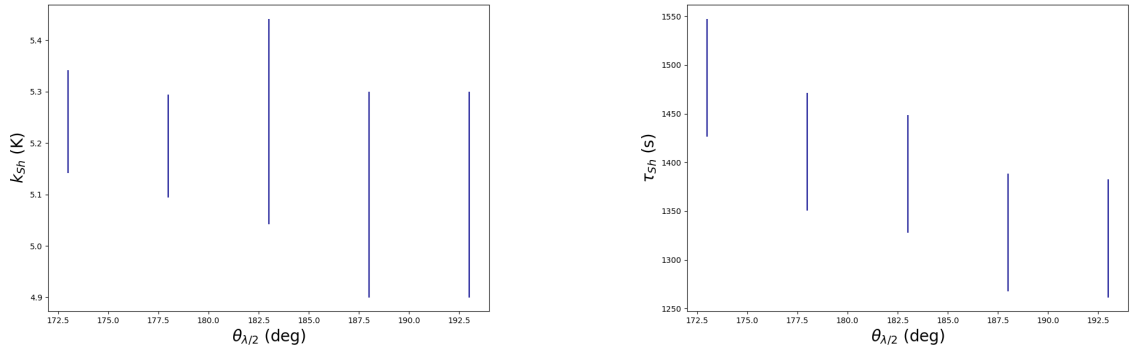

Figure 7.16: Fit parameters extracted from input polarization varying acquisitions of the shield sample temperature.

reflection contribution to the system thermodynamics. This hypotesis will be analyzed in more detail in the Modulation Calorimetry section, as this kind of measurement resulted to be more sensitive to variations in the input polarization.

Anyway, this is not the only noticeable effect induced by the reflection steering mirrors on impulsive measurement signals. Fig.7.17 shows a close up view of an example long-term acquisition in the first few hundred of seconds after the laser was switched on (left) and also a closer zoom of the signal near the laser activation instant (right). This example signal can be qualitatively compared to the one observed in short-term acquisitions during the first campaing (Fig.7.4). The subdominant exponential signal with $\tau \approx 25\,\mathrm{s}$ that was identified in all first campaign acquistions has now vanished. In agreement with the evidence of the previous paragraph, the $\tau \approx 25\,\mathrm{s}$ signal that was observed in first campaign acquistion can be linked to the excess reflected power contribution.

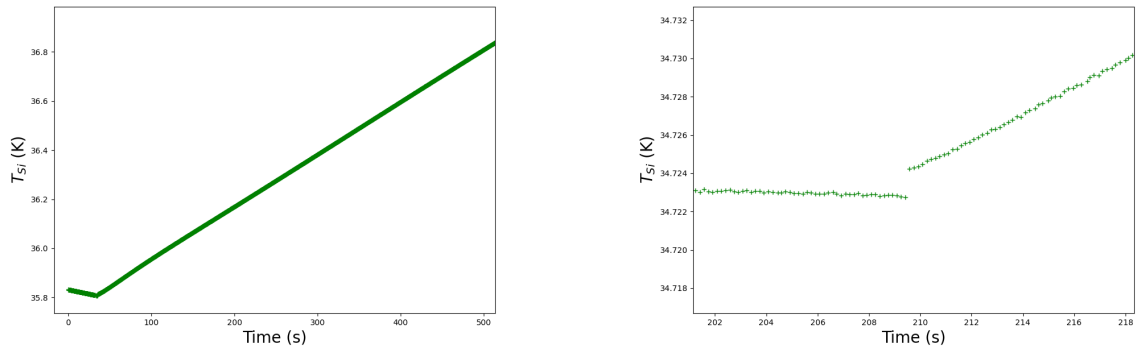

Figure 7.17: Close up view of the impulsive measuremnt signal during (right) and after (left) laser activation during the second campaign.

On the contrary, the sharp temperature variation that is sensed by the CX-1050-SD thermometer when the laser beam is switched on is present in both the first and second campaign acquisitions. In the previous section it was hypotized that this dicontinuous temperature change is a real physical signal with a characteristic time much smaller than the sampling period. The opposite hypotesis, that the observed signal is a read out artifact, was extensively tested against through a detailed debugging of the read out system, finding no evidence to its support.

A second set of impulsive measurements was performed in which it was varied the input optical power between different acquisitions. The various data acquisitions were fitted against the usual exponential temperature rise model with constrained initial equilibrium temperature ($T_{Si,0} = 31.7\,\mathrm{K}$). This way the total amplitude of the exponential temperature rise k extracted from the sample temperature signal fit could be unbiasedly compared to the ones obtained from different acquisitions. The evolution of the k parameters extracted from sample temperature data fit as a function of the input optical power is shown in Fig.7.18. The k versus P_{Las} experimental data clearly exhibits a linear proportionality. All the data points lie within 1σ uncertainty to the linear model fitting curve. In addition, the intercept of the linear fit is 1σ compatible with the origin of the y axis, which is the correct physical expectation for any model trying to describe $k(P_{Las})$ evolution: when there is no optical power entering the sample the resulting temperature variation sensed by the CX-1050-SD should be null.

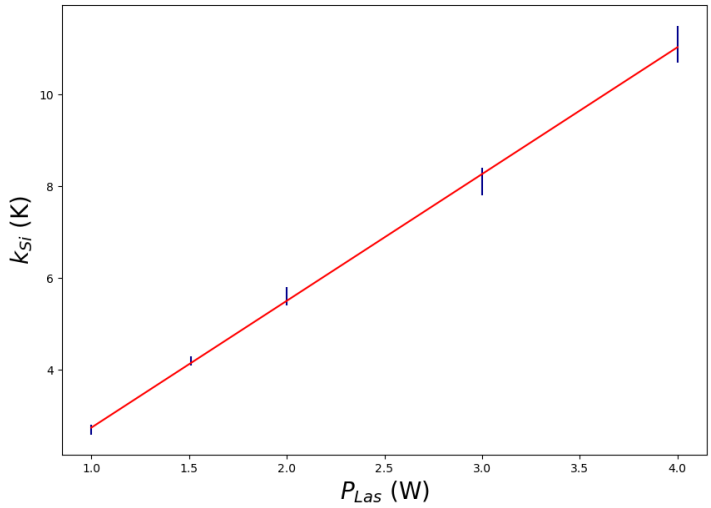

Figure 7.18: Evolution of the k parameter extracted from Eq.6.20 model fit of the sample temperature data in input optical power varying acquisitions.

a (K)	b (K/W)
0.0 ± 0.1	2.76 ± 0.05

Table 7.7: Resulting parameters of Fig.7.18 fit. Fit model: $k(P_{Las}) = a + b\,P_{Las}$

The linear proportionality coefficient $b = 2.76 \pm 0.05\,\mathrm{K/W}$ is instead the parameter that contains the information on the optical absorption in the sample. Under the assumption that the excess reflected power heat flow contribution on the sample has become negligible in this new configuration, the observed exponential temperature rise is predominantly caused by silicon optical absorption. In order to extract the sought information on the silicon absorption coefficient from this experimental slope, a calibration procedure would be necessary, as already explained in Sec.6.2.4.
A different technique to obtain a reference signal for the calibration of impulsive measurements would be to perform an accurate numerical simulation of the system thermodynamics. This approach was actually attempted by recycling Sec.6.2.4 system modelization and implementing the empirical estimate of the A_c and A_{eff} quantities that were obtained throughout this chapter. Unfortunately this

improvement of the system modelization was still not enough to accurately describe the whole chamber thermodynamics. In fact the assumption that was used in the aformentioned model by which the radiation shield temperature is stabilized at a fixed value during the whole acquisition is too strong. The total amplitude of the exponential temperature rise in the shield that was measured during second campaign acquisition as a function of the input optical power is illustrated in Fig.7.19. As it is being proven in the current section, this radiation shield temperature rise is not caused by direct absorption of the reflected power from the sample input surface. The shield is instead heated from the increased radiation heat flow coming from the sample, which is increasing its temperature as a function of time. In order to properly model this heat flow contribution it would be needed to perform an independent measurement of the radiation shield capacitance and thermal coupling with the refrigerating cold head. This obtain this information is a non trivial operation that would require further tests and measurents for which we lacked the time to perform. As a consequence, in the current experimental set up impulsive measurement could only serve as a tool to perform an in depth investigation over the system thermodynamics and could not provide instead an independent estimate of the silicon optical absorption coefficient in a cryogenic environment.

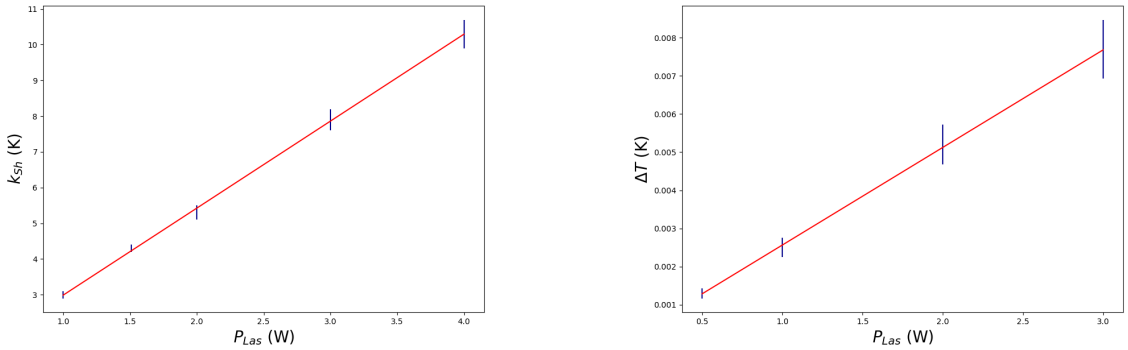

Figure 7.19: Left: k parameter extracted from Eq.6.20 model fit to shield temperature rise data in input power varying acquisitions. Right: Amplitude of the impulsive temperature variation sensed by the CX-1050-SD thermometer after laser activation as a function of the laser optical power.

Signal	a (K)	b (K/W)
Radiation Shield	$5.5 \pm 0.9 \times 10^{-1}$	$2.44 \pm 0.04 \times 10^{0}$
Laser activation	$2.1 \pm 0.6 \times 10^{-4}$	$2.36 \pm 0.07 \times 10^{-3}$

Table 7.8: Linear model fit parameters of Fig.7.19 data.

It is also useful to analyze the behaviour of the small-τ signal that manifests in impulsive measurements right after the laser activation instant as a function of the input laser power. The faster signal has such a small characteristic time that is able to thermalize with the silicon crystal in a few sampling periods, where the sampling frequency at which all the second campaign impulsive acquisitions were performed was $f_s = 6\,\mathrm{Hz}$. It should be then expected a linear proportionality between the amplitude of the laser activation temperature variation and the input laser power in the system. This is because determining the total temperature excursion of the fast signal is analogous to extracting the k parameter from an exponential rise model fit. Fig.7.19 illustrates the relation between this two quantities that was observed during input power varying acquisitions in the mirror aided configuration of the second campaign. Despite the few available data points, the linear distribution of the total temperature

variation respect to input optical power is verified.

Modulation Calorimetry Measurement

Even in the case of Modulation Calorimetry measurement the acquisition and data processing procedures were analogous to the one developed during the first campaign. The second campaign of modulated measurements was started by performing a set of input polarization varying acquisitions to quantify the effect of the excess reflected power on the system thermodynamics in Modulation Calorimetry conditions after the change of optical configuration inside the cryogenic chamber. The laser power modulation parameters were set to $p_{out} = 1.088 \pm 0.001\,\mathrm{W}$,$\omega_p = 0.34147 \pm 0.00005\,\mathrm{rad/s}$ in all the acquisitions. Fig.7.20 illustrates the behaviour of the amplitude of sample temperature oscillations as a function of the HWP rotation angle. Also in the case of Modulation Calorimetry measurements it is evident that the new configuration has solved the problem of the additional contribution due to the reflected power. In particular, from the figure it can be seen that by changing the input polarization away from the p-state, the amplitude of the temperature modulation decreases, which can be explained only by assuming that the sample heating is mainly caused by the absorbed part of the p-polarized power which is transmitted throught the sample.

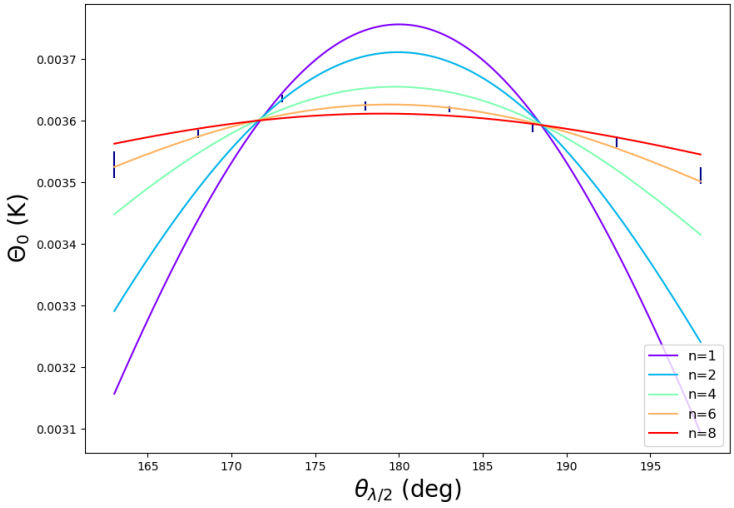

Figure 7.20: Amplitude of sample temperature oscillations as a function of the HWP rotation angle in second campaign acquisitions. Experimental data was fitted with Eq.7.15 model for different n values.

k (K)	θ_0 (deg)
$3.61 \pm 0.06 \times 10^{-3}$	179 ± 2

Table 7.9: Fit parameters for the $n = 6$ case of Eq.7.15 model on Fig.7.20 data.

Following this observation, the data points must be fitted with a model in which the sample temperature oscillations are driven by optical absorption in the silicon crystal. The model is analogous to the

one of Eq.7.14, in which it is accounted for both s- and p-polarization component in the beam that is reaching the sample input surface. That is, the model accounts for the depolarizing effect of the chamber input window. The only difference respect to Eq.7.14 model is that it will be considered the contribution of a finite number n of internal reflection:

$$\Theta_0(\theta) = k\Big[\cos^2(\theta-\theta_0) + T_s\sin^2(\theta-\theta_0)\sum_{m=0}^{n} R_s^m\Big]. \tag{7.15}$$

The above model was tested against the experimental data for different values of n (Fig.7.20). A comparison of the χ^2_ν associated to the different fits indicates that the $n = 6$ model is the one that better matches the observations. All the data points lie within 1σ uncertainty from the fitting curve in the $n = 6$ case, except for the $\theta_{\lambda/2} = 173°$ outlier that was excluded from the set of point over which the fit is performed. Then, the observed $\Theta_0(\theta_{\lambda/2})$ distribution further validate the hypotesis under which silicon optical absortion is the leading contribution to the sample thermodynamics in second campaign acquisitions. The above estimate on the number of internal reflections of p-polarized light in the sample is also compatible with the $n = 4 \pm 2$ geometrical estimate of the same quantity, that is obtained by comparing the distance between parallel internal reflections at Brewster angle to the dimension of the sample orthogonal side to the input beam.

7.3.1 Discussion of Second Measurement Campaign

The optical configuration for the cryogenic chamber system that was employed during the acquisitions of the second campaign proved to be an efficient solution for the excess reflection issue that was spoiling the first campaign measurements. Minimization of the reflected power contribution was a mandatory requirement for the identification of the source of the different signals observed in impulsive measurements, that could not be resolved with the help of thermodynamical simulations during first campaign analysis. The qualitative difference between the signal sensed by the CX-1050-SD thermometer in the two configurations (First campaign: Fig.7.4; Second campaign: Fig.7.17) can be explained in the following framework. The large-τ exponential ($\tau \approx 2000\,\mathrm{s}$) is the signal associated with the sample temperature rise. The sample signal is caused in first place by optical absorption in the silicon crystal but also by the effect of the excess reflected power that overheats the sample either directly, through diffuse light, or indirectly, by heating up different parts of the chamber that then irradiate or conduct heat back into the sample. The effect of the excess reflection is dominant in the first campaign acquisitions, as it was illustrated in Fig.7.5, while silicon optical absorption is the leading contribution in the new mirror aided configuration. The small-τ exponential ($\tau \approx 25\,\mathrm{s}$) that was observed during first campaign acquisitions was instead caused by the excess reflection heating up a third thermally independent body inside the chamber, that eventually transfer excess heat back into the sample. As there is no direct optical absorption contribution on this independent body, its signal vanishes when the majority of the excess reflected power is evacuated from the chamber.
The above evidence settles down also the issue regarding the estimate of the A_c and A_{eff} quantities, of which it was possible to only determine the relative ratio after the first acquisition campaign. Following the aformentioned interpretation, a large-τ exponential temperature rise on the sample is recreated by simulations with the ($\mu \approx r_{c/r}$,$\epsilon \approx 1$) model. More specifically, this evidence points out that the radiation effective area is approximately equal to the one computed in the concentric spheres modelization of the cryogenic chamber, so that the emissivity of the two inner surfaces is almost unitary; the contact area for heat conduction is instead much smaller than the first geometrical estimate that was provided in Sec.6.2.4: a $\mu \approx r_{c/r}$ attenuation factor must be included in its computation to account for the poor thermal coupling between the separate teflon and copper parts that are interfacing between the silicon crystal and the copper support.

As to the discountinuous temperature variation in the instant following the laser activation in impulsive measurements, the same feature is present in both first and second campaign acquisition. The signal physicality hypotesis has already been confirmed during Sec.7.2, but it will be further validated in next paragraph, where it will be demonstrated a linear proportionality between the amplitude of the temperature discontinuity and the input power on the sample. Then the signal should be identified a very small capacitance body inside the chamber that could couple to the CX-1050-SD thermometer to generate the observed small-τ signal. The most straight-forward hypotesis to explain this kind of signal would be the one involving a small portion of the input or reflected beam that is directly impinging on the the thermometer surface, causing a sharp overheating; next to the initial non-equilibrium phase the CX-1050-SD fastly thermalizes with the sample thanks to its very good coupling with the crystal. The fact that the signal is still present in the mirror aided configuration indicates that it cannot be caused by an indirect reflection or diffused light associated with the excess reflection on the sample input surface. The excess heat flow on the thermometer could instead be caused by a non-negligible portion of the input beam that is clipping on the sample upper edge, above which the Cernox thermometer is placed, or by an internal s-polarized reflection, in the case that the beam is entering non-perpendicular to the sample optical plane.

Having completed the impulsive measurement picture, the attention can be turned on Modulation Calorimetry measurements. The crucial analysis for the Modulation Calorimetry method is the one regarding ω_p varying acquisitions. During the second measurement campaign it was performed a set of modulated acquisitions in which the modulation frequency was discretely varied in the $[0.02 - 0.3]$ Hz range. All the other optical parameters were kept fixed throughout the various acquisitions: $p_{out} = 372 \pm 5\,\mathrm{mW}$, $\theta_{\lambda/2} = 183°$.
At first it can be studied the distribution of the phase retardation of the temperature signal as a function of the modulation frequency (Fig.7.21: left). The tangent of the phase shift between power and temperature oscillating signals distributes in the same qualitative way of the first campaign data (Fig.7.10). Again, this pattern can be explained with a model that accounts for the sum of two equal-frequency sinusoidal signals with ω_p-dependent amplitude and phase. Such a model was already made explicit in the 7.8 and 7.9 equations of the previous section. The same model is also able to account for the Θ_0 versus ω_p behaviour (Fig.7.21: right), as the distribution of the experimental data acquired in the new mirror-aided optical configuration inside the chamber is qualitatively similar to the one that was observed during first campaign acquisitions (Fig.7.10).

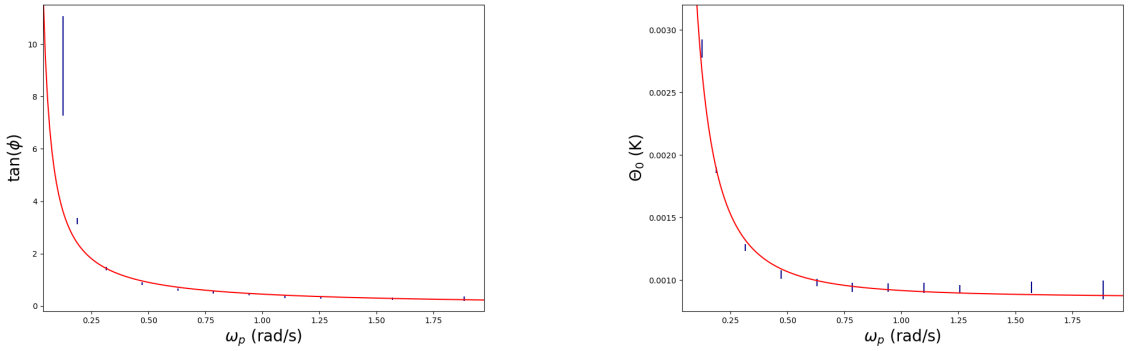

Figure 7.21: $\tan(\phi)$ and Θ_0 data obtained from ω_p-varying acquisitions during second campaign.

Contrarily to the first campaign situation, it is now possible to confidently identify the nature of the two superiposing signals. Sec.7.3 evidence proved that the insertion of the two steering mirror on the copper support optical plane succeded in the evacuation of the largest part of the promptly reflected

k_1 (K)	p_{in} (W)
$8.6 \pm 0.2 \times 10^{-4}$	$7.2 \pm 0.2 \times 10^{-5}$

Table 7.10: Parameters for the $\Theta_0(\omega_p)$ fitting curve for the Eq.7.20 model.

optical power, which was inputing a non negligible and non quantifiable heat flow contribution in the sample. This implies that there are only two remaining contributions that are independently driving the oscillating signal that is sensed by the CX-1050-SD thermometer: a first component that is directly caused by optical absorption in the silicon crystal and a second component which has same origin of the smallest-τ signal that was observed in impulsive acquisitions.
The two superimposing signal have considerably different natures, so that they can be succesfully decoupled. The notation for the two sinusoidal contriutions that was established in Sec.7.2 is recalled:

$$\begin{aligned} T(t) - T_0 =& A\sin(\omega_p t + \gamma) + B\sin(\omega_p t + \delta) = \\ =& \Big[\big(A\cos(\gamma) + B\cos(\delta)\big)^2 + \big(A\sin(\gamma) + B\sin(\delta)\big)^2\Big]^{1/2} \\ & \sin\Big(\omega_p t + \tan^{-1}\big(\frac{A\sin(\gamma) + B\sin(\delta)}{A\cos(\gamma) + B\cos(\delta)}\big)\Big) = \\ =& \Theta_0 \sin(\omega_p t + \phi). \end{aligned} \tag{7.16}$$

The fast responding signal is able to couple with its driving power source throughout all the inspected modulation frequency range, thus its amplitude and phase will be ω_p independent:

$$\begin{aligned} A &= k1 \\ \gamma &= 0. \end{aligned} \tag{7.17}$$

The slower signal is instead associated with optical absorption in the sample. In the most general form the amplitude and phase of this signal are governed by the Modulation Calorimetry equations that were developed in the section dedicated to the theory of the measurement technique (Eq.6.6), but the modulation calorimetry solution can be simplified if the system enters adiabatic regime. The $\tan(\phi) > 10$ adiabatic regime condition on the phase retardation of the tempearature signal translates in a lower bound condition on the modulation frequency, as it was seen in Eq.6.26. The adiabatic regime condition on the modulation frequency ω_p is directly proportional to the linear heat flow coefficient Q' which was in its turn modeled as directly proportional to the contact area for the conductive heat flow. Explicitely putting together Eq.6.25 and Eq.6.26 it is obtained an expression linking ω_p and A_c in adiabatic regime conditions:

$$\omega_p \geq \frac{10\, k_P\, A_c}{z_P\, m\, c_{p\,Si}(T_{Si})}. \tag{7.18}$$

In Fig.6.26 this lower bound on the modulation frequency was computed under the $A_c = A_c^{geom} = 10^{-5}\,\mathrm{m}^2$ assumption. On the contrary, over the course of the measurement campaign sections it was concluded that this initial estimate was inaccurate and that the effective area for heat conduction must be computed including an attenuation factor to account for the non ideal thermal coupling between different material contacting surfaces ($A_c = \mu A_c^{geom}$). The following attenuation factor estimate was produced by combining heater-only acquisition equilibrium data with the τ_{Si} evidence that was obtained during second campaign impulsive measurements: $\mu \approx r_{c/r} A_{eff}^{geom}/A_c^{geom} = 4.63 \pm 0.06 \times 10^{-4}$. This result directly impacts on the adiabatic regime condition for ω_p: the modulation frequency that is needed to achieve adiabatic regime on the sample in the real case is $O(10^{-2})$ lower than the initial estimate. Referring to Fig.6.26 data and considering that in the current cryogenic chamber set up the sample temperature cannot be lowered below $T_{Si} = 30\,\mathrm{K}$, it results that the adiabatic regime condition

on the sample is fullfilled across all the tested modulation frequency range $\omega_p \in [0.01 - 0.3]$ Hz.
The above argument allows to simplify the amplitude and phase expressions of the slower sinusoidal contribution:

$$\begin{aligned} B &= \frac{p_{in}}{m_{Si} c_{Si} \omega_p} \\ \delta &= \pi/2. \end{aligned} \tag{7.19}$$

By inserting the information on the phases of the two superimposing signals in the formulation of the total signal modulation amplitude (Eq.7.16), the Θ_0 expression simplifies to:

$$\Theta_0 = \sqrt{A^2 + B^2} = \left[k_1^2 + \left(\frac{p_{in}}{m_{Si} c_{Si} \omega_p} \right)^2 \right]^{1/2} \tag{7.20}$$

Finally, the above model can be fitted to the $\Theta_0(\omega_p)$ data obtained during second campaign modulated acquisitions. In the above model, the silicon specific heat value is computed using Eq.6.19 model with sample temperature equal to the average temperature of the various modulated acquisitions ($T_{Si} = 40.37 \pm 0.01$ K), the silicon sample mass value is inherited from Tab.6.1 and k_1 and p_{in} are instead left as free parameters. The result of this fit is graphically illustrated in Fig.7.21, while the least squares parameters are listed in Tab.7.10.
All the data points are 2σ compatible with the fitting curve, confirming the validity of the assumptions that were used to develop Eq.7.20 model. The p_{in} parameter corresponds to the total absorbed input power inside the sample and is the relevant quantity for the optical absorption estimate in the Modulation Calorimetry framework. The k_1 parameter quantifies instead the modulation frequency independent amplitude of the faster contribution.

Over the course of this section it was assumed that the small-τ signal that was observed right after the laser activation instant of impulsive acquisitions and the faster contribution to the Modulation Calorimetry signal are originated by the same physical process. The validity of this assumption can be evaluated by comparing the two independent estimates of the amplitude of such signal.
In Fig.7.19 it was observed a linear proportionality between the amplitude of the small-τ signal and the power that is injected in the cryogenic chamber. Assuming that the process originating the fast signal is able to achieve thermal equilibrium in a smaller time interval respect to the sampling period of impulsive acquisitions, then the observed signal amplitude is comparable with the one obtained from modulated measurements, where the input source has a slower variation so that thermal equilibrium is easier to achieve. In ω_p-varying Modulation Calorimetry measurements the input power modulation amplitude was fixed to the constant value $p_{Las} = 0.372 \pm 0.005$ W, resulting in a $A = k_1 = 8.6 \pm 0.2 \times 10^{-4}$ K amplitude of sample temperature oscillation for the faster signal. An indepentent estimate of A can by computing the $P_{Las} = p_{Las}$ prediction of the $\Delta T(P_{Las})$ linear model for the fast signal amplitude that was obtained from impulsive measurements data (Tab.7.8): $A = 9.6 \pm 0.7 \times 10^{-4}$. The two independent estimates of the fast signal amplitude have 2σ compatibility. This result contributes to the validation of the hypotesis that the fast signals observed in impulsive and modulated acquisition has the same physical origin.

7.4 α_{Si} Estimate

The set of Modulation Calorimetry acquisitions performed in the experimental set up of the second campaign allowed to obtain an estimate of the modulation amplitude of absorbed power in the silicon sample: $p_{in} = 7.2 \pm 0.2 \times 10^{-5}$ W. Following Sec.6.1 derivation, it is possible to relate this quantity

to an optical absorption estimate for crystalline silicon in a cryogenic environment.
In modulated acquisitions the power measurement is performed at fiber output by means of the Keopsys laser internal powermeter. The amplitude of optical power oscillations at fiber output was set to the constant value of $p_{out} = 0.372 \pm 0.005\,\mathrm{W}$ throughout all the ω_p varying acquisitions, from which the p_{in} estimate has been extracted. The amount of output optical power that reaches the sample input surface is computed by recalling that the optical isolator system was set in its configuration of maximum transmittance throughout all the modulated acquisitions ($T_{FI}^{Max} = 0.974 \pm 0.002$). The AR coated input window of the cryogenic chamber has a finite transmittance $T_{Wind} = 0.995$ and it induces a depolarizing effect on the beam which causes an unavoidable $R_{\theta_B}^{Min} = 0.06 \pm 0.01$ reflectivity at Brewster angle. The resulting amplitude of optical power oscillations that manages to enter the sample input surface is then: $p_{Las} = T_{FI}^{Max}\, T_{Wind}\, (1 - R_{\theta_B}^{Min})\, p_{out} = 0.361 \pm 0.005\,\mathrm{W}$.

The s-polarized and p-polarized portions of the input optical power should then behave and contribute differently to optical absorption. Nevertheless it is possible to neglect the p-polarized light contribution to optical absorption by recalling that the HWP rotation angle was set to $\theta_{\lambda/2} = 183^\circ$ throughout all the ω_p-varying modulated acquisition. The fraction of p-polarized optical power is Malus' law distributed respect to the $\theta_{\lambda/2}$ angle ($p_{Las,p} = p_{Las} \sin^2(2(\theta_{\lambda/2} - \theta_{\lambda/2,0}))$), where the p-polarization minimization angle $\theta_{\lambda/2,0} = 183.022 \pm 0.007^\circ$ has been determined from Fig.7.8 fit. This implies that the p- versus s- polarized component ratio is approximately $p_{Las,p}/p_{Las,s} = O(10^{-7})$, rendering the p-polarized light contribution to optical absorption negligible.
The p-polarized optical power gets fully transmitted outside of the sample after having covered a $l = l_x/\cos(\theta_t) = 1.046 \pm 0.006 \times 10^{-2}\,\mathrm{m}$ optical path inside the sample, where $l_y = 1.005 \pm 0.005 \times 10^{-2}\,\mathrm{m}$ is the length of the side of the sample that is parallel to the input surface normal vector and $\theta_t = 0.28 \pm 0.01\,\mathrm{rad}$ is the transmission angle for air-silicon interface in the case of a $\theta_i = 1.29 \pm 0.01\,\mathrm{rad} \approx \theta_B$ input beam. Assuming a linear model for optical absortion, all the transmitted p-polarized optical power contributes to the oscillation amplitude of absorbed power: $p_{in} = \alpha_{Si}\, l\, p_{Las}$. The amplitude of absorbed power oscillations has been experimentally determined through the fit of Fig.7.21 data via Eq.7.20 model: $p_{in} = 7.2 \pm 0.2 \times 10^{-5}\,\mathrm{W}$.

It is eventually possible to obtain an estimate for the cristalline silicon optical absorption coefficient α_{Si} by rearranging the previous equation:

$$\alpha_{Si} = \frac{p_{in}}{p_{Las}\, l} = (2.03 \pm 0.07) \times 10^2\,\mathrm{ppm/cm}. \tag{7.21}$$

It is necessary to underline that this α_{Si} estimate is affected by a sistematic error that is larger in mangitude than its statistical error that was presented in Eq.7.21. This systematic error is originated by the following issue. The sample temperature was determined by performing a 4-wire measurement of the CX-1050-SD resistance, wich was then converted to a temperature value with the use of the static calibration curve that was presented in Sec.6.2.2. The static calibration procedure was developed to adress the isteresis-like behaviour of the sensed values of CX-1050-SD resistance in cooling and heating phases of the broad range calibration attemps. This second calibration method required to acquire the $T_{Si}(R_{cx})$ calibration data points in thermal equilibrium conditions. Then, in the framework of our experimental set up, the static calibration could be performed by clamping both the CX-1050-SD and the DT-470 reference thermometer to the copper support, the temperature of which could be controlled with the use of the PID resistive heater. The PID heater allowed to stabilize the copper support temperature in the $[15 - 25]\,\mathrm{K}$ range.
On the other hand, due to a poor conductive thermal coupling between the silicon crystal and the copper support, when the sample was installed in its teflon housing it was not possible to lower its temperature below $T_{Si} \approx 30\,\mathrm{K}$. In fact, Modulation Calorimetry measurements required the injection of a modulated optical power in the silicon crystal with $P_{Las}^{avg} = 1.923 \pm 0.004\,\mathrm{W}$ average power, to which it corresponds a laser-on equilibrium temperature on the sample of $T_{Si}^{avg} = 40.37 \pm 0.01\,\mathrm{K}$.

This incompatibility between the temperature ranges in which the calibration was performed and the sample absorption was tested introduces a systematic error in the final α_{Si} estimate. We do not dispose of an accurate calibration for the CX-1050-SD resistance signal in proximity of the T_{Si}^{avg} value so that we need to extrapolate the Fig.6.6 calibration curve outside of the range where its empirical model was originally tested. It is possible to give an estimate of the systematic error that is introduced by this temperature measurement procedure on the determination of the sample temperature oscillation amplitude Θ_0 in modulated acquisition.
The determination of temperature oscillations amplitude is a differential measurement. That is, the Θ_0 quantity is directly proportional to the derivative of the calibration curve for the CX-1050-SD resistance signal. To compute the relative calibration uncertainty associated to Θ_0 estimates it is then necessary to perform error propagation on the derivative of the calibration curve dT/dR. Starting from the static calibration fit model of Eq.6.12, the derivative of the calibration curve is computed:

$$T'(R_{cx}) = \frac{dT}{dR}(R_{cx}) = \frac{b}{(R_{cx} - c)^2}. \tag{7.22}$$

From there it is immediately obtained the error propagation formula for the calibration curve derivative:

$$\sigma_{T'}(R_{cx}) = \sqrt{\left[\frac{\sigma_b}{(R_{cx} - c)^2}\right]^2 + \left[\frac{2b\sigma_c}{(R_{cx} - c)^3}\right]^2} \tag{7.23}$$

where the $\sigma_{R_{cx}}$ contribution has been neglected due to the fact that the relative uncertainty of the 4-wire resistance measurement is orders of magnitude smaller compared to one associated to the calibration parameters estimate. This expression has to be evaluated in $R_{cx} = R_{cx}^{avg}$, that is the average resistance value of the CX-1050-SD signal during modulated acquisition. All the calibration parameters and uncertainties are provided in Tab.6.3. The resulting relative uncertainty on the static calibration curve derivative in the temperature region of modulated measurements is: $\frac{\sigma_{T'}}{T'}(R_{cx}^{avg}) \approx 0.17$.
The derivative of the static calibration curve T' is proportional to the measured amplitude of sample temperature oscillations Θ_0, which is in its turn proportional to the amplitude of absorbed optical power oscillations p_{in} via the fundamental equation of modulation calorimetry Eq.6.7. For this reason the relative uncertainty contribution that was just computed for the calibration curve derivate directly propagates to the α_{Si} estimate that was provided in the previous paragraph. This calibration error is by far the largest contribution to the uncertainty of the silicon optical absorption estimate, which eventually must be corrected to the following value:

$$\alpha_{Si} = (2.0 \pm 0.3) \times 10^2 \,\mathrm{ppm/cm}. \tag{7.24}$$

In the end, the validity of the Modulation Calorimetry technique for performing an $O(100\,\mathrm{ppm/cm})$ optical absorption measurement within the constraints of the experimental set up that was designed and developed over the course of this document is demonstrated. An $O(10\%)$ accurate estimate of the crystalline silicon optical absorption coefficient α_{Si} in criogenic environment has been successfully obtained.
It should be noted that the conclusive estimate for the crystalline silicon optical absorption coefficient is in principle only valid in the small temperature region in which the second campaign Modulation Calorimetry acquisitions have been performed ($T_{Si}^{avg} \approx 40.37\,\mathrm{K}$). Also this temperature estimate suffers of a considerably large sistematic error caused by the same calibration issue that was presented in the former paragraph. By performing an analogous error propagation for static calibration curve extrapolation evaluated in R_{cx}^{avg}, it is obtained the 1σ uncertainty associated with T_{Si}^{avg}, the silicon crystal temperature at which Eq.7.24 is valid: $40 \pm 5\,\mathrm{K}$.

Chapter 8

Conclusions

8.1 Consequences for the Einstein Telescope design

Crystalline silicon is among the most favourite candidates to serve as test mass substrate material in third generation gravitational wave detectors. A summary of its excellent mechanical and thermal properties has been presented in Ch.5. Despite the large amount of literature on crystalline silicon properties that was prompted by a strong intrest on the material by the telecomunication industry, little is known about its absorption spectrum at cryogenic temperatures. The only direct experimental evidence on silicon optical absorption for $\lambda = 1550\,\mathrm{nm}$ light in a cryogenic environment was obtained by [55], where it was found a nearly temperature independent optical absorption coefficient in the $[5 - 300]\,\mathrm{K}$ range with value: $\alpha_{Si} \approx 300\,\mathrm{ppm/cm}$. This evidence was also in contrast with the existing theoretical expectations for a negligible optical absorption at low temperatures due to carrier freezout.
This work provided an independent estimate of α_{Si} at cryogenic temperatures which supports the evidence for an $O(10^2\,\mathrm{ppm/cm})$ optical absorption coefficient for $\lambda = 1550\,\mathrm{nm}$ light ($\alpha_{Si} = 200 \pm 30\,\mathrm{ppm/cm}$). The aforementioned optical absorption measurement was specifically performed at an average temperature of $T_{Si} = 40 \pm 5\,\mathrm{K}$, but the cryogenic facility that was developed during the course of this thesis work will allow to perform a complete characterization of crystalline silicon optical absorption in a wide range of temperatures in the near future. Moreover it should be investigated the α_{Si} dependency from a variety of different parameters, such as the purity of the crystal or the intensity of the input beam. It is also of fundamental importance to carry out an analysis that allows to decouple surface and bulk absorbtion contributions in the silicon crystal. This is because it is suspected that the leading contribution to the $\lambda = 1550\,\mathrm{nm}$ α_{Si} value that was indepently measured in this work and in [55] paper and which is large compared to existing predictions based on semiconductor theory, is associated to temperature independent surface absorption processes.
Following the [55] indication about a nearly temperature independent absorption, it is possible to extend the validity of the α_{Si} estimate that was found in Sec.7.3 to lower temperatures to investigate its consequences on the design of the Low-Frequency cryogenic interferometer of the Einstein Telescope. In particular, an higher than expected optical absorption value in the test mass substrate material could threaten the cryocenic operation of the interferometer system. The original working temperature requirement for the ET-LF interferometer was $T_{mir} = 10\,\mathrm{K}$, where T_{Mir} is the temperature on the test mass. The excess heat that is injected in the test mass through optical absorption is evacuated through the suspension fibers, which hang the payload to the marionette that has the dual purpose of actively controlling the mirror position and providing a temperature stabilized point of contact for the test mass system. The operating temperature of the marionette stage in the ET-D design was set to $T_{Mario} = 4\,\mathrm{K}$. The excess absorbed power is then proportional to the injected and circulating optical power in the interferometer cavities. The quantity of intrest for bulk absorption estimate in substrate candidate materials is the optical power that gets trasmitted through the input test mass, that in the case

of the most recent design of the ET-LF interferometer is $P_{in} = 65\,\mathrm{W}$[1]. Starting from this constraints in [55] it was run a FEA simulation to determine the thermodynamics of the system made up of the test mass, the suspension fibers and the marionette. The suspension fiber system was modeled by means of a single cylindrical suspension with $l_w = 1\,\mathrm{m}$ lenght and varying diameter. A set of numerical simulations was run to extract an estimate of the equilibrium temperature of the test mass as a function of the suspension cross section.

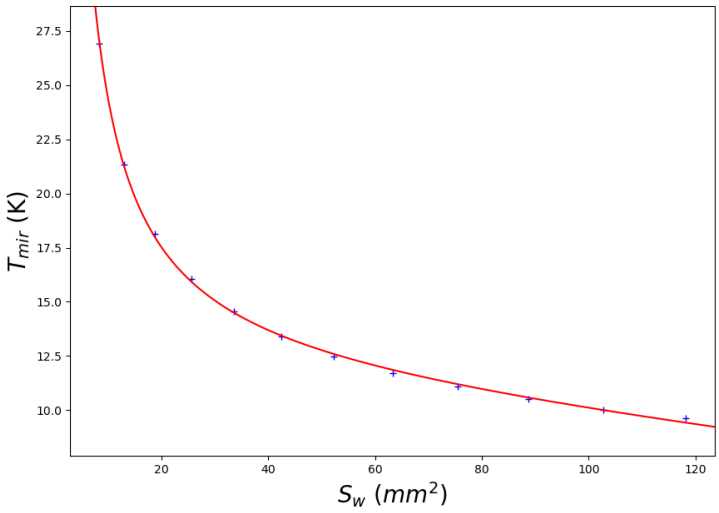

Figure 8.1: Equilibrium temperatures in the input test mass as a function of the total cross section of the suspension system. The data points were obtained by means of FEA simulations of the thermodynamical model described in Sec.8.1.

The result of the simulation can be easily rescaled to account for silicon optical absorption estimate that was found in this work. The rescaling is to be performed by noting that in laser-on equilibrium conditions the radiation heat flow contribution from the ambient to the colder mirror is negligible respect to the silicon optical absorption and suspension conduction heat flows, so that the equilibrium equation reduces to $P_{abs} = P_{wire}$:

$$P_{in}\alpha_{Si}l_{Mir} = \frac{S_w}{l_w} < k_{Si} > (T_{Mir} - T_{Mario}) \tag{8.1}$$

where l_{Mir} is the test mass lenght along the beam axis and S_w is the total cross section of the 4-wire suspension system. The average silicon thermal conductivity $< k_{Si} >$ in the suspension system is defined as:

$$< k_{Si} >= \frac{1}{\Delta T}\int_{T_{Mir}}^{T_{Mario}} k_{Si}(T)dT. \tag{8.2}$$

Due to the direct proportionality between silicon optical absorption coefficient and suspension cross section, Eq.8.1 is left invariant under an equal rescaling of the α_{Si} and S_w quantities. Then [55] simulation results can be rescaled according to the ratio of the two different α_{Si} estimates, obtaining an estimate of the $T_{Mir}(S_w)$ distribution in the $\alpha_{Si} = 200 \pm 30\,\mathrm{ppm/cm}$ case (Fig.8.1).
It can be seen that in order to achieve the ET-D design operational temperature on the test mass ($T_{Mir} =$

[1]ET-D design aims for a $18\,\mathrm{kW}$ circulating power inside the arm cavities of the Low-Frequency cryogenic apparatus. Almost the entirety of this circulating power gets reflected in the first few layers of the mirror HR coating, leading to a negligible bulk optical absorption contribution in the end test masses.

$10K$) it is necessary to install a suspension system with total cross section $S_w \geq 100\,\mathrm{mm}^2$. The cross section of the suspension wire is proportional to its mechanical dissipation and a larger mechanical dissipation translates in an increased thermal noise spectrum due to the Fluctuation-Dissipation theorem. As a consequence there is a trade-off between thermal noise minimization in the test mass and in the suspension system. An initial design for the Last Suspension Stage of the ET-LF detector test masses accounted for a four wire configuration with $d = 3\,\mathrm{mm}$ diameter and $l = 2\,\mathrm{m}$ length. Rescaling for the different wire length between ET-D simulations and the analysis showed in Fig.8.1, this particular design configuration for the suspension fibers would result in a $T_{Mir} \approx 12.5\,\mathrm{K}$ equilibrium temperature for the test mass. The final design operating temperature for the Low-Frequency interferometer must be carefully determined by accounting for both the direct impact on test mass thermal noise and the indirect impact on suspension thermal noise.

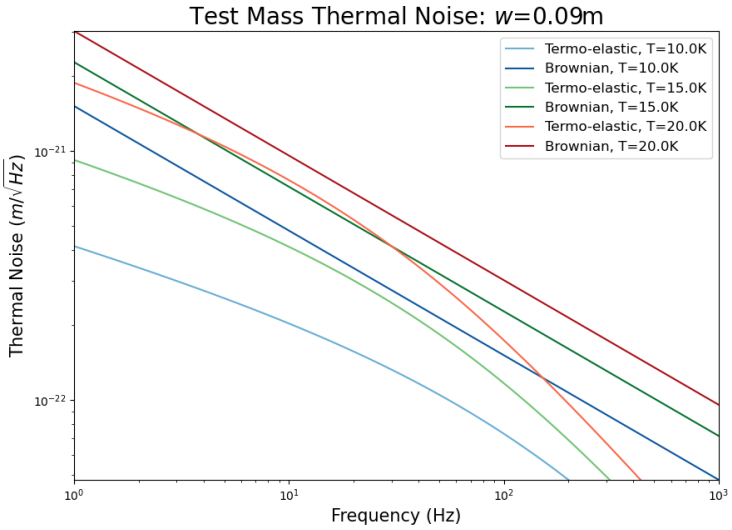

Figure 8.2: Comparison of the Brownian (Eq.3.44) and Thermo-Elastic (Eq.3.50) noise contributions for a crystalline silicon test mass operated at different cryogenic temperatures. $T = 10\,\mathrm{K}$: Blue; $T = 15\,\mathrm{K}$: Green; $T = 20\,\mathrm{K}$: Red.

It is then possible to perform an estimate of the test mass thermal noise contributions as a function of the mirror equilibrium temperature by making use of the noise power spectra that were derived in Sec.3.3. A comparison of the Brownian noise (Eq.3.44) and Thermo-Elastic noise (Eq.3.50) contributions for different values of the test mass operational temperature is illustrated in Fig.8.2. The two noise contributions are computed by considering a $w = 0.09\,\mathrm{m}$ beam radius on the test mass surface, referring to ET-D-LF design (Tab.5.1). All the quantities that appear in Eq.3.44 and Eq.3.50 spectra are computed with temperature dependent model based on literature data. Brownian noise is the dominant contribution across all the $[10 - 20]\,\mathrm{K}$ mirror temperature range.
In Fig.8.3 the total test mass thermal noise contribution, that is computed by summing up the Brownian and Thermo-Elastic components, is plotted against the ET-D design sensitivity for the Low-Frequency interferometer. The strain of the thotal thermal noise contribution is at least an order of magnitude smaller than the ET-D requirement in the whole wideband spectrum even in the worse considered case of a $T_{Mir} = 20\,\mathrm{K}$ operating temperature for the interferometer test masses. To achieve a $20\,\mathrm{K}$ equilibrium temperature on the input test mass it is sufficient design a fiber suspension system with $S_w \geq 15\,\mathrm{mm}^2$ total cross section (Fig.8.1), which would considerably lower the suspension thermal noise contribution respect to the ($T_{Mir} = 10\,\mathrm{K}$, $S_w = 100\,\mathrm{mm}^2$) initial design configuration. This value Therefore, provided that all the relevant noise and absorption contributions were accounted for in the above analysis, it can be concluded that the $\alpha_{Si} = 200 \pm 30\,\mathrm{ppm/cm}$ value for the optical ab-

sorption coefficient of crystalline silicon for $\lambda = 1550\,\mathrm{nm}$ light at cryogenic temperatures should have a containable impact on the sensitivity of the Einstein Telescope Low-Frequency detector.

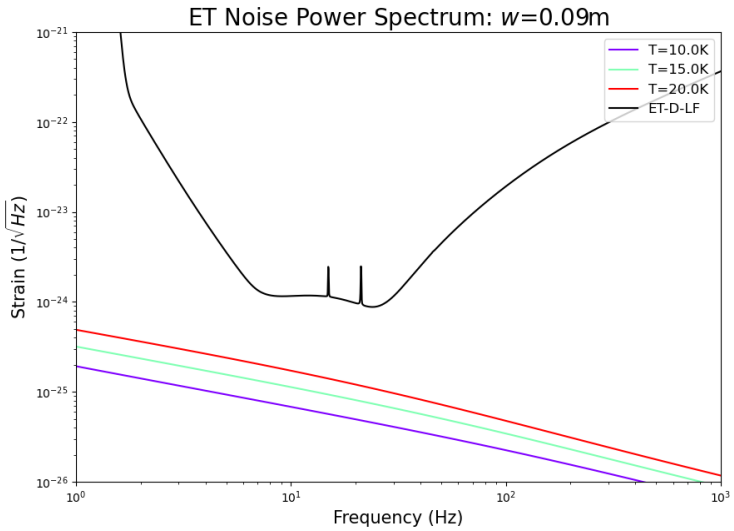

Figure 8.3: Comparison of the total mirror thermal noise contribution as a function of the test mass equilibrium temperature against ET-D design sensitivity for the Low-Frequency detector.

Appendices

Appendix A

Technical Drawings

A.1 Mirror Mount

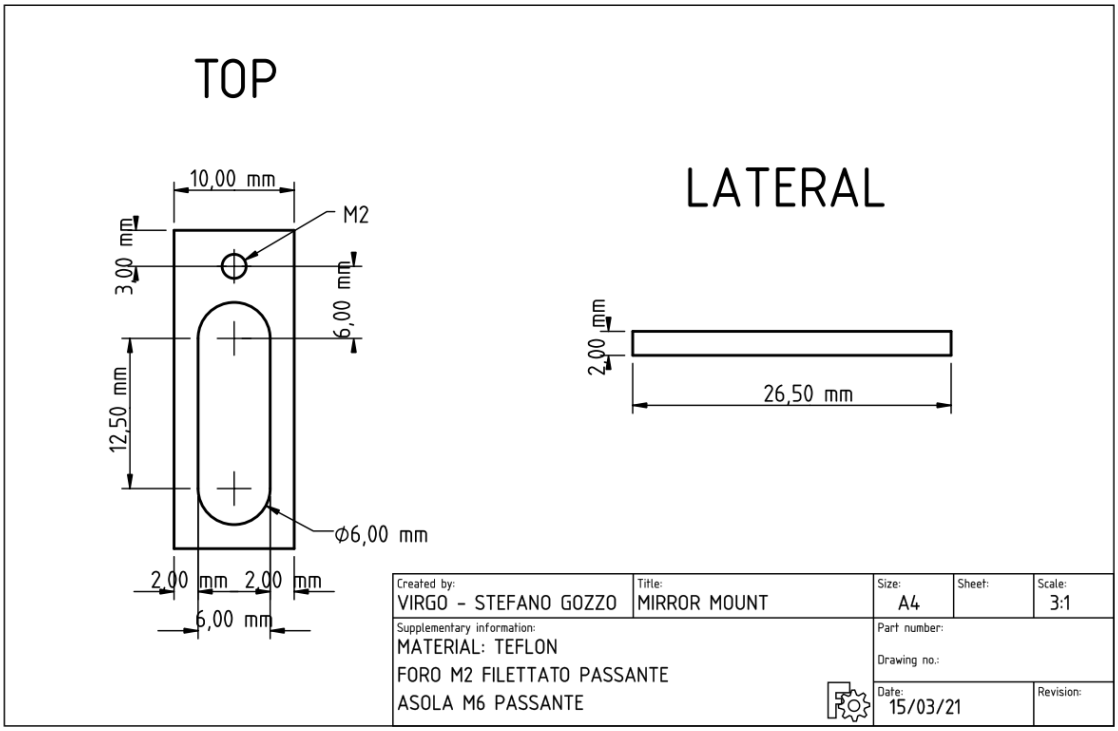

Figure A.1: Mirror Mount

A.2 Sample Support System

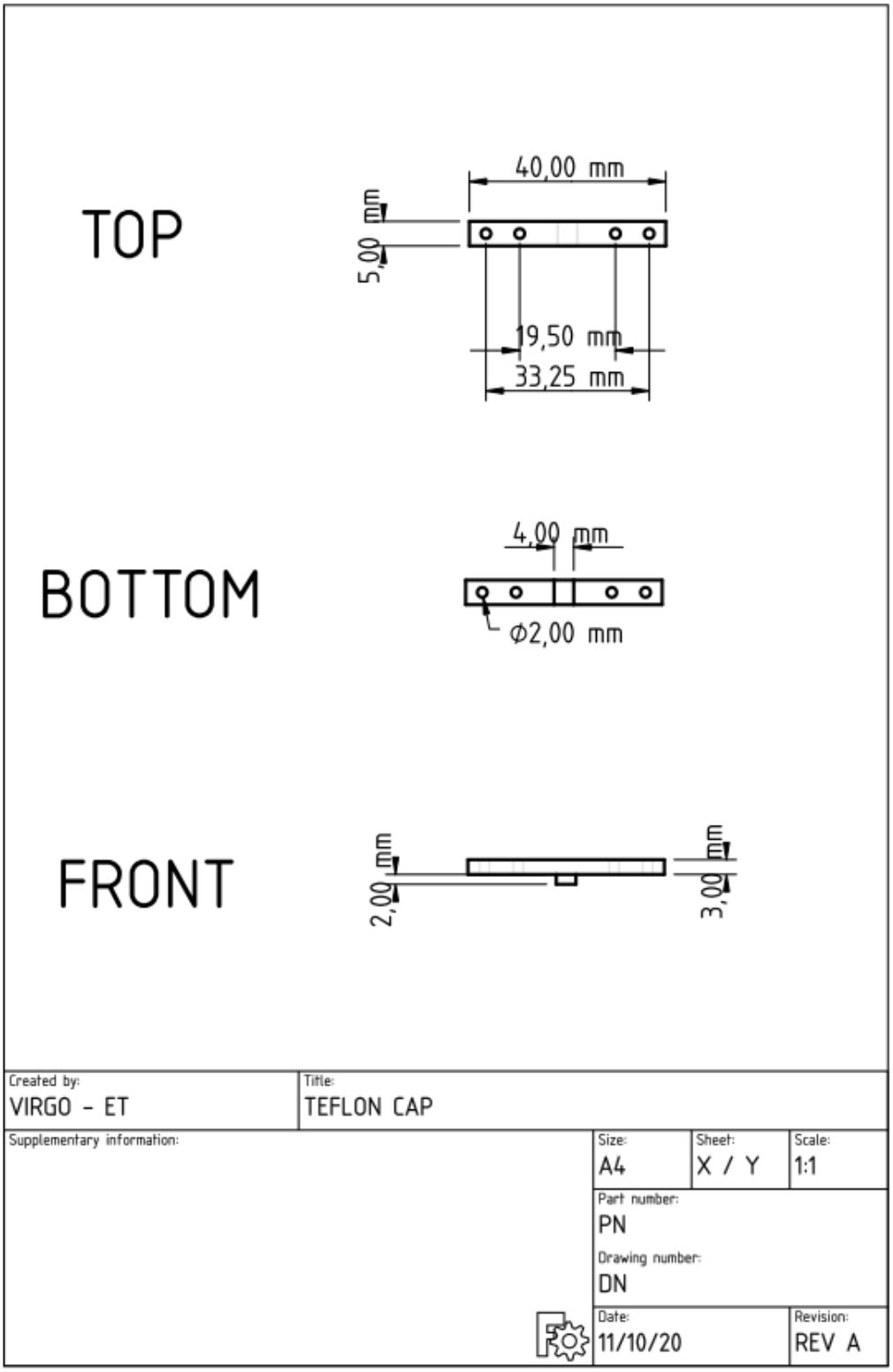

Figure A.2: Upper Layer - Teflon Cap

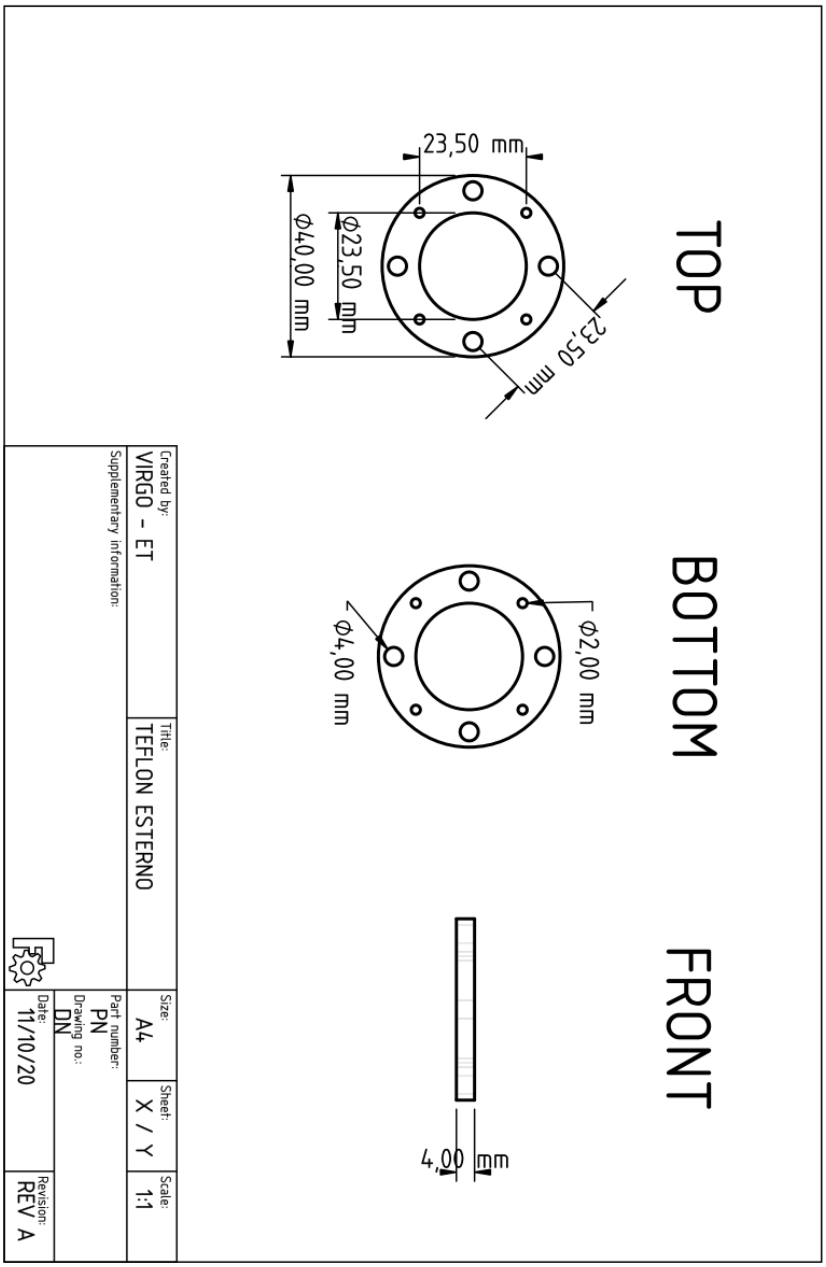

Figure A.3: Intermediate Layer - Teflon External Support

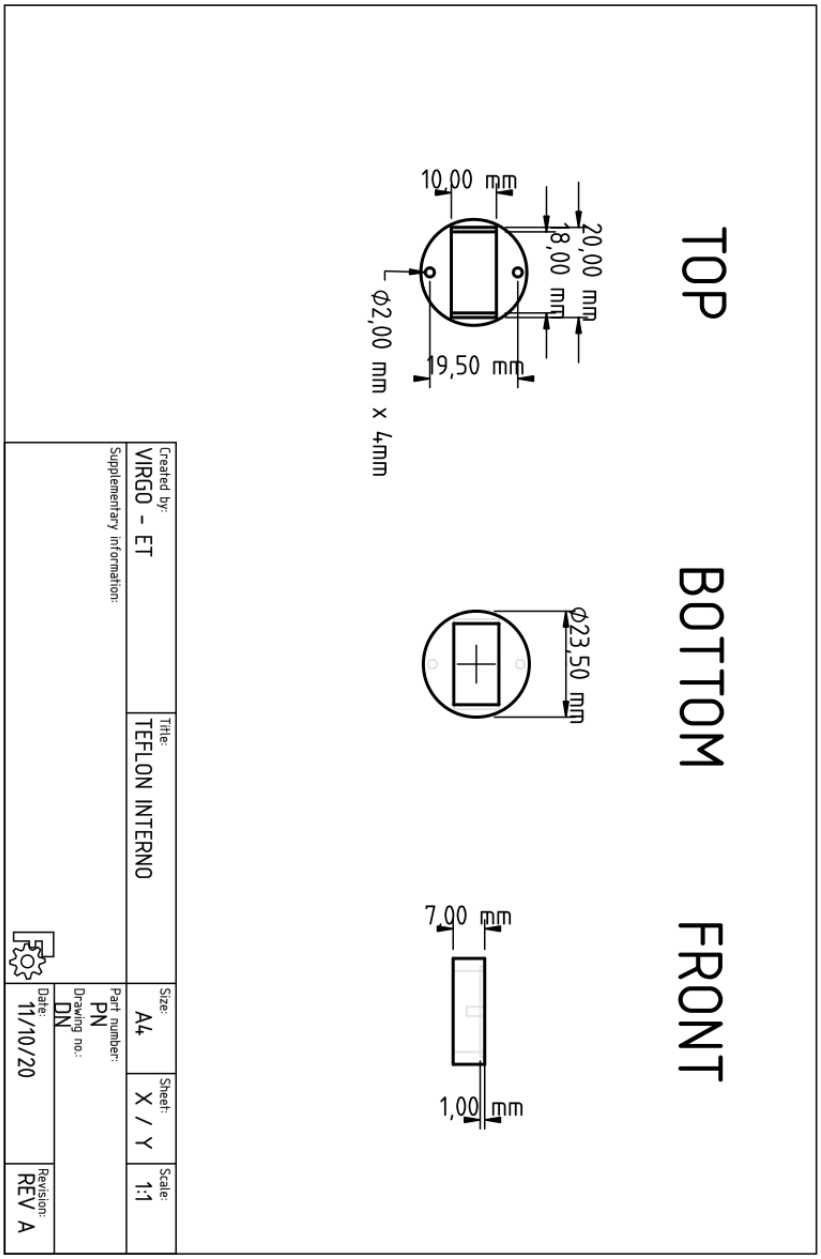

Figure A.4: Intermediate Layer - Teflon Internal Support

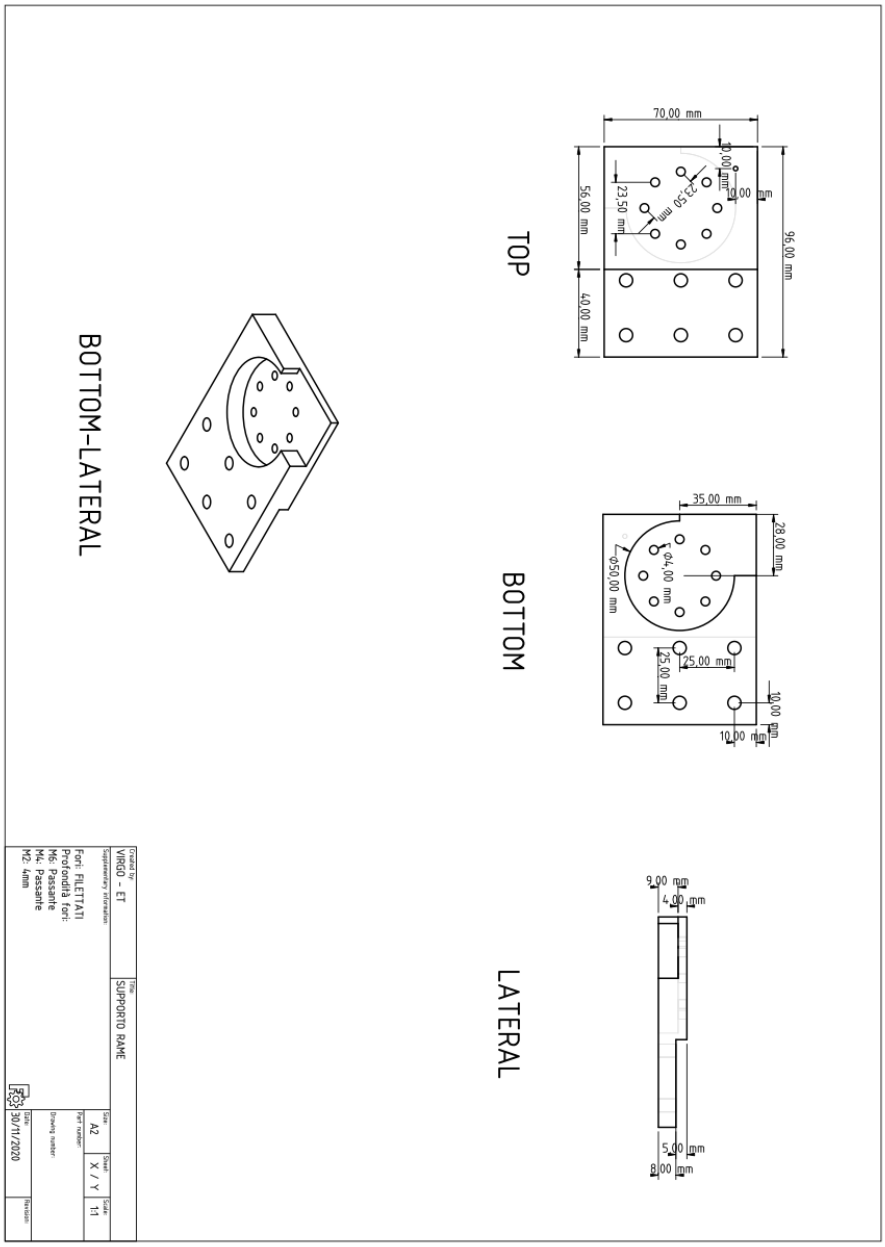

Figure A.5: Lower Layer - Copper Support

Bibliography

[1] G.F. Smoot, J.L. Cervantes-Cota, S. Galindo-Uribarri, "A Brief History of Gravitational Waves", DOI: 10.3390/universe2030022.

[2] J. Weber, "Detection and Generation of Gravitational Waves" Physical Review, 1960.

[3] J. Weber, "Observation of the Thermal Fluctuations of a Gravitational-Wave Detector", Physical Review Letters, 1966.

[4] R. L. Forward, G. E. Moss, L. R. Miller, "Photon-Noise-Limited Laser Transducer for Gravitational Antenna", Appl. Opt. 10, 2495-2498 (1971).

[5] R. Weiss, Quarterly Progress Report 1972, No 105, 54-76. Research Laboratory of Electronics, MIT, http://dspace.mit.edu/bitstream/handle/1721.1/56271/RLE_QPR_105_V.pdf?sequence=1.

[6] LIGO Collaboration, "Sensitivity of the Advanced LIGO detectors at the beginning of gravitational wave astronomy", Phys. Rev. D 93, 112004.

[7] VIRGO Scientific Collaboration, "The Advanced Virgo detector", J. Phys.: Conf. Ser. 610 012014.

[8] LIGO Scientific Collaboration, "Observation of Gravitational Waves from a Binary Black Hole Merger", DOI: 10.1103/PhysRevLett.116.061102.

[9] R. Abbot et al., "GWTC-2: Compact Binary Coalescences Observed by LIGO and Virgo During the First Half of the Third Observing Run", arXiv:2010.14527.

[10] LIGO-VIRGO Collaboration et al., "Multi-messenger Observations of a Binary Neutron Star Merger", arXiv:1710.05833.

[11] R. v. Eötvös, Mathematische und Naturwissenschaftliche Berichte aus Ungarn, 8, 65, 1890

[12] E. Di Casola, S. Liberati, S. Sonego, "Nonequivalence of equivalence principles", DOI: 10.1119/1.4895342

[13] M. Maggiore, "Gravitational Waves: Volume 1: Theory and Experiments", OUP Oxford, 2007.

[14] S. Carroll, "Spacetime and Geometry: An Introduction to General Relativity", Pearson, 2013.

[15] R.X. Adhikari, "Gravitational Radiation Detection with Laser Interferometry", DOI:10.1103/RevModPhys.86.121.

[16] https://science.gsfc.nasa.gov/663/research/index.html.

[17] https://www.lisamission.org.

[18] R.N. Manchester, "Pulsar Timing Arrays and their Applications", AIP Conference Proceedings 1357, 65 (2011).

[19] J.E. Carlstrom, A.T. Lee, "Inflation Physics from the Cosmic Microwave Background and Large Scale Structure", DOI:10.1016/j.astropartphys.2014.05.013.

[20] LIGO Scientific Collaboration, "Advanced LIGO", DOI:10.1088/0264-9381/32/7/074001.

[21] M. Punturo et al., "The third generation of gravitational wave observatories and their science reach", DOI:10.1088/0264-9381/27/8/084007.

[22] A.E. Siegman, "Lasers", University Science Books, 1986.

[23] H.B. Callen, T.A. Welton, "Irreversibility and Generalized Noise", Phys. Rev. 83, (1951).

[24] Y. Levin, "Internal thermal noise in the LIGO test masses : a direct approach", DOI:10.1103/PhysRevD.57.659.

[25] M.L. Gorodetsky, "Thermal noises and noise compensation in high-reflection multilayer coating", DOI:10.1016/j.physleta.2008.09.056.

[26] G.M. Harry et al., "Thermal noise from optical coatings in gravitational wave detectors", Appl. Opt. 45, (2006).

[27] L.D. Landau, E.M. Lifshitz, "Theory of Elasticity, third edition", Pergamon, Oxford, 1986.

[28] V.B. Braginsky, M.L. Gorodetsky, S.P. Vyatchanin, "Thermodynamical fluctuations and photothermal shot noise in gravitational wave antennae", DOI: 10.1016/S0375-9601(99)00785-9.

[29] M. Cerdonio, L. Conti, A. Heidmann, M. Pinard, "Thermoelastic effects at low temperatures and quantum limits in displacement measurements", DOI:10.1103/PhysRevD.63.082003

[30] A. Freise et al., "Triple Michelson interferometer for a third generation gravitational wave detector", Class. Quantum Grav. 26 085012, 2009.

[31] S. Hild et al., "Sensitivity studies for third-generation gravitational wave observatories", DOI:10.1088/0264-9381/28/9/094013.

[32] B.S. Sathyaprakash et al., "Scientific Objectives of Einstein Telescope", DOI: 10.1088/0264-9381/29/12/124013.

[33] B.S. Sathyaprakash et al., "Cosmology and the Early Universe", arXiv:1903.09260.

[34] R. Schnabel, N. Mavalvala, D.E. McClelland, P.K. Lam, "Quantum metrology for gravitational wave astronomy", DOI:10.1038/ncomms1122.

[35] Y. Zhao et al., "Frequency-Dependent Squeezed Vacuum Source for Broadband Quantum Noise Reduction in Advanced Gravitational-Wave Detectors", DOI: 10.1103/PhysRevLett.124.171101.

[36] L. McCuller et al., "Frequency-Dependent Squeezing for Advanced LIGO", DOI: 10.1103/PhysRevLett.124.171102.

[37] R. Abbot et al., "Tests of General Relativity with GW150914", DOI: 10.1103/PhysRevLett.116.221101.

[38] Planck Collaboration, "Planck 2018 results. VI. Cosmological parameters", DOI: 10.1051/0004-6361/201833910.

[39] E. A. Huerta and J. R. Gair, "Intermediate–mass–ratio–inspirals in the Einstein Telescope: I. Signal–to–noise ratio calculations", DOI: 10.1103/PhysRevD.83.044020.

[40] J. R. Gair, I. Mandel, M. Coleman Miller, M. Volonteri, "Exploring intermediate and massive black-hole binaries with the Einstein Telescope", DOI: 10.1007/s10714-010-1104-3.

[41] L. Baiotti, B. Giacomazzo, L. Rezzolla, "Accurate evolutions of inspiralling neutron-star binaries: prompt and delayed collapse to black hole", DOI: 10.1103/PhysRevD.78.084033.

[42] G.B. McDonalds, "A Review of Pulsar Glitch Mechanisms", Ph.D. thesis, University of Johannesburg, 2007.

[43] B.J. Owen, "Maximum elastic deformations of compact stars with exotic equations of state", DOI: 10.1103/PhysRevLett.95.211101.

[44] LIGO Scientific Collaboration, Virgo Collaboration, "GW190521: A Binary Black Hole Merger with a Total Mass of $150M_{\odot}$", DOI:10.1103/PhysRevLett.125.101102.

[45] K. Jani, D. Shoemaker, C. Cutler, "Detectability of Intermediate-Mass Black Holes in Multiband Gravitational Wave Astronomy", DOI: 10.1038/s41550-019-0932-7.

[46] Planck Collaboration, "Planck 2018 results. X. Constraints on inflation", DOI: 10.1051/0004-6361/201833887.

[47] Y. S. Touloukian, C. Y. Ho, “Thermophysical Properties of Matter; Vol.1 - Thermal Conductivity - Metallic Elements and Alloys” Plenum, 1970.

[48] Y. S. Touloukian, C. Y. Ho, “Thermophysical Properties of Matter; Vol.2 - Thermal Conductivity - Nonmetallic Solids” Plenum, 1970.

[49] T. Ruf et al., “Thermal conductivity of isotopically enriched silicon,” Solid State Communications, vol. 115 (5), 2000.

[50] S. Hild et al., "Sensitivity Studies for Third-Generation Gravitational Wave Observatories", DOI: 10.1088/0264-9381/28/9/094013

[51] J. Steinlechner et al.,"Optical Absorption Measurements on Crystalline Silicon Test Masses at 1550 nm", DOI: 10.1088/0264-9381/30/9/095007.

[52] A. Khalaidovski, J. Steinlechner, R. Schnabel, "Indication for dominating surface absorption in crystalline silicon test masses at 1550nm", DOI: 10.1088/0264-9381/30/16/165001.

[53] A.S. Bell et al., "Anomalous optical surface absorption in nominally pure silicon samples at 1550 nm", DOI: 10.1088/1361-6382/aa8aac.

[54] J. Degallaix et al., "Bulk optical absorption of high resistivity silicon at 1550 nm", DOI: 10.1364/OL.38.002047.

[55] J. Degallaix et al., "Measurement of the optical absorption of bulk silicon at cryogenic temperature and the implication for the Einstein Telescope", DOI: 10.1088/0264-9381/31/18/185010.

[56] Y. Kraftmakher, "Modulation Calorimetry - Theory and Applications", Springer-Verlag Berlin Heidelberg, 2004.

[57] K.L. Hsu, D.E. Kline, J.N. Tomlinson, "Thermal conductivity of polytetrafluoroethylene", DOI: 10.1002/app.1965.070091106.

[58] N. Pearlman, P.H. Keesom, "The Atomic Heat of Silicon below 100° K", DOI: 10.1103/PhysRev.88.398.

[59] R.J. Corruccini, J.J. Gniewek, "Specific Heats and Entalpies of Technical Solids at Low Temperatures", National Bureau of Standards Monograph 21, 1960.

[60] R. Hull, "Properties of Crystalline Silicon", INSPEC, 1999.

[61] B.J. Frey, D.B. Leviton, T.J. Madison, "Temperature-dependent refractive index of silicon and germanium", DOI:10.1117/12.672850.